Ph.D. Thesis

Investigation of electronic, optical, and magnetic properties of a quasi-one-dimensional molecular Mott insulator

（準 1 次元分子性モット絶縁体の電気，光学，磁気的性質の研究）

Muhammad Khalish NURYADIN

Department of Physics

Graduate School of Science

Tohoku University

September 2022

Investigation of electronic, optical, and magnetic properties of a quasi-one-dimensional molecular Mott insulator

（準１次元分子性モット絶縁体の電気，光学，磁気的性質の研究）

Condensed Matter Physics in Molecular Materials Group
Department of Physics, Graduate School of Science, Tohoku University
NURYADIN Muhammad Khalish

Introduction

BEDT-TTF (bis(ethylenedithio)-tetrathiafulvalene) molecule-based organic salts have been considered as one of strongly correlated electron systems which indicate Mott insulating, charge ordering, quantum spin liquid, anisotropic superconducting states and so on [1]. In most cases of the organic molecular materials, previous studies have been carried out in BEDT-TTF salts with donor and anion molecule ratio of 2:1. These salts have one hole carrier averagely in two BEDT-TTF molecules resulting in the quarter filling conduction band in principle. In contrast, a series of κ-(BEDT-TTF)$_2X$ (X = Cu[N(CN)$_2$]Y with Y = Br and Cl, Cu$_2$(CN)$_3$ etc.) has the BEDT-TTF dimer structure. Strong dimerization of BEDT-TTF molecules changes the quarter filling band structure to an effective half filling band. This effective half filling band structure is the origin of the dimer Mott insulating state with strongly correlated π-electrons.

Although active studies in the dimer-Mott organic salts, only few studies have been conducted in BEDT-TTF salts with a 1:1 ratio, which should have a genuine Mott insulating state with a half-filling band. Previous reports in 1:1 ratio of BEDT-TTF salts such as ζ-(BEDT-TTF)PF$_6$ and β-(BEDT-TTF)TaF$_6$ show that both salts are considered as a genuine Mott insulator material [2]. Recently, another 1:1 BEDT-TTF organic salt, (BEDT-TTF)Ag$_4$(CN)$_5$, has been studied as a candidate of Dirac Semimetal (DSM) with diamond lattice structure [3]. It has a Mott-insulating ground state with antiferromagnetic order at T_N = 102 K.

(BEDT-TTF)Cu[N(CN)$_2$]$_2$ is an organic salt with 1:1 ratio of donor BEDT-TTF^{+1} and anion molecules Cu[N(CN)$_2$]$_2^{-1}$. (BEDT-TTF)Cu[N(CN)$_2$]$_2$ was first reported by Wang *et. al*. [4], where the crystal has monoclinic structure and C2/c space group. Wang *et al.* concluded this compound as a semiconductor. However, (BEDT-TTF)Cu[N(CN)$_2$]$_2$ could be considered as a genuine Mott insulator from the half-filling band structure. (BEDT-TTF)Cu[N(CN)$_2$]$_2$ does not have an alternating layer structure found typically in quasi-two-dimensional (BEDT-TTF)$_2X$. Instead, this compound has three-dimensional arrangement of BEDT-TTF and anion molecules. This three-dimensional arrangement of BEDT-TTF with the shortest intramolecular distance results in a distorted diamond-like lattice structure. The band structure calculation suggested that this compound has a low dimensional system resulting in the strongest transfer integral along the *c*-axis direction, creating one dimensional zigzag BEDT-TTF chain [5]. These characteristics make this compound a promising subject for studying quasi-one-dimensional organic material with half-filled energy band.

In this study, the fundamental physical properties like as electronic, optical, and magnetic properties of (BEDT-TTF)Cu[N(CN)$_2$]$_2$ are investigated. Specially a nonmagnetic state below about 26 K was found firstly in this study [7,8], and confirmed that the state was induced by spin-singlet transition, probably considered as a spin-Peierls transition. We also study molecular disorder effect by x-ray irradiation technique.

Experiments

Single crystals of (BEDT-TTF)Cu[N(CN)$_2$]$_2$ with needle-like shape were prepared by electro-crystallization method. The longest direction of the needle shape is parallel to the *c*-axis [5]. The electronic properties were measured by dc resistivity measurements with two probes method using electrometer. The optical properties were measured by using FT-IR in far-, mid- and near-infrared regions, and a grating spectrometer in UV-Visible light region. The magnetic properties were measured by SQUID magnetometer (MPMS XL, Quantum Design) and ESR spectroscopy (JEOL JES-RE3X). The x-ray irradiation effect was examined using the same measurement setup. The x-ray irradiation was done by the tungsten tube with 40 kV and 20 mA.

Results and discussions

Fig. 1 (a) shows Arrhenius plots of the temperature dependence of the resistivities along three crystal morphology directions of *a**, *b* and *c*-axes [5]. The results show that the sample is highly insulating, and its resistivity increases with decreasing temperature. The resistivity along the *c*-axis is the most conducive in comparison to other two directions. The resistivity results show linear behavior in the Arrhenius plots well in the low temperature regions. The activation energies obtained from the Arrhenius fitting are the same value along three crystal morphology directions, indicating

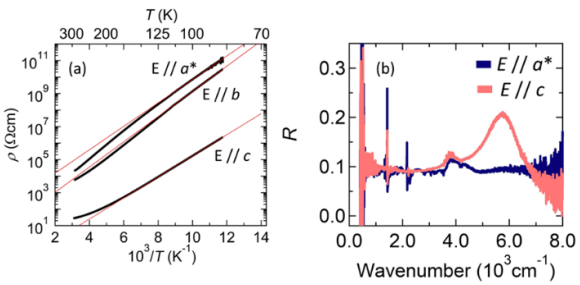

Fig. 1 (a) Arrhenius plot of the temperature-dependence of the resistivities along three crystal morphology directions *a**, *b* and *c*-axes. (b) Polarized IR reflectivity of the single crystal along the c and *a** -axes.

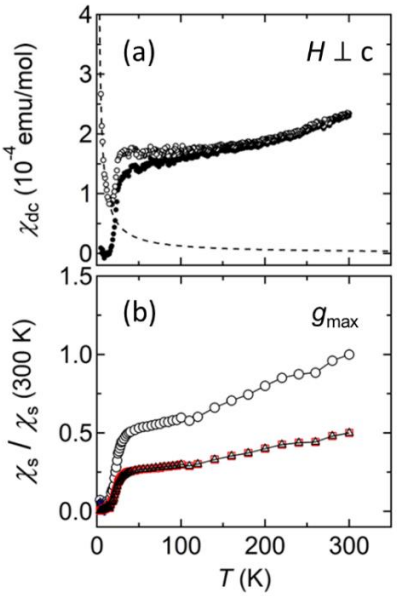

Fig. 2 (a) DC magnetic susceptibility c_{dc} at H = 1 T perpendicular to the c-axis. The dashed curve corresponds to Curie law c_C fitting to the measurement values (open circles). Filled circles correspond to the magnetic susceptibility after subtracting the Curie component c_C. (b) Total spin susceptibility χ_s from the combination of two Lorentzian component in the ESR spectrum along the principal axis of g_{max}. Square and triangle correspond to *1** and *2** of each Lorentzian component of ESR spectra, respectively.

that this compound has an isotropic energy gap of about 0.3 eV for transport properties. Fig. 1 (b) shows the polarized IR reflectivity spectra along two crystal axes. The reflectivity spectra consist of several sharp molecular vibration modes and two broad bands representing charge excitation. The larger charge excitation peak comes from the Hubbard band transition with onsite coulomb energy of about 0.7 eV. This energy is in a good agreement with the theoretical value. The result also suggests that charge excitation from the Hubbard band has anisotropic behavior. On the other hand, lower charge excitation peak has almost isotropic behavior located around 4000 cm^{-1}. This isotropic charge excitation, with the value of 0.4 eV, might relate to the isotropic energy gap found in the transport measurements.

Fig. 2 (a) shows the static susceptibility χ_{dc} measured by the SQUID magnetometer. The results indicate a spin-singlet like transition at $T_{sp} \approx 26$ K. The Curie contribution is subtracted in consideration of 1.1 % of $S = 1/2$ impurity spins. To confirm spin-singlet like transition in this compound, ESR spectroscopy measurements have been conducted [6]. The ESR signals from π-electrons on BEDT-TTF molecules are observed and the g-value along principal axes are determined. Fig. 2 (b) shows spin susceptibility χ_S along the g_{max} direction. At the same temperature of T_{SP}, χ_S decreases as following the temperature dependence of $\chi \propto A\,exp(-\Delta/T)$ with a spin gap $\Delta \sim 90$ K. Below about 75 K, the ESR spectrum becomes asymmetric because two Lorentzian components *1** and *2** having different parameters, line width and peak amplitude, appear to consist of the asymmetric shape of the spectrum. These two components might come from

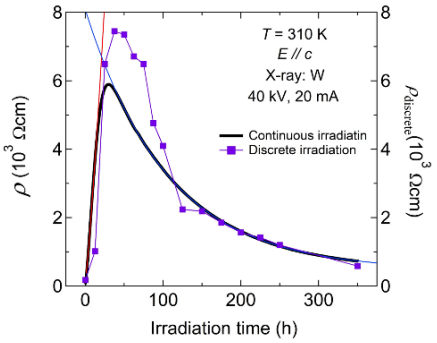

Fig. 3 x-ray irradiation time-dependence of the resistivity at 310 K. Solid thick curve corresponds to the resistivity change with continuous x-ray irradiation. Square corresponds to the resistivity after each step of the x-ray irradiation time.

two independent BEDT-TTF molecules because their g-values are almost close to each other. These observations indicate that two Lorentzian components of the ESR spectrum are important to form a spin-singlet state in a likely pair of BEDT-TTF molecules in this compound. Therefore, these ESR results may indicate a spin-Peierls transition in the zigzag BEDT-TTF chain structure of this compound.

X-ray irradiation effect on the resistivity at 310 K is shown in Fig 3. The results show a nonmonotonic change in the resistivity with the x-ray irradiation time. The resistivity increases until critical time of 30 hours and decreases with increasing irradiation time. The results suggest that there are two contributions for the transport properties affected by x-ray irradiation. This behavior is different from the other organic dimer Mott insulators [7].

Summary

In this study, a genuine Mott insulating state expected in (BEDT-TTF)Cu[N(CN)$_2$]$_2$ has been investigated in a comprehensive manner. The anisotropic behaviors observed in the transport and optical measurements indicate that this compound is a quasi-one-dimensional system. The magnetic property measurements show that the system has a spin-singlet state below about 26 K, which is confirmed by the ESR spectroscopy. The spin-singlet might be formed at a pair of BEDT-TTF molecules in the zigzag one-dimensional chain, indicating a spin Peierls transition.

References

[1] K. Kanoda and R. Kato, Annu. Rev. Condens. Matter Phys. **2**, 167 (2011).
[2] T. Kawamoto *et.al*, J. Phys. Soc. Jpn. **90**, 103703 (2021).
[3] Y. Shimizu Phys. Rev. B **99**, 174417 (2019).
[4] H. H. Wang *et.al.*, Chemistry of materials **2**, 247 (1992).
[5] N. Yoneyama, M. K. Nuryadin, *et.al.*, to be submitted.
[6] M. K. Nuryadin, *et.al.*, in preparation
[7] T. Sasaki, Crystals **2**, 374 (2012).

Acknowledgments

I acknowledge Prof. N. Yoneyama for providing crystals and Prof. T. Tsumuraya for DFT band structure calculation. A part of mid-IR measurement was performed at BL43IR in SPring-8. ESR spectroscopy measurements were performed in RIKEN with helping by Dr. Y. Oshima

Acknowledgments

First and foremost, I would like to express my deepest appreciation to Prof. Takahiko Sasaki for all his guidance and support. He always helps me, not only to understand better of my research but also giving advice and support for my academic and non-academic process throughout my entire graduate studies. I also would like to thank Dr. Satoshi Iguchi who always taught and helped me, mentoring me during my research process, experiment, instrument maintenance, in addition to being my discussion counterpart. Also, I would like to thank those who helped my graduate work: Prof. Naoki Yoneyama for providing sample, tight-binding approximation results, and insights; Prof. Takao Tsumuraya for DFT band structure calculation; and especially Dr. Yugo Oshima for his irreplaceable support as a mentor during the entire process of ESR spectroscopy measurements in RIKEN facility, which the results became the main part of my doctoral dissertation defense. I greatly appreciate having the experience to do experiments of mid-IR measurement at BL43IR in SPring-8. To all member Sasaki Lab, especially Dr. Tetsuya Furukawa and Dr. Shiori Sugiura for their input during group meetings. To student members for their kindness and to all junior members who gave me wonderful time in the Lab and lovely memories of living in Japan. Special thanks to my partner Elza Firdiani Sofia for important late-night discussions, writing process, and major proofreading, and to my friend Alwan Abdillah Darussalam for helping me sorting my thinking process and creative insights when I got stuck in my research process. There were so many people that I could not mention that all friends, people who helped me, people who helped giving happiness during my stay in Sendai. I want to thank you from the bottom of my heart because without them; I would not be able to be what I am today. Finally, I would like to thank my parents, brother, and sisters, who always being supportive and motivated me, accompanying me all night long so I could finish my thesis on time.

This research would not be possible without the generous support of Japan ministry of science (MEXT) scholarship and IGPAS Program of Tohoku University.

Table of Contents

List of Figures

This thesis is dedicated to the late memories of my father
Dr. Suwirman Nuryadin (1952-2019) and my brother Afiq Amhar Nuryadin (1998-2021).

Chapter 1 Introduction

In the early study, the independent electron model is a simple approximation to determine electronic properties in the material. This approximation can distinguish the metallic or insulating behavior in material by the filling of electronic band and the energy gap between occupied-unoccupied level. This approximation treats the electrons as non-interacting particle from which the energy bands can be derived. When electron interaction becomes dominant in material, the independent electron model fails to explain phenomena that come from this material. In this situation, when strong electron interaction is dominant in material, it is called as strongly correlated electron system. In the study of the strongly correlated electrons system, Mott insulating state is one of the attractive phenomena for studying Metal-Insulator (MI) transition. Organic conductors become a promising class for studying strongly correlated system material due to their interesting physical phenomena such as high temperature superconductor and MI transition. This chapter will briefly introduce about MI transition by Hubbard model, spin Peierls transition, organic conductor material, and last section is motivation of this study.

1.1 Metal Insulator (MI) transition in strongly correlated system

An MI transition can occur in a half-filling band system where one charge exists per site. It starts when the electron hops to another occupied site and generating on-site Coulomb repulsion *U*. The on-site Coulomb repulsion *U* appears as an effect that prohibits double occupancy of the site. When electron-electron interactions become dominant owing to the relatively large on-site Coulomb energy *U* with respect to bandwidth *W*. The localization to individual sites of these electrons will minimize mutual repulsion which makes an opening charge gap at Fermi level [1]. Fig. 1.1 shows the opening charge gap from the original half-filling band into full band. The magnitude of this phenomena can be defined using one-band Hubbard Hamiltonian with relation,

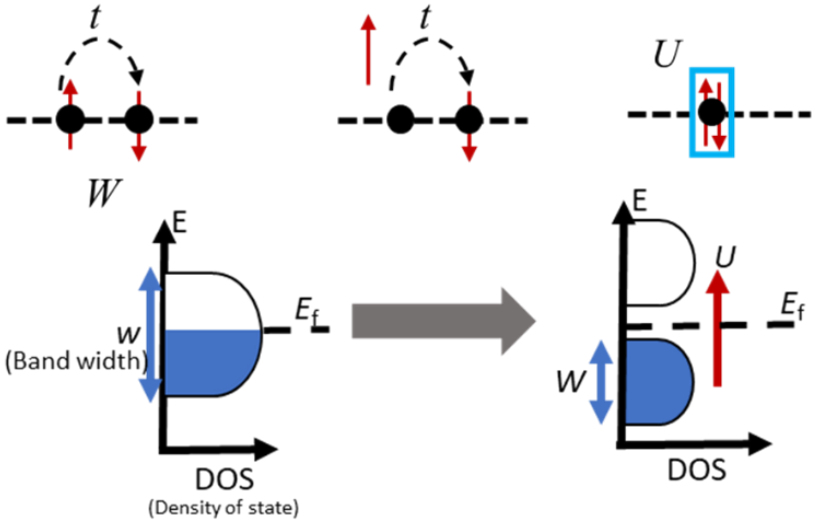

Fig. 1. 1 MI transition Mott insulator in hall-filling Hubbard model

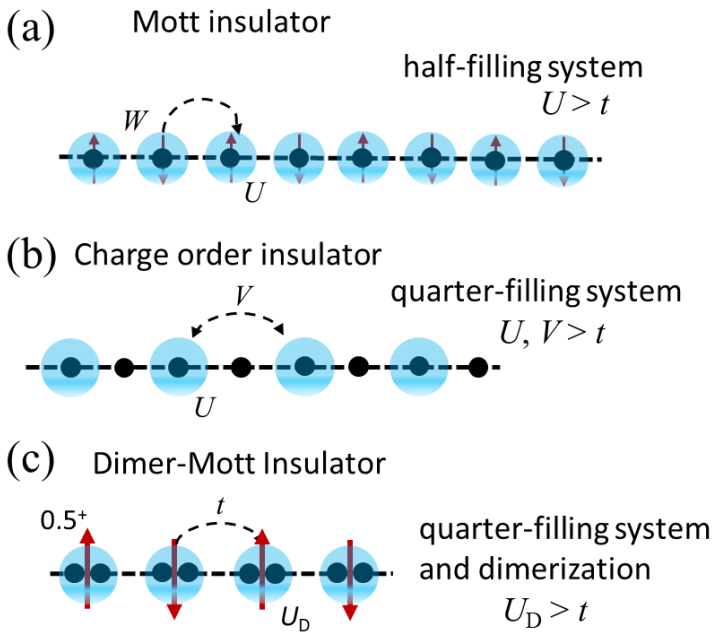

Fig. 1. 2 Mott insulator, charge order insulator and Dimer-Mott insulating state based on the magnitude relationship between the transfer integral t, the on-site Coulomb repulsion U, and the inter-site Coulomb repulsion V in strongly correlated electron systems (a) Mott insulator when U > t, (b) charge order insulator when U, V > t and (c) Dimer-Mott insulator when $U_D > t_D$.

from hopping action electron and the on-site Coulomb repulsion *U* [3],

$$H = -t \sum_{\langle i,j\rangle\sigma} \left(c_{i\sigma}^{\dagger} c_{j\sigma} + \text{h.c.}\right) + U \sum_{i} n_{i\uparrow} n_{i\downarrow} \tag{1.1}$$

where $c_{i\sigma}^{\dagger}$ and $c_{j\sigma}$ are the operators for creation and annihilation single electron on site *j* with spin polarization σ, $n_{j\sigma} = c_{i\sigma}^{\dagger} c_{j\sigma}$ is the occupation number operator, the transfer integral *t* or electron kinetic energy, and *U* is the on-site repulsion. When half-filling band split into upper Hubbard band and lower Hubbard band, total density of state for each band is *N* atoms where *N* are double-occupied upper Hubbard and single-occupied for lower Hubbard band. When on-site Coulomb *U* is larger than transfer integral *t*, the Hubbard model solution become insulating phase and is called Mott insulator [37]. The MI transition depends on competition between carrier localization and the delocalization. To control MI transition, it can be done by controlling bandwidth *W* because the bandwidth *W* came from delocalization energy *t*. To control bandwidth itself, it can be done by giving external force to lattice and this method is called as bandwidth-controlled MI transition. The other method to control MI is by giving electron or holes which affect Coulomb repulsion *U*, and this is called as carrier-induced MI transition.

MI transition can also occur in the quarter-filling band system. The electronic state of this system can be well explained by the extended Hubbard model [2],

$$H = -t \sum_{\langle i,j\rangle\sigma} \left(c_{i\sigma}^{\dagger} c_{j\sigma} + \text{h.c.}\right) + U \sum_{i} n_{i\uparrow} n_{i\downarrow} + \sum_{\langle i,j\rangle} V_{ij} n_i n_j \tag{1.2}$$

Fig. 1.2 show relation between *U*, *V* and *t* in a strongly correlated system. In the quarter-filling system, there are two types of strongly correlated system, charge-ordered and Dimer-Mott insulator. In charge-

ordered system, one charge exists at two sites. The on-site Coulomb repulsion in this system is not only from U but also came from inset Coulomb repulsion V between two sites. In this situation, the transfer integral t and the in-site of Coulomb repulsion V now has relation between each other. When on-site Coulomb U and in-site Coulomb V are larger than transfer integral t, charge order insulator can be realized. For Dimer-Mott insulator, usually occurs in organic conductor. For instances, BEDT-TTF (bis(ethylenedithio)-tetrathiafulvalene) molecule based organic conductors have a highly strong correlated electronic state. In $(BEDT\text{-}TTF)_2X$ where X is monovalent, BEDT-TTF donor molecule has +1/2 hole charge which corresponds to quarter-filling band structure, that is, three-quarters energy band occupied by electrons. The dimerization between two molecules plays an important role to change the three-quarters energy band to split into bonding and antibonding bands, resulting in effective half-filling band. After the effective half-filling has been acquired, each dimer is regarded as one unit and charge degrees of freedom inside of dimers are disregarded. In this model, now the parameters of extended Hubbard model are the on-dimer Coulomb interaction U_D, Intradimer Coulomb V_0 and intradimer transfer integral t_d, which depend on the local geometry of dimer [3].

1.2 Low dimensional system: Spin-Peierls transition

One-dimensional (1-D) system can be described by simple tight-binding binding approximation as equation $\varepsilon_k = -2tcos(ka)$, where t is electron-electron hopping between neighboring sites and a is lattice period [85], which the energy band can be described as Fig. 1.3 (a) as a cosine band. Assuming this 1D system is come from 1D linear chain, the Hamiltonian of nearest-neighbor exchange coupling J of antiferromagnet Heisenberg S = 1/2 describe as [86],

$$H = J\sum S_i \cdot S_{i+1} \tag{1.3}$$

where S_i is spin operator at the site i. Each site has one electron resulting in energy band will be exactly half-filled. Peierls in 1955, showed that a 1-D metallic lattice with uniformly spaced site and half-filled band is not stable at low temperatures [87]. The unstable state can be in the form of elastic distortion of

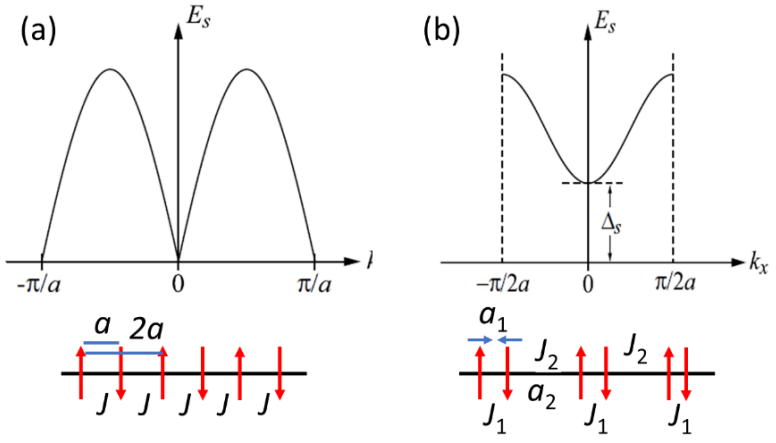

Fig. 1. 3 Schematic illustration of dispersion magnetic excitation S = 1/2. (a) Uniform 1D linear chain with $\gamma_{ex} = 1$. (b) Alternating 1D linear chain with $\gamma_{ex} < 1$. The singlet ground state is separated by an energy gap Δ_s [86]

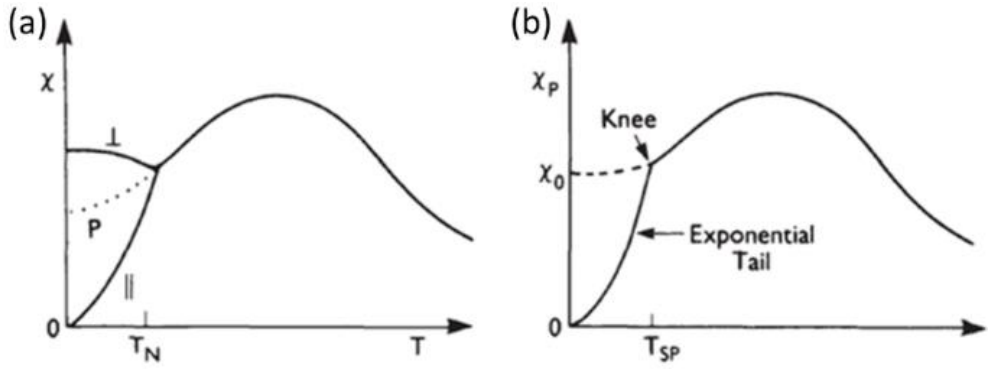

Fig. 1. 4 (a) Magnetic susceptibility of a quasi-one-dimensional Heisenberg-like antiferromagnetic with temperature long-range order is T_N (Néel point). (b) Magnetic susceptibility of a quasi-one-dimensional spin-Peierls antiferromagnetic system with temperature T_{SP} [88].

the lattice namely, magnetoelastic at low temperature regions. When the uniform 1D linear chain experiencing magnetoelastic at critical temperature T_{SP}, this phenomenon called as spin-Peierls transition [88]. An elastic distortion in the lattice will influence the exchange energy of the spin chains in the function of separation between adjacent lattice sites. The Hamiltonian of change of exchange energy due to alternation lattice become

$$H = \sum_{i=0}^{N/2} (J_1 S_{2i} \cdot S_{2i-1} + J_2 S_{2i} \cdot S_{2i+1}) \tag{1.4}$$

where change of exchange coupling from J to J_1 and J_2 with alternation parameter $\gamma_{ex} = J_2/J_1$, and there is different lattice period a as shown in Fig. 1.3 (b) [86]. The antiferromagnet order in ideal 1D magnetic model with short-range interactions can occur only at T = 0 K. However, most of the spin-Peierls transitions occur at non-zero temperature T_{SP}. This means weak interchain interactions are necessary [88]. Weak interchain interactions can occur in quasi-one-dimensional system where the material has three-dimensional structure with weak inter-stack couplings and non-rigid structure [89].

For alternating chain with $\gamma_{ex} < 1$, energy gap Δ_s will open in the spin excitation spectrum, and the ground state becomes nonmagnetic as shown in Fig. 1.3 (b) [86]. On contrary, in the Hubbard model with limit of large U/t, uniform $J = 2t^2/U$ and the excitation spectrum gives a non-zero susceptibility at T = 0 K. The energy gap Δ is between the singlet ground state and the triplet excited states at temperature T_{SP}. When T_{SP} smaller than Δ, zero magnetic susceptibility χ can be observed as a sharp decrease in χ as shown in Fig. 1.4. The energy gap Δ of temperature dependence of magnetic susceptibility χ can be calculated by Bulaevskii model that obtained by using Hartree-Fock approximation,

$$\chi = \frac{N g^2 \mu_B^2 \alpha}{k_B T} \, exp\left(-\frac{\beta J_1}{T}\right) \tag{1.5}$$

where the value of α and β are parameters tabulated in the reported paper that depend on alternating parameter γ [78].

1.3 Molecular organic conductors

Organic conductor is realized when charge transfer occurs between donor and anion molecules and conduction carriers (typically hole) are induced on donor molecules. The charge-transfer salt reaction can be written as $[D_{\mathrm{m}}] + [X_n] \rightarrow [D_m]^{+\delta} + [X_n]^{-\delta}$, where D is donor molecule, X is anion molecule, and δ is charge transfer ratio which can calculate from chemical composition in organic conductor type [86]. There are three organic conductor type such as $(TMTTF)_2X$, $(BEDT\text{-}TTF)_2X$, and $(BEDT\text{-}TTF)X$.

1.3.1 $(TMTTF)_2X$

Since the discovery of the first organic superconductor in 1980, $(TMTF)_2PF_6$, there have been many studies of molecular organic conductors [4]. This material can reach superconductivity at 0.9 K with 12 kbar. This material is part of charger-transfer salts (CT's) class, a compound consists of two molecules where one molecule act as a donor and the other one act as an acceptor. When one of them is partially charged, conductivity is induced [5]. This can be explained by making the difference between the highest occupied molecular orbital (HOMO) and the lowest unoccupied orbital (LUMO) of the organic molecule to be small and causing overlap between them to form partially filled bands. Most organic conductor has 2:1 ratio where the donor molecule has +1/2 charge. HOMO can contain up electron (or holes). Therefore, band filling in organic conductor 2:1 ratio is 3/4-occupied, and the remaining is empty [6].

There are also other band fillings in organic material as shown in Fig. 1.5. $(TTM\text{-}TTP)I_3$ is 1:1 ratio organic material with highly one-dimensional half-filling band in their system. Because of half-filling in this material, MI transition can be acquired. T. Mori *et. al*., has reported that there was a sudden jump in resistivity measurement and this feature is attributed to MI transition [7]. The NMR result

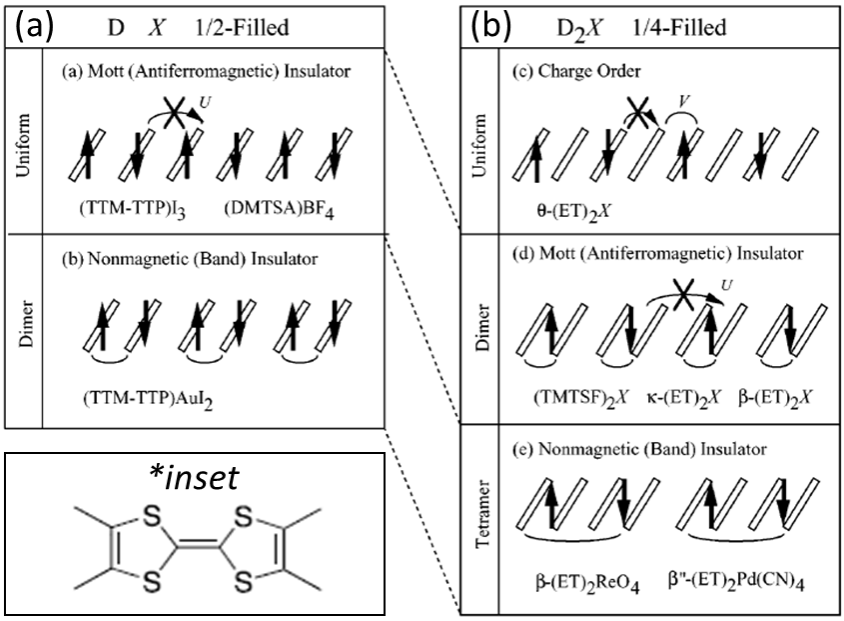

Fig. 1. 5 Relation between band filling and lattice periodicity in TMTTF-based organic conductor (a) half-filling band and (b) quarter-filling band. [6]. Inset figure is TMTTF molecule.

suggested the MI transition of this material is charge-ordering with temperature transition 120 K [8]. Later, the Raman spectroscopy result did not find any phase transition, but there is an intramolecular deformation at below 160 K which was thought to be the cause of the MI transition. According to T. Mori, breaking symmetry in molecule TTM-TTP created an energy gap in metal-like phase. The instability of TTM-TTP against asymmetric deformation can be an inherent property of a long molecule or it can be a consequence of intramolecular Coulomb repulsion [9].

1.3.2 (BEDT-TTF)$_2X$

BEDT-TTF (bis (ethylendithio) tetrathiafulvalene) molecule is a typical donor molecule of a molecular organic conductor with pseudo-two-dimensional conductivity. The molecule pentagonal bonding ring and hexagonal bonding ring of combination Sulfur and Carbon as shown in Fig. 1.6. The overlapping of π orbital between two sulfur atoms from two different molecules is an important parameter which will determine the electronic properties of BEDT-TTF-based organic conductor. In the organic conductor with charge transfer, salt of (BEDT-TTF)$_2X$ (composition ratio 2:1) with two BEDT-TTF$^{+0.5}$ as donor molecule will correspond to quarter filling band structure and monovalent anion X. Most of (BEDT-TTF)$_2X$ has a pseudo-two-dimensional structure in which conductive BEDT-TTF molecular layer and insulating anion layer are alternately laminated. There are some organic conductors that exhibit superconducting with transition temperatures above 10 K [10-12].

In the report from C. Hotta, Fig. 1.6 shows diagram relation between position of packing molecules of BEDT-TTF in the crystal structure with band structure in the (BEDT-TTF)$_2X$ organic conductor [13]. The shaded area in the diagram of organic conductor type represents a unit cell. Molecular organic conductors show various molecular arrangements such as β-type, θ-type, κ-type and λ-type. In comparison of band structures, the upper two bands of κ-type and λ-type look similar with β-type and θ-type, respectively, because their lattice structures are identical with each other. The only

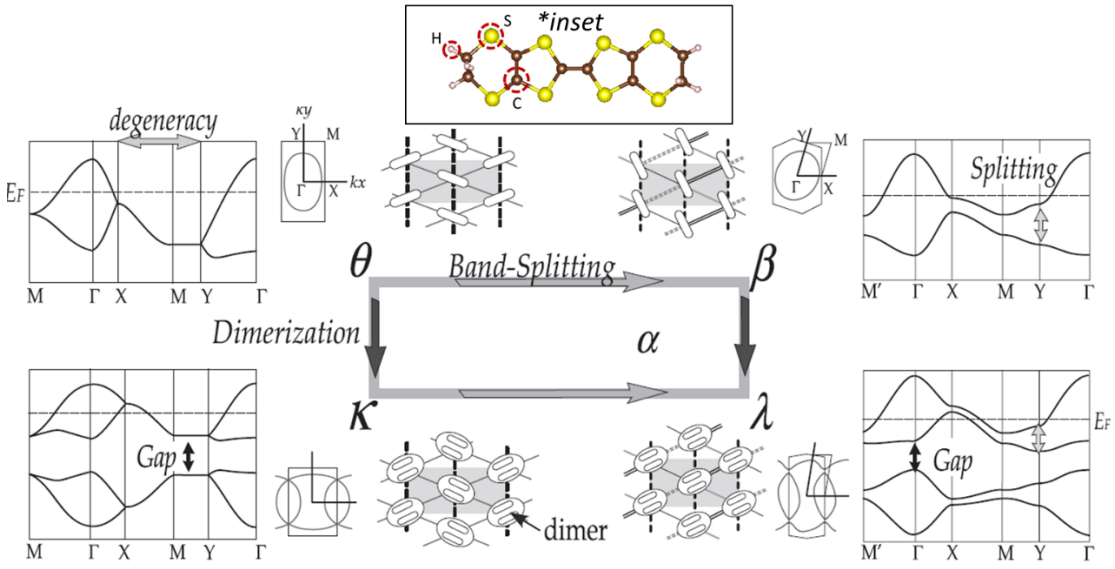

Fig. 1. 6 Molecular arrangement, band structure, schematic diagram of Fermi surface of BEDT-TTF salt [13]. Inset figure is BEDT-TTF molecule

different is that κ-type and λ-type have dimerization parameter between two molecules, and thus each dimer become a unit. In addition, the upper two bands of κ-type and λ-type, the so-called antibonding orbital, create gaps towards the lower bands. The band structure of κ-type has a large band gap because this type has strong dimerization and the transfer integral between dimer pairs can form anisotropic triangular lattice which has different two different values of transfer integrals. In the case of λ-type, it has strong dimerization but less symmetric anisotropic triangular lattice [52]. Therefore, κ-type and λ-type are classified as Dimerization in the Fig. 1.6. The other classification is band splitting which depends on the degeneracy along Brillouin zone boundary at (*X*-*M*-*Y*) of band structures. In the diagram, θ-type and κ-type have degeneracy, and in the β-type and λ-type degeneracy is vanished.

(BEDT-TTF)$_2$*X* organic salt has attracted many studies from metal-insulator (MI) transition to quantum spin liquid (QSL) [53, 52]. Among them, κ-(BEDT-TTF)$_2$*X* is known as a typical bandwidth-controlled Mott transition system where the ratio of donor molecule BEDT-TTF$^{+0.5}$ and monovalent anion *X* is 2:1. The κ-(BEDT-TTF)$_2$*X* has averagely +1/2-hole charge at a donor molecule which corresponds to quarter filling band structure, that is, three-quarters energy band occupied by electrons. When BEDT-TTF molecules have strong dimerization in a κ-(BEDT-TTF)$_2$*X* crystal, the three-quarters-filled energy band turns to an effective half-filling dimer band. κ-(BEDT-TTF)$_2$Cu[N(CN)$_2$]Cl is well known as an antiferromagnetic dimer-Mott insulator where in the temperature dependence of resistivity has sudden jump below 50 K as Mott insulating transition. This sudden increase on resistivity because opening gap of effective half-filling band filling, causes by strong dimerization from two BEDT-TTF molecules turn quarter-filling band to effective half-filling band, generates the effective Coulomb energy U_D on the dimer [26-28]. Furthermore, κ-(BEDT-TTF)$_2$*X* material has a softness in the lattice which enables to tune the bandwidth by giving pressure but keeping band-filling [29-31]. This dimer Mott insulator can be turn into a superconductor with T_c = 12.8 K by applying pressure of 30 MPa [55]. In a recent study of electron spin resonance (ESR), κ-(BEDT-TTF)$_2$Cu$_2$(CN)$_3$ is considered as a candidate for QSL with a gapped magnetic ground state at the temperature $T^* \approx 6$ K [56]. This non-magnetic ground state of spin-singlet is formed on the S = 1/2 triangular lattice, the so-called valence bond solid (VBS). This scenario is also discussed in Kagome lattice and higher-dimensional QSL candidates. Ground state with spin gap below T^* of spin susceptibility implies that this organic salt has a similar transition phase with spin-Peierls transition in the organic linear chain. The triangular lattice is distorted due to the T^* transition, followed by shrinkage of the *c* axis accompanied by lattice softening [56]. There is also an important role of defects to the VBS magnetic ground that create vacancy affecting nearby spin-singlet to become localized unpaired spins [4]. The other study of molecular disorder, x-ray irradiation effect direct to κ-(BEDT-TTF)$_2$Cu[N(CN)$_2$]Cl, introduced CN-bond defects to the anion layer that suppressed magnetic order similar to the QSL state [57].

1.3.3 (BEDT-TTF)*X*

Many studies have been carried out on BEDT-TTF organic salts with a 2:1 ratio, but only few have been conducted on BEDT-TTF organic salts with a 1:1 ratio. There are two studies that have been conducted on 1:1 BEDT-TTF organic salts such as ζ-(BEDT-TTF)PF_6 and β-(BEDT-TTF)TaF_6 with in-depth fundamental properties studies [58, 59]. Both organic salts are considered as genuine Mott insulator materials. The ζ-(BEDT-TTF)PF_6 shows Mott-Hubbard insulating type as provided by the transport and optical measurement results. The ζ-(BEDT-TTF)PF_6 has two-dimensional sheets of BEDT-TTF separated by sheets of anion that are parallel to each other in the *ab* plane. The magnetic susceptibility of this organic salt has a sudden drop at the transition temperature T_{sp} around 40 K, which suggests the spin-Peierls transition. The new inter-molecular vibration modes are found above temperature T_{sp} which is suggested as three-dimensional softening of lattice mode compatible with spin-Peierls dimerization [58]. However, there is no structural analysis below 40 K for ζ-(BEDT-TTF)PF_6 organic salt reported so far. The β-(BEDT-TTF)TaF_6 is considered as quasi-two-dimensional square lattice with half-filled band [59]. The transport and magnetic properties results suggest that β-(BEDT-TTF)TaF_6 is a Mott insulator material with antiferromagnetic ordered state at Néel temperature T_N = 10 K.

The other 1:1 BEDT-TTF organic salt, (BEDT-TTF)$Ag_4(CN)_5$, has intensively been studied as a candidate of Dirac Semimetal (DSM) organic salts with diamond lattice structure [60-62]. DSM state is a linearly crossing band dispersion near Fermi level that can be found in diamond lattice, and when the presence of spin-orbit coupling is strong, topological insulator will emerge in the diamond lattice [63,54]. Moreover, diamond lattice structure is a good system to study strong spin frustration as a condition for QSL [63]. (BEDT-TTF)$Ag_4(CN)_5$ has an orthorhombic crystal structure with space group *Fddd*. Also, (BEDT-TTF)$Ag_4(CN)_5$ has three-dimensional (3D) BEDT-TTF arrangement that interacts via sulfur-to-sulfur atoms or S-S contact with equal distance to the nearest neighbors around 3.91 Å. The geometry character of this arrangement resembles 3D diamond lattice which is supported by equal transfer integral t = -68.442 meV, calculated by a tight-binding model fitted to the HOMO band [60]. Compared to the previous 1:1 ratio, the $Ag_4(CN)_5^-$ anion molecule has infinite chain with honeycomb shape surrounded BEDT-TTF molecule in the *bc* plane. (BEDT-TTF)$Ag_4(CN)_5$ has been reported to have a Mott-insulating ground state by resistivity measurement. In the magnetic susceptibility, (BEDT-TTF)$Ag_4(CN)_5$ shows antiferromagnetic ordering at temperature T_N = 102 K. However, a weak ferromagnetic have been observed as non-zero magnetic moment in the magnetic susceptibility near the lowest temperature caused by a spin canting with angle 0.012° [60]. Although (BEDT-TTF)$Ag_4(CN)_5$ has strong spin frustration, antiferromagnetic ordering is preventing QSL state because annihilation of inversion symmetry, and ratio of exchange coupling J and next-nearest-neighbor J' is $J'/J = 0.004$, which is less than requirement for QSL state ($J'/J = 1/8$) [61].

1.4 X-ray irradiation effect in organic conductors

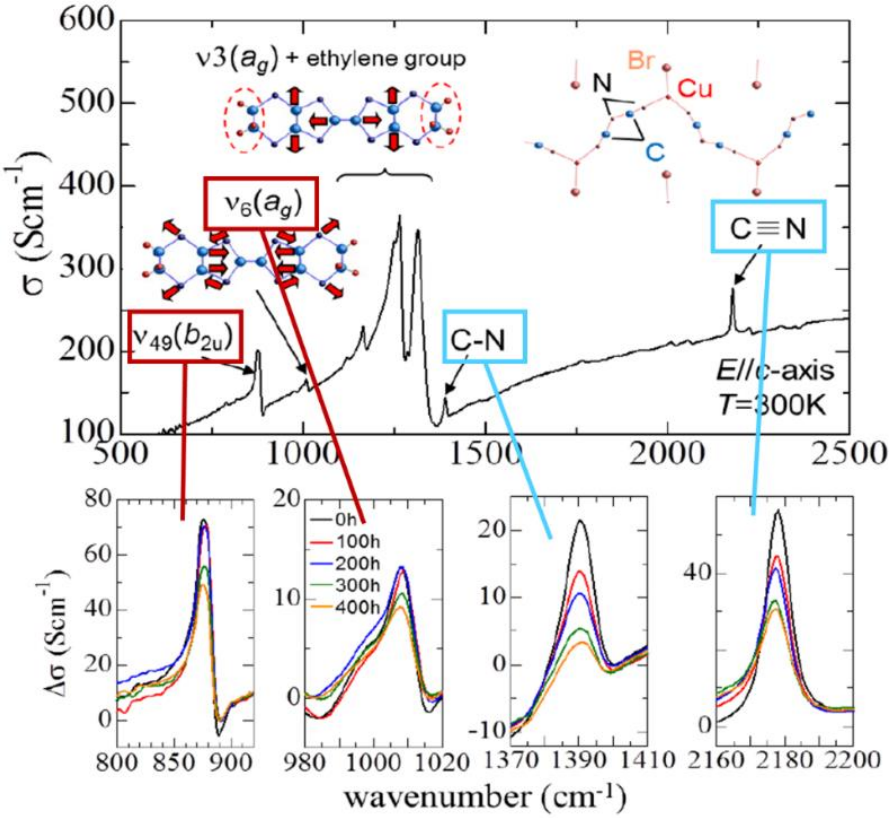

Fig. 1. 7 Changes in molecular vibrational intensity of κ-(BEDT-TTF)$_2$Cu [N(CN)$_2$]Br by X-ray irradiation [1]. The peaks of the *v*49 and *v*6 vibration modes of BEDT-TTF molecule observed at 880 cm -1 and 1010 cm -1 respectively, and for anion part vibration modes are 1390 cm-1 and 2180 cm-1, the peaks of the C-N and C≡N.

The X-ray irradiation effects on molecular organic conductors have been studied for a long time. By irradiating X-ray to molecular organic, it will introduce impurities and defects into sample which cause scattering carriers in electric conduction and breaking up the paths of electric conduction in low-dimensional substances. This results in a lowering transition temperature of the superconducting state [15]. However, it has not been elucidated yet how defects are generated by irradiation. In the case of inorganic material, irradiation effect will be shifted atom position in that material, then turn into amorphous structure and it can be repair by heat treatment. While in the case organic material, it is considered that the defects generated in the organic material by irradiation are irreversible because the defect comes from the bonds that break, gasified, or lost. In addition, the number of defects introduced into organic matter is known to be proportional to the total energy absorbed by the organic matter [16].

The studies about X-ray irradiation effect into organic material have done in experiment and simulation on the BEDT-TTF system [17-23]. In the reported experiment, X-ray irradiation was performed with white X-ray (non-filtered, 40 kV, 20 mA, 0.5 MGy / h) of a tungsten tube. Fig. 1.7 shows the change of intensity in the optical conductivity of molecular vibration mode in κ-(BEDT-TTF)$_2$Cu[N(CN)$_2$]Br due to X-ray irradiation measured by MID-IR measurement. In this report, there are four vibration mode from (BEDT-TTF)$_2$Cu[N(CN)$_2$]Br structure such as two vibration mode *v*49 and *v*6 from BEDT-TTF molecule, and two vibration more from anion part C-N and C≡N. The X-ray

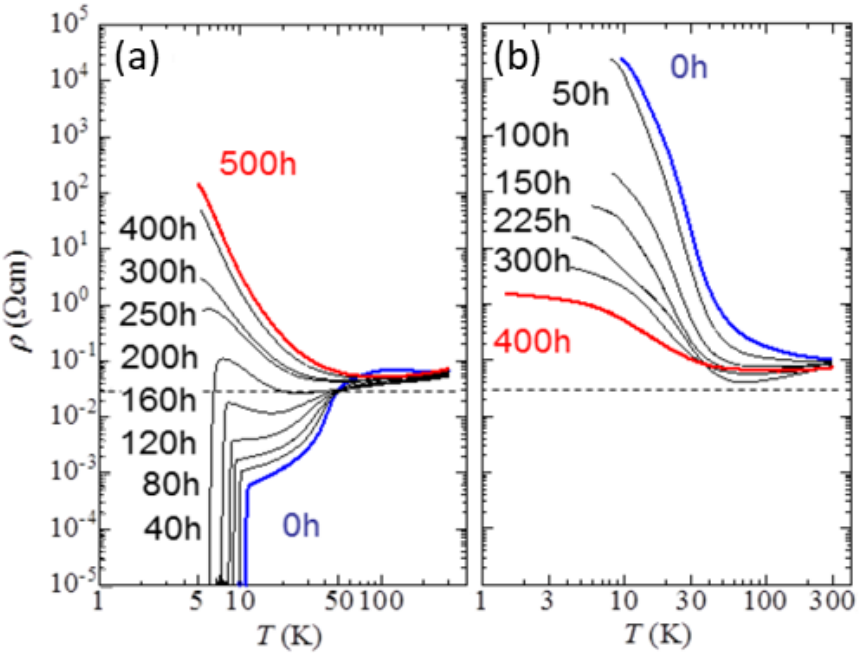

Fig. 1. 8 X-ray irradiation effect on resistivity of κ-(BEDT-TTF)$_2$X; (a) κ-(BEDT-TTF)$_2$Cu[N(CN)$_2$]Br and (b) κ-(BEDT-TTF)$_2$Cu[N(CN)$_2$]Cl [1].

irradiation effect on intensity of vibration of BEDT-TTF molecule is hardly changed, while in C-N and C≡N vibration mode is decreasing with increasing irradiation time. This means X-ray irradiation causing defect on anion part of (BEDT-TTF)$_2$Cu[N(CN)$_2$]Br. Similar behavior also can be seen in the X-ray irradiation on *κ*-(BEDT-TTF)$_2$Cu[N(CN)$_2$]Cl [19].

The X-ray irradiation effect on resistivity were performed on two different organic conductor κ-(BEDT-TTF)$_2$Cu[N(CN)$_2$]*X'* (*X'* = Br or Cl) as shown in Fig. 1.8. The CN-bond defects that occur in the anion layer work as a random potential to the conduction electrons in BEDT-TTF molecule layer, which will affect electronic properties in organic conductor. κ-(BEDT-TTF)$_2$Cu[N(CN)$_2$]Br is originated as superconductor material with transitions T_c at 11 K as sudden drop at resistivity value. Fig. 1.8 (a) shows x-ray irradiation effect temperature dependence of resistivity on κ-(BEDT-TTF)$_2$Cu[N(CN)$_2$]Br. The resistivity change into insulating-like characteristic by increasing irradiation time. The random potential, also known as the randomness effect, creates Anderson-type electron localization in the superconductor material. Therefore, superconductor state in the κ-(BEDT-TTF)$_2$Cu[N(CN)$_2$]Br change to Anderson insulator state. On the other hand, Fig. 1.8 (b) x-ray irradiation effect on dimer mott insulator in κ-(BEDT-TTF)$_2$Cu[N(CN)$_2$]Cl, which the resistivity on this organic conductor decreased as increasing irradiation time in all temperature region. The randomness effect on the dimer Mott insulator will produce a soft Coulomb gap. This soft Coulomb gap will be decreased Mott gap in resistivity and lowering resistivity value as shown in Fig. 1.8 (b).

The other experiment, the de Haas-van Alphen (dHvA) effect frequency measurement on κ-(BEDT-TTF)$_2$Cu(NCS)$_2$ also have been reported [1,21]. The dHvA effect measurement can evaluate microscopic changing in the electronic state at the Fermi level which results information are Fermi surface, the effective mass, and the scattering time. By evaluating the scattering time of conduction, the

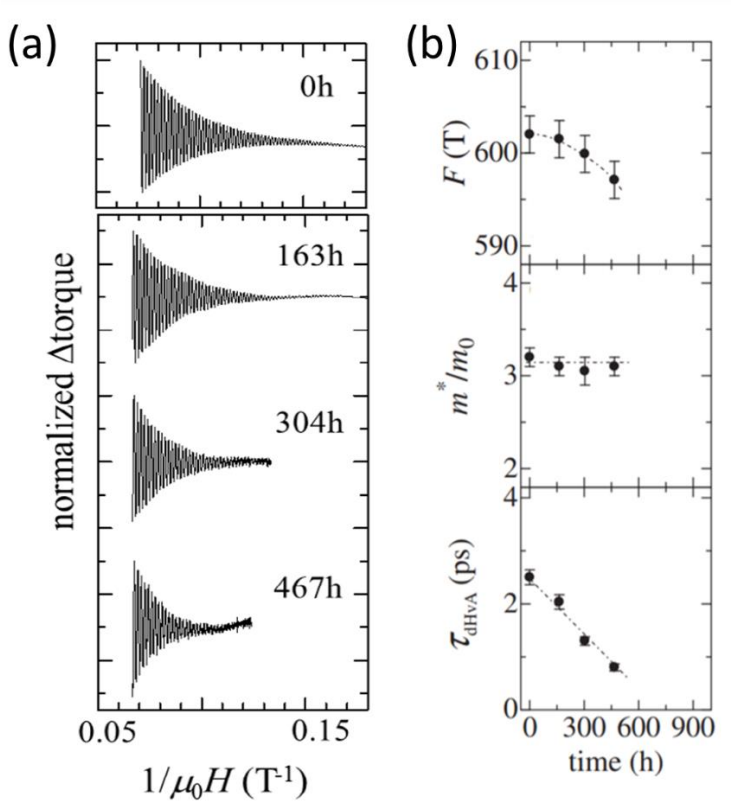

Fig. 1. 9 Effect of X-ray irradiation on κ-(BEDT-TTF)$_2$Cu(NCS)$_2$ (a) Changes in de Haas-van Alphen oscillations. The frequency is hardly changed by X-ray irradiation. (b) Parameter changes in de Haas-van Alphen such as frequency, effective mass, and scattering time. [1, 21].

effective mass, and the scattering time. By evaluating the scattering time of conduction, the randomness introduced by X-ray irradiation effect into metallic state and the suppression of conductivity can be investigated [1]. Fig 1.9 shows that the magnitude of frequency decreasing about 1% with X-ray irradiation time 467 hours and the frequency changing can be ignored. The result indicates that the Fermi surface is hardly changed by X-ray irradiation. In addition, the effective mass is hardly changed by the X-ray irradiation which mean the intensity of electron correlation is also do not change. The last result is the scattering time is decreasing with increasing irradiation time which cause by potential modulation from molecular defect in the anion layer [1]. In conclusion, it is considered that X-ray irradiation has almost no influence on the number of carriers, the bandwidth, and it is only introducing disorder into the sample. Thus, in the recent report, the results show that X-ray irradiation can introduce molecular defects into anion molecules, especially CN bonds, and introduce and control disturbances to the π electron system responsible for conduction in the BEDT-TTF layer.

Chapter 2 Motivations and purpose of study

In this Doctoral dissertation, I prepared (BEDT-TTF)Cu[N(CN)$_2$]$_2$ as BEDT-TTF based organic compound with a 1:1 ratio between donor and acceptor molecules. The organic salts with 1:1 donor/anion molecule ratio on stoichiometry can generates a half-filling energy band. In the case of 2:1 BEDT-TTF organic salts, a site consists of a dimer between two molecules with intra-dimer degree of freedom. However, in the 1:1 BEDT-TTF organic salts, a site is comprised by only one molecule thus direct study of donor-to-anion is possible. It is important to find another BEDT-TTF organic salts with 1:1 ratio because it can be used to directly study (BEDT-TTF)$^+$ donor molecules itself, and possibly gives new information on the transition of MI to QSL. (BEDT-TTF)Cu[N(CN)$_2$]$_2$ is expected to have a half-filled energy band with Mott insulating behavior. Until today, there is no in-depth study about the fundamental properties.

A recent study shows that x-ray irradiation on (BEDT-TTF)$_2$*X*, the results show that CN-bond defects will occur in anion layer and the defects work as a random potential to the conduction electrons in BEDT-TTF molecule layer. This random potential is known as the randomness effect which creates Anderson-type electron localization. On the other hand, the randomness effect may give a different result on Mott insulator, which will produce a soft Coulomb gap. Both behaviors can be observed clearly by resistivity measurements [1]. However, there is a possibility that irradiation effects can affect the dimer structure itself which will disturb effective half-filling dimer band. From this assumption the question arises, will the 1:1 donor/anion i.e., (BEDT-TTF)Cu[N(CN)$_2$]$_2$ show the same behavior when irradiated by x-ray as in (BEDT-TTF)$_2$*X*? The simple tool to find out the disorder effect on the material causes by X-ray irradiation is by using resistivity measurement. From this measurement, we can know how electronic transport behaves on the Fermi surface.

In this study, I will study fundamental properties of (BEDT-TTF)Cu[N(CN)$_2$]$_2$ i.e., electronic, optical, and magnetic properties. It is important confirm of half-filling band, genuine Mott insulating state, and one-dimensionality of this compound from fundamental properties. Furthermore, the investigation of the detail of magnetic nature and mechanism of magnetic order found in the one-dimensional zig-zag chain structure is also important. Therefore, this Doctoral dissertation will consist with several chapters. The in-depth detail crystal structure and energy band structure will be presented in chapter 3. The fundamental properties will explain in chapter 4 for electronic and optical properties and chapter 5 for magnetic properties. In chapter 6, the study of x-ray irradiation effect on the fundamental properties (BEDT-TTF)Cu[N(CN)$_2$]$_2$. The other x-ray irradiation effect in other fundamentals properties such as optical and magnetic properties will also presented in chapter 6.

Chapter 3 Synthesis, crystal structure and band calculations

In this chapter, the crystal and energy band structure of (BEDT-TTF)Cu[N(CN)$_2$]$_2$ will be explained. Also, the method for synthesizing of single crystal of this compound will briefly explain. (BEDT-TTF)Cu[N(CN)$_2$]$_2$ is a 1:1 (BEDT-TTF)*X* based organic compound that has a different crystal structure compared to (BEDT-TTF)$_2$*X*. The differences in the crystal structure can lead to different phenomena in the material. Because of (BEDT-TTF)Cu[N(CN)$_2$]$_2$ has natural half-filling band which is this compound is a candidate for a genuine organic Mott insulator.

3.1 Single crystal growth

Wan *et al*. first reported the crystal growth process of (BEDT-TTF)Cu[N(CN)$_2$]$_2$ using electro-crystallization [14]. In previous work by Wan *et al*., (BEDT-TTF)Cu[N(CN)$_2$]$_2$ is an unwanted byproduct of κ-(BEDT-TTF)2Cu[N(CN)$_2$]Cl, a (BEDT-TTF)$_2$*X*- based organic compound. They tried to minimize the byproduct by using several types of solutions. However, in this PhD thesis, the current sample is (BEDT-TTF)Cu[N(CN)$_2$]$_2$. In the Wan *et al*. reported paper, there are two main electrolyte solutions that produce (BEDT-TTF)Cu[N(CN)$_2$]$_2$. The first solution is a mixed of BEDT-TTF, CuCl and PPh$_4$[N(CN)$_2$] and the second solution is a mixed of BEDT-TTF, CuCl, PPh$_4$[N(CN)$_2$], and N(hexyl)$_4$Cl. The second solution gives high production of κ-(BEDT-TTF)2Cu[N(CN)$_2$]Cl, and slow growth conditions with low current density and good amount of Cl^- will also increase production. Therefore, to get better production organic salt (BEDT-TTF)Cu[N(CN)$_2$]$_2$, we modified the type of solution and electro-crystallization method.

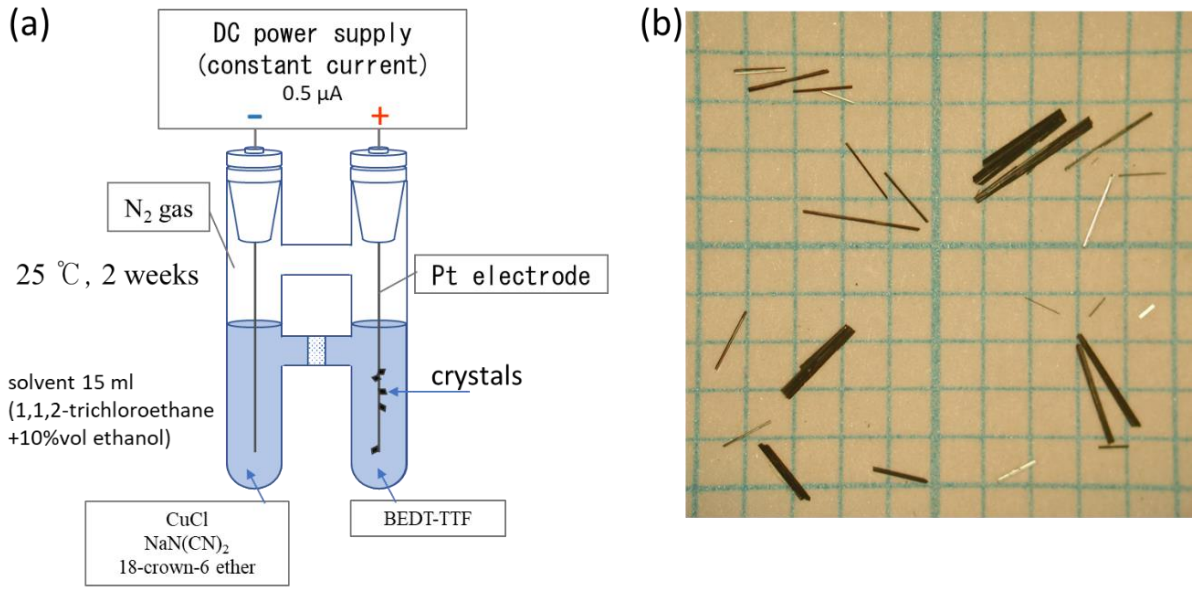

Fig. 3. 1 (a) Schematic of synthesize method for crystal growth (BEDT-TTF)Cu[N(CN)$_2$]$_2$. (b) crystal morphology of (BEDT-TTF)Cu[N(CN)$_2$]$_2$. The single crystal morphology has a needle-like structure.

The schematic of crystal growth synthesized process is shown in Fig. 3.1 (a). The crystal growth by was prepared by using reagents BEDT-TTF (ET), CuCl, $NaN(CN)_2$, and 18-crown-6 ether which we modified electrolyte solutions from reported paper by Wan *et al*.. The current density is set to be 0.5 μA which higher than reported paper, 0.1 – 0.2 μA. Also, the crystal growth condition is rather fast compared to reported paper which expected to give higher production of $(BEDT\text{-}TTF)Cu[N(CN)_2]_2$. The crystal morphology of $(BEDT\text{-}TTF)Cu[N(CN)_2]_2$ is very different compared to its counterpart. $BEDT\text{-}TTF)Cu[N(CN)_2]_2$ has a shiny black needle-like shape as shown in Fig. 3.1 (b), while κ-$(BEDT\text{-}TTF)_2Cu[N(CN)_2]Cl$ has rhombic plates shape.

3.2 Crystal structure

$(BEDT\text{-}TTF)Cu[N(CN)_2]_2$ has monoclinic crystal structure and C2/c space group with $Z = 4$ independent molecules. According to Wan *et al*., long axis of crystal morphology is *c*-axis direction. The lattice parameters measured by XRD at 300 K are a = 16.756(3) Å, b = 13.975(3) Å, c = 10.340(2) Å, β = 124.145(10)°, and volume = 2003.9(7) $Å^3$ with R= 4.01%. For low temperature measurements of XRD at 93 K, the lattice parameters are a = 16.783(3) Å, b = 13.816(3) Å, c = 10.311(16) Å, β = 124.145(10)° and volume = 1986.3(6) $Å^3$ with R= 3.74%, where almost no indication of parameters change with the high temperature. Both lattice parameters are comparable with the previous reported study [13]. Fig. 3.2 shows crystal structure of $(BEDT\text{-}TTF)Cu[N(CN)_2]_2$. In the $(BEDT\text{-}TTF)_2X$, the organic compound shows clear alternating layer of BEDT-TT molecule as conducting layer and anion *X* and insulating layer. While in $(BEDT\text{-}TTF)Cu[N(CN)_2]_2$, this crystal structure does not have alternating layer of BEDT-TT molecule. Instead, the BEDT-TTF has unique arrangement in the 3D network. Also, the anion molecule has infinite chain along $a + c$ direction with tetrahedral formation between copper atom with nitrogen atoms.

In the organic base compound, intermolecular distance creates overlapping of π orbital is a pathway for electronic conduction which will determine electronic properties in the compound. This distance should less than van der Waals distant i.e., 3.60 Å [65]. In the BEDT-TTF based organic

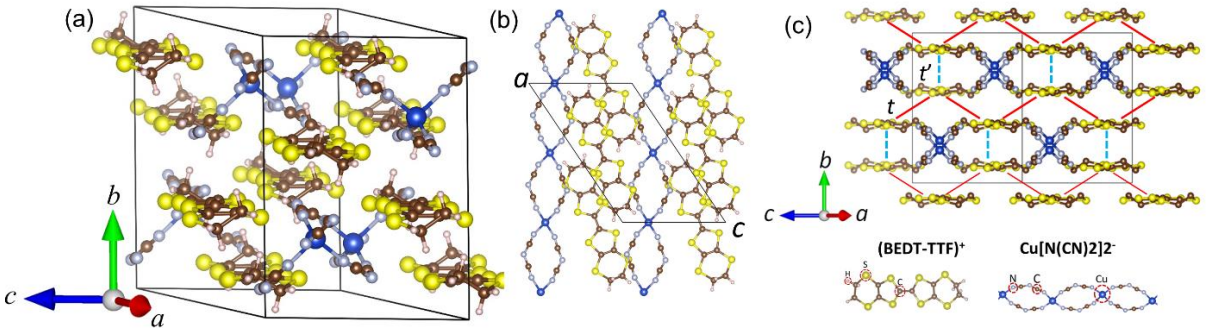

Fig. 3. 2 (a) Crystal structure of $(BEDT\text{-}TTF)Cu[N(CN)_2]_2$ at room temperature (from ref [13]). (a) Crystal structure in the *ac* plane. Infinite chain-like polymeric $Cu[N(CN)_2]_2^-$ anion at the $(a + c)$ direction. (c) Crystal structure view from $a + c$ plane. Red line corresponds to shortest distance of S-S contact. Blue dashed line corresponds to longest distance of S-S contact. Transfer integral *t* (red line) and transfer integral *t*' (blue line) from DFT calculation.

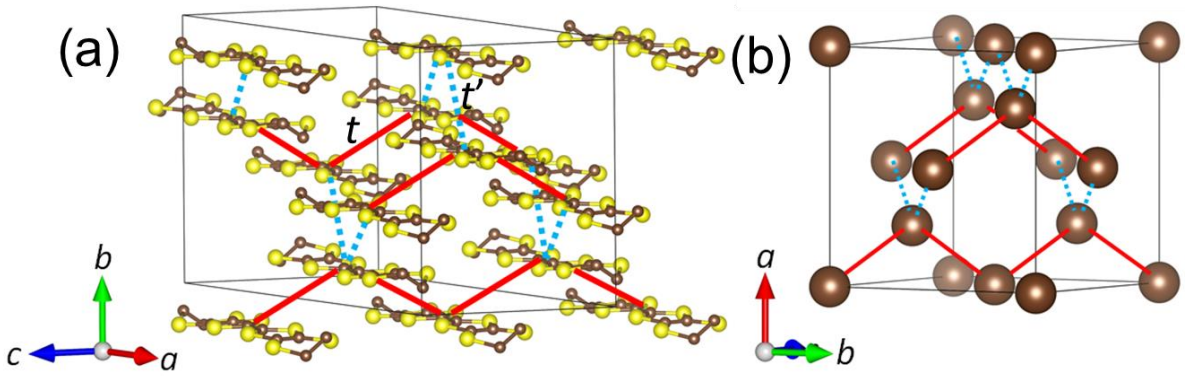

Fig. 3. 3 (a) 3D network arrangement of BEDT-TTF via S-S contact in the crystal structure as distorted diamond structure. Transfer integral *t* (red line) and transfer integral *t*' (blue line). (b) Diamond lattice corresponds to transfer integral *t* and transfer integral *t*'.

compound, π orbital come from sulfur atoms and carbon atoms which mean electronic properties determine by BEDT-TTF molecule. The shortest intermolecular distance of (BEDT-TTF)Cu[N(CN)$_2$]$_2$ is between sulfur-to-sulfur atoms named S-S contact. The shortest S-S contact is 3.63 Å along *c* direction and the longest is 3.98 Å at the *b* direction as shown in Fig. 3.2 (c). The other shortest distance is happened between BEDT-TTF molecule with Cu[N(CN)$_2$]$_2^-$ i.e., sulfur atom to nitrogen atom is 3.17 Å and sulfur atom to carbon atom is 3.19 Å. The shortest S-S contact in this compound is rather long compared to (BEDT-TTF)$_2$*X*. Compared to its counterparts, (BEDT-TTF)Cu[N(CN)$_2$]$_2$ has semiconductive electronic properties. Even though, (BEDT-TTF)Cu[N(CN)$_2$]$_2$ has semiconductive electronic properties, the BEDT-TTF based organic molecules are well-known have strongly correlated electron system. Therefore, the electronic properties of this compound will dictate by BEDT-TTF molecule. Together with natural Half-filling from (BEDT-TTF)Cu[N(CN)$_2$]$_2$, resulting this compound as a genuine candite for organic Mott insulator.

By connecting BEDT-TTF^{+1} donor molecule to their nearest neighbor via S-S contact, this connection creates a tetrahedral arrangement which similar to diamond lattice structure. However, because this arrangement is connected by two different S-S contact, this 3D arrangement is true diamond lattice, i.e., distorted diamond lattice structure. This comparison arrangement is shown in Fig. 3.3. The connection of S-S contact with distance 3.63 Å is expected to be a dominance in electronic properties, resulting (BEDT-TTF)Cu[N(CN)$_2$]$_2$ has a zig-zag chain along the *c* direction. To better understand the electronic properties, the band structure calculate from room temperature crystal structure will presented in the next section.

3.3 Band structure calculations

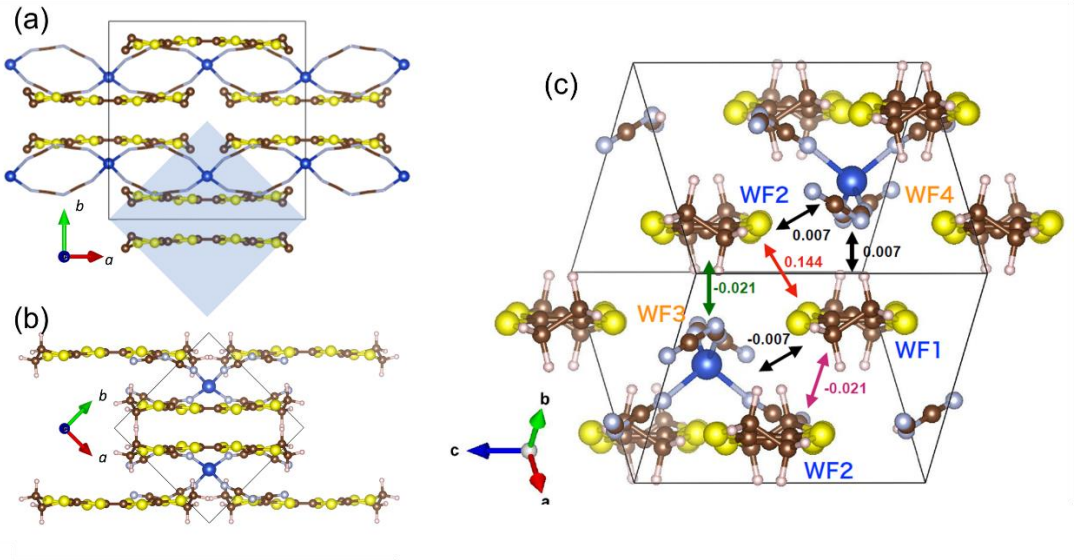

Fig. 3. 4 (a) Crystal structure of (BEDT-TTF)Cu[N(CN)$_2$]$_2$ in the *ab* plane. Blue square is a primitive cell area. (b) Primitive cell of crystal structure of (BEDT-TTF)Cu[N(CN)$_2$]$_2$ in the *ab* plane. (c) Transfer integral directions from the DFT band structure with Wannier function in the primitive cell.

The tight binding approximation and First principle DFT band calculation was done with crystal structure of (BEDT-TTF)Cu[N(CN)$_2$]$_2$ at room temperature. The results, figures and analysis are provided from Prof. N. Yoneyama extended Hückel method and the tight binding approximation, Dr. T. Tsumuraya for DFT band structure calculation [66]. The crystal structure of monocline C/2 of this compound is reduced to its primitive cell as shown in Fig. 3.4. The lattice parameters from primitive cell of a = 10.89 Å, b = 10.89(3) Å, c = 10.279 Å, $\alpha = \beta$ = 115.4510°. There are 2 independent BEDT-TTF molecule in the primitive cell. The value and the direction of transfer integral can be got from extended Hückel method, and DFT band calculation with the Wannier function WF [67] each BEDT-TTF interaction as shown in Fig. 3.4 (c). From extended Hückel method, the direction of t = −0.192 eV and t' = +0.0229 eV from the shortest and the longest S-S contact, respectively. From DFT and Wannier function WF, the transfer integral energy direction is also shortest and the longest S-S contact with value t = −0.192 eV and t' = +0.0229 eV, respectively as shown in Fig. 3. 4 (c). Both results values are comparable to each other. (BEDT-TTF)Cu[N(CN)$_2$]$_2$ is considered as one-dimensional (1D) zig-zag chain along the c direction due to ratio of $t'/t \approx 0.1$ where the value of transfer integral t is the strongest interaction and t' is the weakest interaction.

Fig. 3.5 shows band structure from tight binding approximation and DFT calculation. In tight binding approximation, there are two band dispersions come from 2 equivalent BEDT-TTF molecules which Fermi level is located at the middle of HOMO band by viewing as one electron transfer HOMO of BEDT-TTF molecule to its anion molecule. By neglecting t' due to its small value, the band dispersion become:

$$E_{\pm}(k) = \pm 2[\mathrm{tcos}(k_c c/2)] \quad (3.1)$$

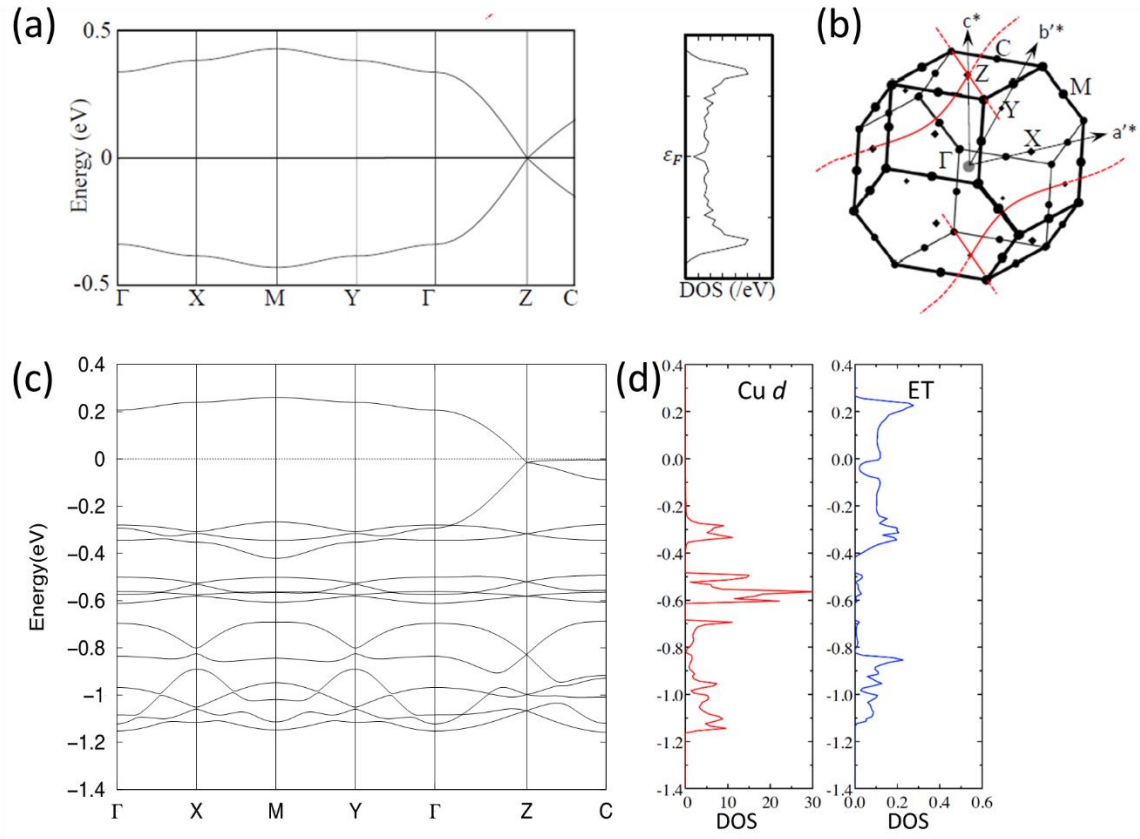

Fig. 3. 5 (a) Band structure calculation from the tight binding approximation. The side figure is density of state from tight calculation. (b) First Brillouin zone for primitive cell. The red line is nodal line from the tight binding approximation dispersion equation. (c) Band structure from first principle DFT calculation. (d) Partial DOS (density of state); red line curve from Cu *d* orbital of anion part and blue line curve from TTF (tetrathiafulvalene) of BEDT-TTF.

The band dispersion shows that 1D-Fermi nodal (00π) surface on Z with linear energy dispersion at around the 1st Brillouin zone as shown in Fig. 3.5 [66]. The crossing at Z point nodal because weak t' break 1D Fermi degeneracy and leave nodal line orthogonally crossing. The two nodal lines, when included t', give linear along the b* direction and bending along the a* direction in the Fig. 3.5 (b) shows that the nodal point features not from diamond structure t' but from uniform zig-zag chain pattern from transfer integral *t* along *c*-axis direction. This mean this material is quasi-1D material. When the change occurs at the zig-zag chain in the crystal structure e.g., dimerization of BEDT-TTF, the gap formation on all the nodal lines easily occurs [66]. The band structure from DFT calculation also shows similar result with a Dirac cone-like appears at Z point as shown in Fig 3. 5 (c). Band structure around -0.3 eV consisted of Cu band and BEDT-TTF band. These two bands are not mixed, wherein partial DOS (density of state) calculation of both parts have the peak dispersion around -0.3 eV, as shown in Fig. 3.5 (d).

Chapter 4 Electronic and optical properties

(BEDT-TTF)Cu[N(CN)$_2$]$_2$ has 1:1 donor/anion i.e., BEDT-TTF$^+$ and Cu[N(CN)$_2$]$_2^-$, molecule ratio on stoichiometry which generates a half-filling energy band. According to the Hubbard model, Mott insulating state only occurs in the half filling band structure with large Coulomb energy *U*. In this chapter, we investigate electronic and optical properties of (BEDT-TTF)Cu[N(CN)$_2$]$_2$ by using resistivity measurement and IR reflectivity measurement to confirm this material as genuine Mott insulator.

4.1 Experimental methods

Resistivity measurements were measured using the two-probe method with an electrometer and a constant voltage equal to 1 V, where the apparatus can measure resistance up to 10^{18} Ω (Appendix AP. 1). A single crystal of (BEDT-TTF)Cu[N(CN)$_2$]$_2$ with dimensions $0.01 \times 0.01 \times 3$ mm attached with gold wire using carbon paste along long axis crystal or *c* direction, and the gold wire attached to measurement probe using silver paste as shown in Fig. 4.1 (a). The sample is placed inside the mounting probe with shielding made by cooper material, which this mounting probe will put inside to LN2 vessel as a cooling system. The cooling rate is using 1 K/min with copper wire is a heating element wrapped around the body part of the mounting probe and temperature control uses D6039505 as a sensor. The other measurement is to check anisotropic behavior in resistivity (BEDT-TTF)Cu[N(CN)$_2$]$_2$. For anisotropic measurement, the measurement was performed using same method with gold wire attached to both short axis of crystal as shown in Fig. 4.1 (b).

The optical properties measurement using Fourier transform infrared (FT-IR) in far-, mid-, near-infrared regions and a grating spectrometer for UV-Visible region. For FTIR measurement at mid-region with temperature dependences were performed in SPring-8, Japan Synchrotron Radiation Research Institute at BL43IR beam. Temperature dependence of IR reflectivity measurement were performed using Hyperion microscope and IR VERTEX 70 machine, and temperature control using a He-flow cryostat (Oxford Instruments) with KBr window. The sample is one single crystal with dimensions crystal is $0.01 \times 0.04 \times 0.6$ mm as shown in Fig. 4.1 (c). The anisotropic IR reflectivity

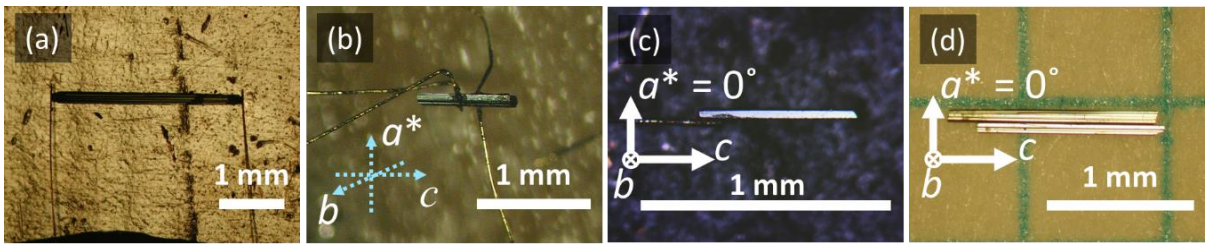

Fig. 4. 1 Two probes method resistivity measurement on the single crystal. (b) Resistivity measurement for anisotropic check on the single crystal. *a**, b, and c are morphology direction on the single crystal. (c) Single crystal (Sample No 1) for IR reflectivity measurement with temperature dependence. (d) Two single crystals (Sample No 2) for anisotropic IR reflectivity measurement

measurement is using IRT-5200TKS and FT/IR 6600 (Jasco). The measurement used two single crystals to amplify the reflectivity resolution for avoiding inference results from thin morphology of needle-like crystals as shown in Fig. 4.1 (d).

4.2 Electrical resistivity

Fig. 4.2 (a) shows the resistivity of (BEDT-TTF)Cu[N(CN)$_2$]$_2$ at all crystal morphology directions, which *a** is given direction that perpendicular with other crystal morphology directions. The result of resistivity shows resistivity increased with decreasing temperature and the sample is highly insulating compared to the other BEDT-TTF organic based compound i.e., κ-(BEDT-TTF)$_2X$, in the low temperature regions. [25]. There is no indication of phase transition that observed in the resistivity results, such as sudden jump or hysteresis result between cooling and heating condition [24]. The resistivity at *c* direction has less resistance compared to the other crystal morphology directions. To understand transport properties in the material, the transport mechanism in electrical resistivity can be observed by Arrhenius law,

$$\rho = \rho_0 e^{\left(\frac{E_a}{k_B T}\right)} \tag{4.1}$$

where ρ_0 (Ωcm) is an extrapolation of resistivity in higher temperature, k_B is Boltzmann constant, and E_a is activation energy, where the activation energy E_a is related to the band gap energy $E_g = 2E_a$ [34]. The activation energy also related to the mechanism of transport from the carrier charge, which driven by thermal activation when temperature decreases. Therefore, activation energy also can be defined as the depth of the electronic level of electron around the edge band, conduction band and valence band [34, 35]. The resistivity results plotted in the Arrhenius plot and the Arrhenius fitting eq. 4.1 are represented as the red lines in the Fig. 4.2 (b). The resistivity results in Fig. 4.2 (b) show linear behavior in the low temperature regions which properly fit by Arrhenius law fitting from 85 K and 125 K. The result of Arrhenius fitting parameters is described in Table 4.1.

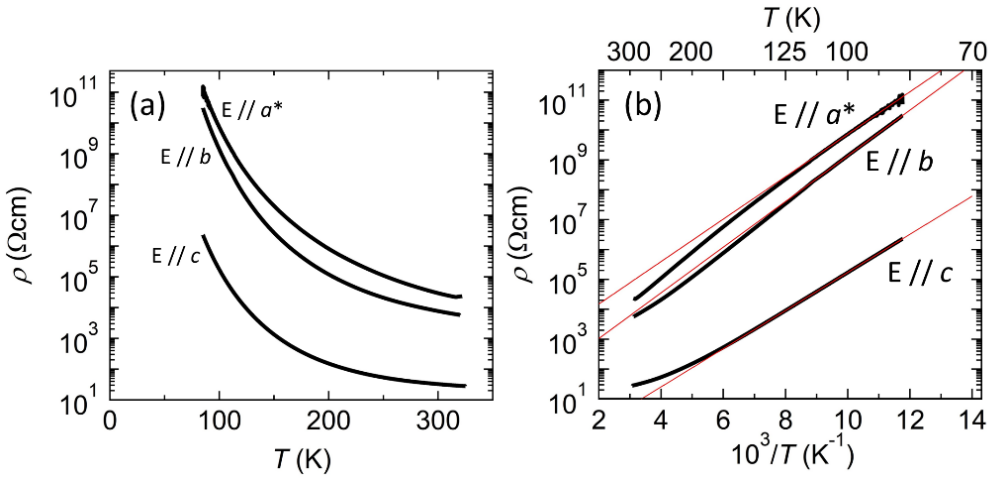

Fig. 4. 2 (a) Temperature-dependence of resistivity of (BEDT-TTF)Cu[N(CN)$_2$]$_2$ at different crystal morphology directions *a**, *b* and *c* as shown in Fig. 4.1 (b). (b) Arrhenius plot of Temperature-dependence of resistivity. The red line is fitting function from eq. 4.1.

Table 4.1 Arrhenius eq. 4.1 parameter of pristine crystal (BEDT-TTF)Cu[N(CN)$_2$]$_2$

Sample	Direction	$E_g = 2E_a$ (eV)	ρ_0 (Ωcm)
H. H. Wang [14]	*c*	0.26	-
Sample 1	*c*	0.28	0.26
Sample 2	*c*	0.28	0.26
Sample 3	*c*	0.26	0.07
Sample 3	*a**	0.31	140
Sample 3	*b*	0.32	13.4

Energy E_g for all crystal morphology directions on average are almost similar to each other, which equal to 0.3 eV. The energy E_g fitting results for each sample is comparable to the previous study by Wang *et al*. proving the samples to be reliable. Also, the value of energy E_g is rather small to categorize this compound as insulator. The parameter ρ_0 also supports that c is the most conductive and *a** is more insulating compared to other directions. This result indicates that with same amount of activation energy, at *c* direction to achieve high resistivity is much harder to excited electron to conduction band compared to the other contact. In the energy band calculations in chapter 3, there is no visible energy gap in the energy band structure and density of state (DOS). Instead, the nodal point from band structure can be considered as semi-metallic behavior from this compound. Although there is small appearance of gap in the DOS, the size of this energy gap is smaller compared to the E_g from Arrhenius law. Therefore, it saves to assume that there is no indication energy gap in the band structure calculations. From half-filling energy band and semi-metallic behavior, the best scenario for the electronic properties of this compound is Mott insulator with the strong on-site Coulomb interaction *U*. In addition, electron-electron interaction *U* along *c* direction is higher than any directions as shown by high anisotropy value on ρ_0 ($\rho_c \ll \rho_b \leq \rho_{a^*}$). This result is consistent with the quasi-one-dimensional system (quasi-1D) from the crystal and band structure analysis in chapter 3. There is a slight nonlinearity above 200 K at all crystal morphology directions. This nonlinearity is reproducible in the other several single crystals of current batch samples. The most probable explanation would be above this temperature regions Mott temperature transition occurs. For instance, Mott insulator in the inorganic material i.e., V_2O, shows sudden drop in conductivity results occur below 300 K. On the other hand, a static conductivity can be seen with higher-order around 10^{-4} Ωcm at a higher temperature. The result indicates that Mott insulating state occur at $T > T_{MI} \sim 333$ K, which this material became a good conductor (MI denotes metal-insulator) [32-33]. This can be concluded that the metallic state of (BEDT-TTF)Cu[N(CN)$_2$]$_2$ can be observed at a higher temperature.

4.3 Infrared optical reflectivity

4.3.1 Polarization angle dependence

The optical reflectivity can be used to analyze vibrational mode from the molecular structure and charge excitation. The Anisotropic behavior of reflectivity can be check using polarization angle dependences, which the angle is related with the incident light direction of IR to the crystal surface. By using different light incident, it can be used to check unique vibrational mode of molecules at certain

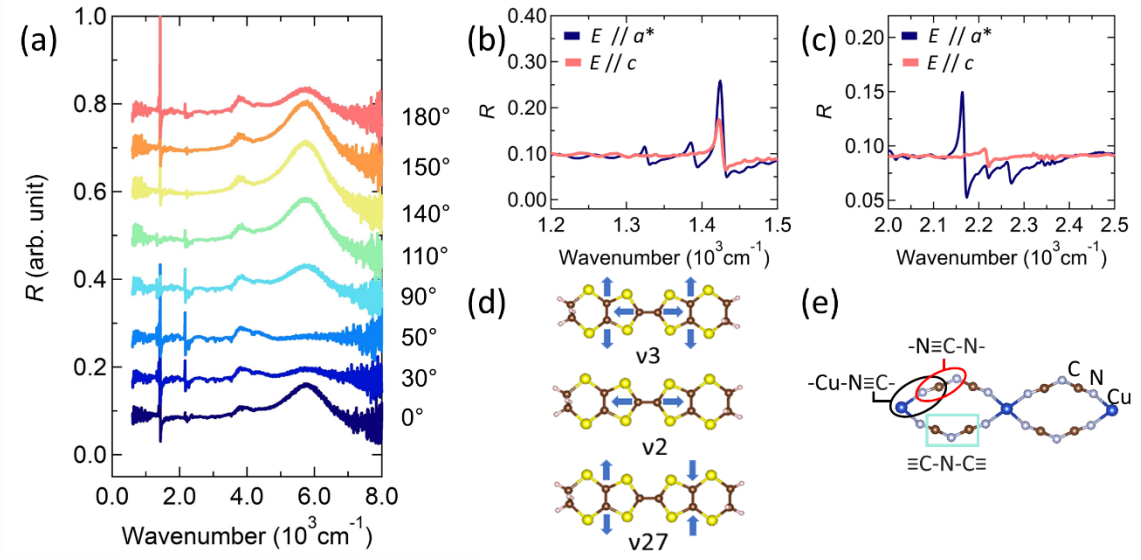

Fig. 4. 3 (a) Polarization angle dependence of reflectivity of at mid- region. (b) Reflectivity of vibration mode *v*3, *v*27 and *v*2 C=C bond of BEDT-TTF. (c) Reflectivity of stretching mode C≡N and C-N from anion molecule $Cu[N(CN)_2]_2^-$. (d) Vibrational mode of BEDT-TTF molecule: symmetric *v*3 (top), *v*2 (middle) and antisymmetric *v*27 (bottom). (e) CN bond in the anion molecule $Cu[N(CN)_2]_2$.

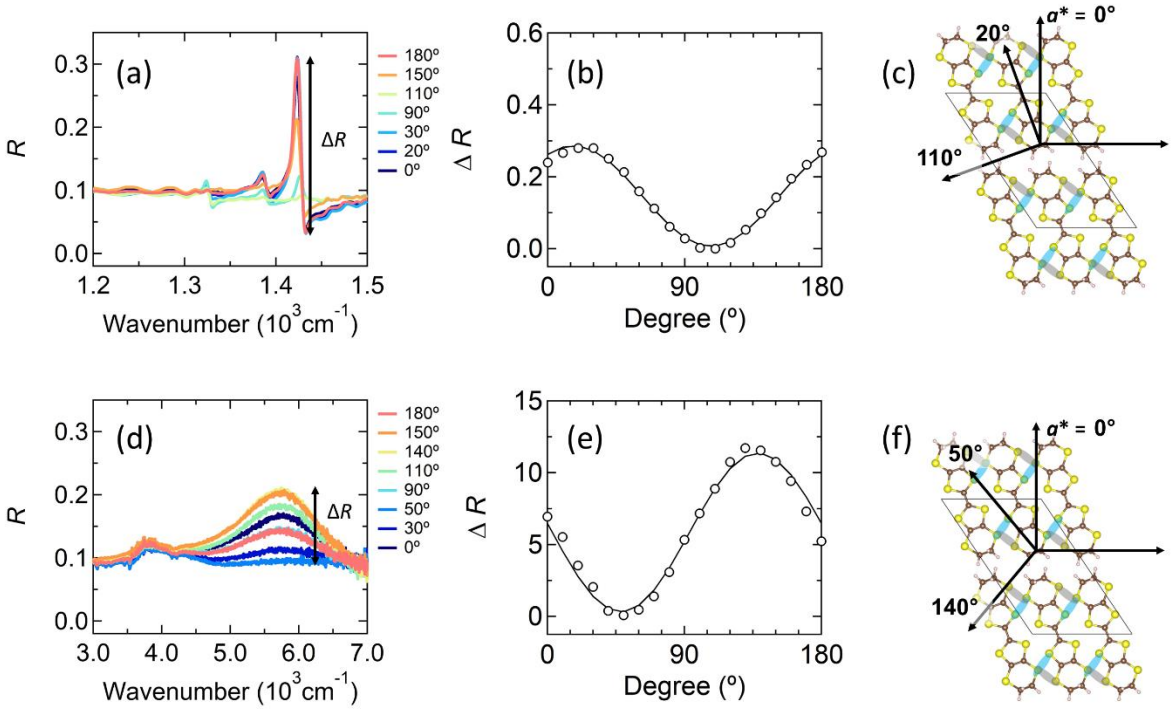

Fig. 4. 4 (a) Reflectivity of polarization angle dependence in BEDT-TTF vibrational mode. (b) Sinusoidal relation between the Δ*R* of vibration mode *v*2 with polarization degree (˚). (c) *ac* plane of crystal corresponds to maxima and minima angle dependence of vibration mode *v*2. (d) Reflectivity of polarization angle dependence of charge excitation Hubbard band and isotropic band. (d) Sinusoidal relation between the Δ*R* of Hubbard band with polarization degree (˚) (c) *ac* plane of crystal corresponds to maxima and minima angle dependence of Hubbard band. Δ*R* is total intensity from top peak to the bottom peak. Blue and gray circle are intermolecular distant between two atom Sulfur or S-S with distance value 3.6309 Å and 3.9408 Å, respectively.

crystal plane, and anisotropic behavior of charge excitation. In this measurement, 0˚ direction is short axis of crystal morphology, which was labeled as *a** direction. In addition, the measurements used two single crystals to avoiding inference results from thin morphology of needle-like single crystals as shown in Fig. 4.1 (d). Fig. 4. 3 shows reflectivity *R* measurement result with different polarization angle. There is anisotropic behavior from vibrational mode of BEDT-TTF from 1200 to 1500 cm^{-1}, stretching mode of CN bond from anion molecule from 2000 to 2500 cm^{-1}, and two charge excitation peaks from 3500 to 7000 cm^{-1}. Fig. 4. 3 (b) and (c) show details of vibrational mode of BEDT-TTF and stretching mode of CN bond, respectively. There are three vibrational modes of C=C as in Fig. 4. 3 (d) have been observed from reflectivity: 1323.9 cm^{-1}, 1384.6 cm^{-1}, and 1423.2 cm^{-1} which are symmetric mode $\nu 3$, antisymmetric mode of $\nu 27$ and symmetric mode $\nu 2$, respectively [82]. The stretching mode of CN bond as in Fig. 3 .4 (e) lies at 2163.8 cm^{-1}, 2212.9 cm^{-1}, and 2262.1 cm^{-1}. According to the Drodova *et al*., stretching mode at 2163.8 and 2212.9 cm^{-1} should be identified as out-of-phase and in-phase vibration mode of two C≡N groups from the same $N(CN)_2$ ligand type [83].

The vibrational mode of $\nu 2$ is the strongest and of $\nu 3$ is the weakest compared to the other vibrational mode as shown in Fig. 4. 4 (a). Although $\nu 2$ and $\nu 3$ is Raman active spectra, the appearance of $\nu 2$ and $\nu 3$ in IR reflectivity might be due to the reduction of molecular symmetry in the crystal, vibration of A_2 symmetry type [84]. Fig. 4. 4 (b) shows the relation between the anisotropic behavior of intensity ΔR from vibration mode $\nu 2$ with a sinusoidal function of IR light incident. The maxima and minima value of ΔR lie at 20˚ and 110˚, respectively. In the Fig. 4. 4 (c), the IR incident light at 20˚ direction is parallel with the long axis of the BEDT-TTF molecule in the ac plane, which gives the strongest reflectivity *R* vibration mode $\nu 2$ because symmetrical C=C stretch mode happens along long axis molecules (in Fig. 4. 4 (d)). On the contrary, when Polarizer at 110˚, IR incident light is perpendicular with long axis molecules resulting in no IR absorption in this direction, or ΔR becomes flat. Therefore, the crystal plane for optical reflectivity measurement is *ac* plane.

The two peaks in Fig. 4. 4 (d) around 4000 cm^{-1} and 5660 cm^{-1} is charge excitation from $(BEDT\text{-}TTF)Cu[N(CN)_2]_2$. The large peak at 5660 cm^{-1} is charge excitation come from natural Coulomb interaction or Hubbard band of molecule BEDT-TTF, where the theoretical calculation value of Coulomb interaction *U* is around 0.7 eV [51]. The origin of charge excitation from the small peak at 4000 cm^{-1} or 0.4 eV might be coming from the energy gap from electronic properties ≈ 0.3 eV because this peak charge excitation has isotropic behavior, and the order of values is relatively close to transport energy gap. Fig. 4. 4 (e) shows the relation ΔR of Hubbard band with a sinusoidal function of IR light incident. The maxima ΔR of Hubbard band at 140˚ produces the largest Hubbard band, while the minima value at 50˚ make Hubbard band disappear or a flat spectrum. The shortest contact of intermolecular BEDT-TTF molecules lies on blue color of two atom Sulfur interactions and the least short contact between two BEDT-TTF lies on gray color of two atom Sulfur interaction as shown in Fig. 4. 4 (e). The shortest contact of S-S will determine π orbital pathways of electronic conduction in the organic compounds. The maxima of Hubbard band at 140˚ is parallel with blue color S-S, while the minima

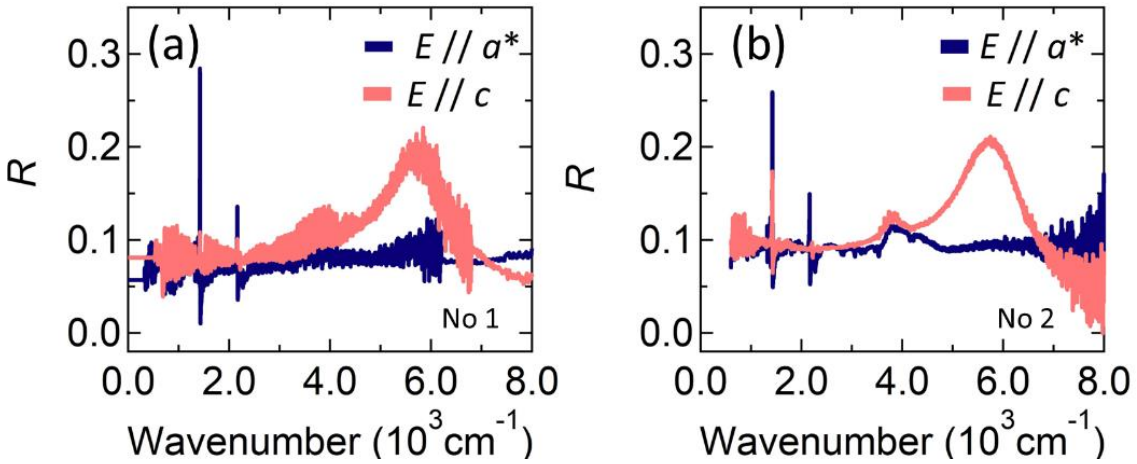

Fig. 4. 5 (a) Reflectivity of one surface single crystal at *c* and *a** direction (sample in Fig. 4.1(c)). (b) Reflectivity of two-surface combination of single crystal at *c* and *a** direction (sample in Fig. 4.1(d)).

value parallel with gray color S-S as shown in Fig. 4. 4 (e). This result is match with transfer integral *t* from extended Hückel method and DFT band lies on this direction (see chapter 3). This explained that Coulomb interaction of π-electron is close to *c*-axis direction resulting Hubbard band has anisotropic behavior in (BEDT-TTF)Cu[N(CN)$_2$]$_2$. The appearance of Hubbard band close to *c* direction and the most conductive direction in resistivity result is *c* direction, strengthening the evidence that (BEDT-TTF)Cu[N(CN)$_2$]$_2$ is a genuine Mott insulator. The anisotropic Hubbard band is also match with anisotropic behavior in resistivity which indicates quasi-1D electronic band structure resulting Hubbard band disappear close to *a** direction.

Fig. 4. 5 shows comparison IR reflectivity measurement with one single crystal surface with two single crystal surface in Fig. 4. 5 (a) and Fig. 4. 5 (b), respectively. IR reflectivity result of one single crystal has inference compared to two single crystal surfaces. The interference occurs because of the ingle crystal of this compound is naturally has thin layer which producing a back-reflectivity interference. This interference makes the IR spectral of charge excitation of isotropic band resolution became low. However, the others vibration mode and Hubbard band spectral sill have good resolution. Although two-surface reflectivity gives better on isotropic charge excitation spectral, this method might affect temperature dependence of IR reflectivity due to occurrence difference of thermal contraction between two crystals and gives measurements at different surfaces. Therefore, one single crystal will used to measure IR reflectivity temperature for uniform thermal contraction. Later, for temperature dependence of optical reflectivity measurement will conducted at *c* and *a** direction.

4.3.2 Temperature dependence of infrared reflectivity

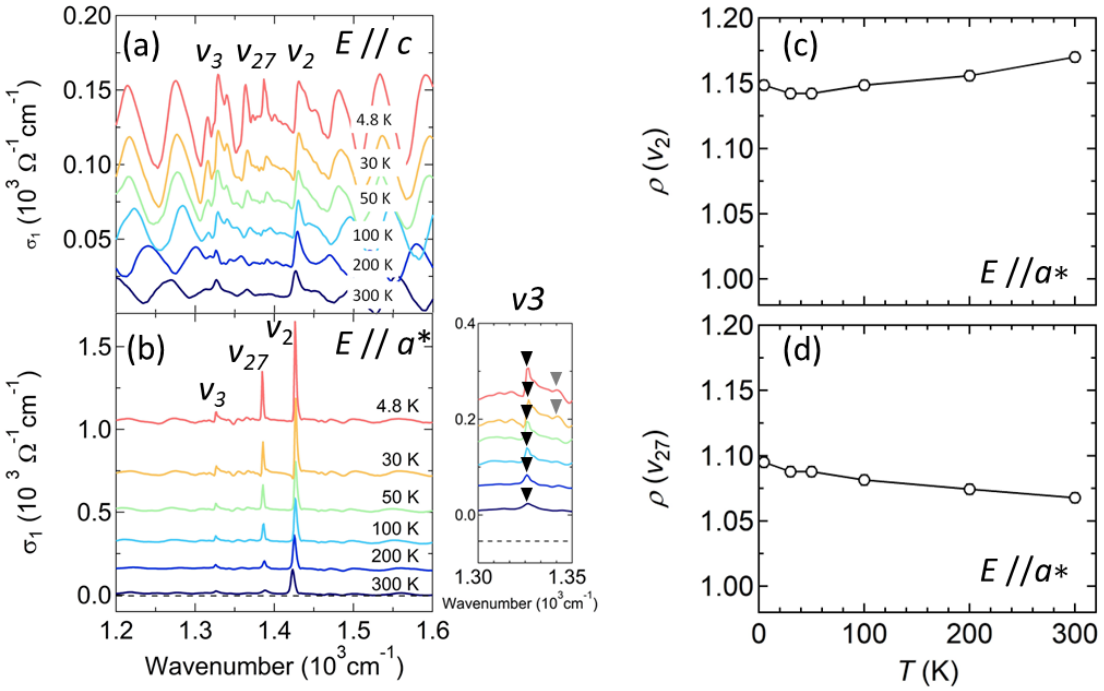

Fig. 4. 6 Temperature dependence of optical conductivity of vibrational mode of BEDT-TTF: (a) at *c* direction, and (b) at *a** direction. Side figure at (b) is zoom in of optical conductivity around vibration mode *v*3 wave number regions. (c) Temperature dependence of charge sensitive from eq. 4.2 on vibration mode *v*2 at *a** direction. (d) Temperature dependence of charge sensitive from eq. 4.3 on vibration mode *v*27 at *a** direction.

Fig. 4. 6 shows temperature dependence of optical conductivity of BEDT-TTF's vibrational mode at *c* and *a** direction. The optical conductivity is obtained from the Kramers-Kronig (KK) transformation of the temperature dependent reflectivity. Fig. 4. 6 (a) shows the optical conductivity for vibration mode *v*3, *v*27 and *v*2 at *c* direction is hardly identified. The splitting of optical conductivity vibration modes *v*3, *v*27 and *v*2 at *c* direction was not convincing enough due to the visible of high interference in optical conductivity. On contrary, the optical conductivity of vibration mode *v*3, *v*27 and *v*2 at *a** direction gives clear identification of peak location. The better resolution of vibration mode at *a** direction might be due to IR light incident almost parallel to BEDT-TTF molecule. In addition, additional peak of vibration mode *v*3 has been observed below 30 K as shown in the side figure Fig. 4. 6 (b). This additional peak of vibration mode *v*3 at *a** might have relation with structural symmetry change of BEDT-TTF molecule. The vibration mode of *v*2 and *v*27 is related to the charge sensitive in BEDT-TTF. The amount of charge in BEDT-TTF molecule can be by empirical relation as below,

$$v2(\mathrm{cm}^{-1})(\rho) = 1447 + 120(1-\rho) \tag{4.2}$$

$$v27(\mathrm{cm}^{-1})(\rho) = 1398 + 140(1-\rho) \tag{4.3}$$

where ρ is charge from vibrational mode wavenumber of *v*2 and *v*27 in cm^{-1} [46]. Because of the chemical composition (BEDT-TTF)Cu[N(CN)$_2$]$_2$ between donor and acceptor molecules 1:1, BEDT-TTF$^+$ is equal to +1 which gives half-filling energy band for this compound. From the empirical eq. 4.3

and 4.4, the charge from both vibrational *v*2 and *v*27 mode is close to +1 at 300 K as shown in Fig. 4. 6 (c) and (d). Both charges from *v*2 and *v*27 have temperature dependence behavior which decreased and increased with decreasing temperatures, respectively. However, the charge changes from 300 K to 4.8 K is around 0.02% for both vibrational modes, which mean Hall-filling energy band is still preserved until low temperature regions. These results of charge sensitive ρ is in good agreement with the characteristic of Mott-insulating state where one charge on one site of BEDT-TTF molecule. There is a subtle kink on the temperature between 30 – 50 K from charge sensitive curve on both Fig. 4. 6 (c) and (d). This kink on the curve might indicates a transition in electronic properties or structural symmetry change of BEDTT-TTF molecule due to temperature dependences. Together with additional peak of vibration mode *v*3 at *a** direction and kink on the temperature dependence of charge curve below 30 K, the structural symmetry change of BEDT-TTF molecule is more possible scenario rather than electronic properties change.

Temperature dependence of Hubbard band and isotropic band of charge excitation at *c* and *a** direction in single crystal is become the main interest to understanding optical properties of (BEDT-TTF)Cu[N(CN)$_2$]$_2$. The temperature dependence of optical conductivity for mid- IR regions in the c and *a** direction is plotted in Fig. 4. 7. The charge excitation peak consists of a large Hubbard band and long-tail peak which might come from the isotropic band. The temperature dependence of optical conductivity shows charge excitation peak of Hubbard band is getting sharper with decreasing temperature. For the isotropic band, the long-tail peak of charge excitation is getting more prominence which the end of long-tail peak located in between 3000 to 4000 cm^{-1}. To distinguish charge excitation Hubbard and isotropic band, two Lorentzian functions are fitted to the optical conductivity curve as shown in Fig. 4. 7 (a). The Lorentzian fitting function $Y(\omega)$ used to analyze the Hubbard and isotropic band as below

$$Y(\omega) = \frac{I\left(1/2\ \Delta H_{1/2}\right)^2}{\left(1/2\ \Delta H_{1/2}\right)^2+(\omega-\omega_0)^2} \tag{4.4}$$

where Lorentzian parameters are *I* is Lorentzian intensity, $\Delta H_{1/2}$ is full width half maximum intensity, and ω_0 is wavenumber of peak center. The spectral weight (SW) is integrated intensity of Lorentzian function is equal to $(\pi/2)I\Delta H_{1/2}$ [CH4_25]. In addition, Sigmoid function $\mathrm{SG}(\omega)$ used for baseline correction to get better fit for Lorentzian function $Y(\omega)$

$$\mathrm{SG}(\omega) = y_0 + \left(\frac{K_1}{1+\exp\left(\frac{\omega a-\omega}{K_2}\right)}\right) \tag{4.5}$$

Therefore, the fitting function become total of $Y(\omega)$ from two peaks charge excitation and $\mathrm{SG}(\omega)$

$$Y_{\mathrm{tot}} = \sum_{i=1}^{n=2} Y_n(\omega) + \mathrm{SG}(\omega) \tag{4.6}$$

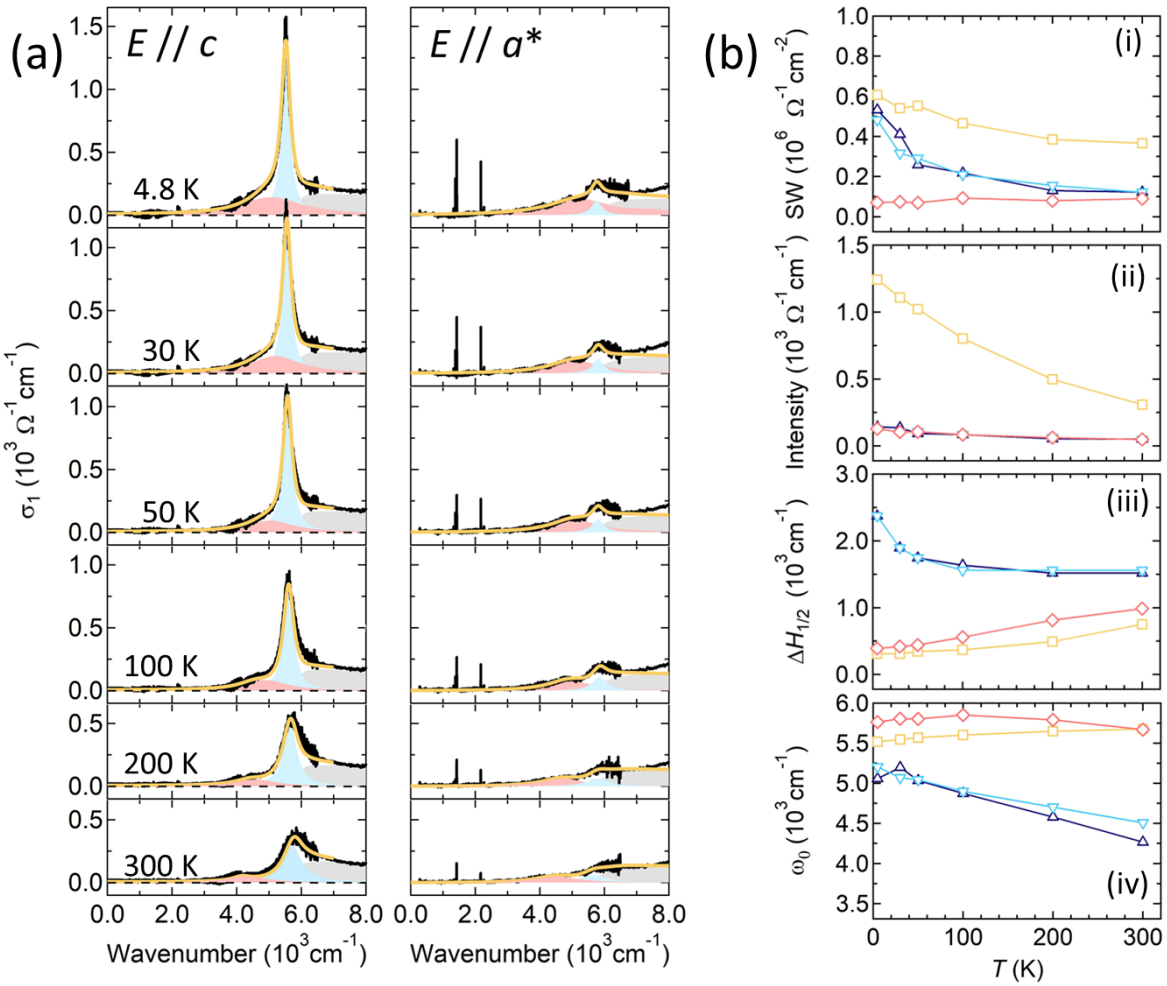

Fig. 4. 7 (a) Temperature dependences of optical conductivity at *c* and *a**direction. Red and blue filled curves correspond to Lorentzian function for isotropic and Hubbard band charge excitation, respectively. Grey filled curve correspond to Sigmoid function for baseline correction (eq. 4.5). Yellow line corresponds to total fitting function (eq. 4.6). (b) Fitting parameters from Lorentzian function (eq. 4.4): (i) Spectral weight (SW), (ii) intensity, (iii) full-width $\Delta H_{1/2}$, and (iv) wavenumber of peak center ω_0. Square, rhombus, triangle up, and triangle down correspond to Hubbard band at *c*-axis, Hubbard band at *a**-axis, isotropic band at *c*-axis and isotropic at *a**-axis, respectively.

The two Lorentzian peaks from fitting results are the red peak attributed to isotropic band around 4000 cm^{-1} and the blue peak attributed to Hubbard band. The details of Lorentzian parameters from fitting results are plotted in Fig. 4. 7 (b). Both *SW* of isotropic and Hubbard band is increased with decreasing temperature, except Hubbard band at the *a** direction remains same. The *SW* of isotropic band for both directions is almost similar to each other and there is sudden increase below 50 K. This sudden increase of SW in the isotropic band due to the $\Delta H_{1/2}$ is become wider below 50 K. The wavenumber of peak center ω_0 for isotropic band at both directions shift toward to the Hubbard band peak. A sharp feature of the Hubbard band excitation peak is evidence of the one-dimensional (1D) Hubbard band excitation. The sharp shape in optical conductivity is also observed in the β'-(BEDT-TTF)$_2$ICl$_2$, which is a quasi-1D electronic structure in 2:1 BEDT-TTF-based organic conductor with strong on-dimer Coulomb repulsion U_D [47]. In comparison of Coulomb interaction, Coulomb interaction U_D of β'-(BEDT-TTF)$_2$ICl$_2$ is estimated to be about 0.4 eV, while in the Coulomb interaction *U* of (BEDT-

TTF)Cu[N(CN)$_2$]$_2$ appears at energy region around 0.7 eV. The Coulomb repulsion U_D is lower than U due to total interaction from onsite Coulomb interaction U, intradimer coulomb interaction V_0, and transfer integral dimer t_d resulting in nearly half of the natural coulomb interaction of BEDT-TTF [48]. The isotropic band shift ω_0 gives a convincing result because the long tail should not originate from the Hubbard band. After all, the Hubbard band should preserve sharp features as a quasi-1D band. From fitting calculation, all optical conductivities at different temperature results show the end of long-tail peak around 3000 cm^{-1}, which mean the optical gap E_g is about 0.4 eV. This optical gap value is also close to the transport gap E_g from the electrical resistivity results, which about 0.3 eV. Therefore, the energy gap of (BEDT-TTF)Cu[N(CN)$_2$]$_2$ electronic and optical properties is a summation of isotropic and Hubbard band. From the DFT calculation results of partial density of state (DOS) from in chapter 3, DOS of donor and acceptor molecules show the Cu *d*-orbital and π-orbital from TTF (tetrathiafulvalene) from BEDT-TTF have energy band that located at the same energy regions around 0.4 eV. This means the energy gap E_g might come from interaction between BEDT-TTF$^+$ cation molecule and Cu[N(CN)$_2$]$_2^-$ anion molecule.

Chapter 5 Magnetic properties

In this chapter, we investigate magnetic properties of (BEDT-TTF)Cu[N(CN)$_2$]$_2$ which has an intrinsic half-filling band structure resulting in a genuine Mott insulator. Until today, there is no in-depth study about the magnetic properties of (BEDT-TTF)Cu[N(CN)$_2$]$_2$. By using a dc magnetization measurement and ESR spectroscopy, we will confirm the magnetic ground state of this organic salt. We will discuss additional ESR parameters together with other experimental results. The results are suggested that an alternating chain occur in organic salt together with opening gap of spin susceptibility resulting spin-singlet transition.

5.1 Experimental methods

The dc magnetization was measured by SQUID magnetometer. The temperature dependence of magnetic dc susceptibility was measured by SQUID magnetometer (MPMS *XL* by Quantum design) using several single crystals. There are two methods used for this measurement, such as with grease and non-grease. The grease method is using 0.22 mg samples mounted at the center of plastic straw with Apiezon N grease and the applied magnetic field is parallel to long axis or *c* direction of crystals. The non-grease method is using 1.1 mg of samples and polyacetal rod as the sample holder (appendix AP.2). The samples were inserted to the center of the rod, and the applied field is perpendicular to the *c* direction of crystals.

The ESR measurements performed by a conventional X-band ESR spectrometer (JEOL JES-RE3X) with magnetic range 319 – 326 mT equipped with a He-flow cryostat (Oxford Instruments). There are two single crystals used for ESR measurement with crystal dimensions is $0.1 \times 0.15 \times 2$ mm for sample 1 and $0.05 \times 0.05 \times 1.3$ mm for sample 2 as shown in the Fig. 5.1. The sample was mounted on a quartz rod using a silicone grease (appendix AP.3). Both samples for temperature dependence and angular dependence of applied magnetics field direction. The angular dependence measured by ESR was performed by rotating the quartz rod relative to the crystal plane: *ab*, *ac*, and *bc* plane at temperature of choices. The temperature dependence measurement was performed on the principal axis of *g*-values, which were relatively close to the directions of crystal axis. A single crystal was cooled with zero field cooling (ZFC) process and measurements were started from the lowest temperature while applying magnetic field to the sample.

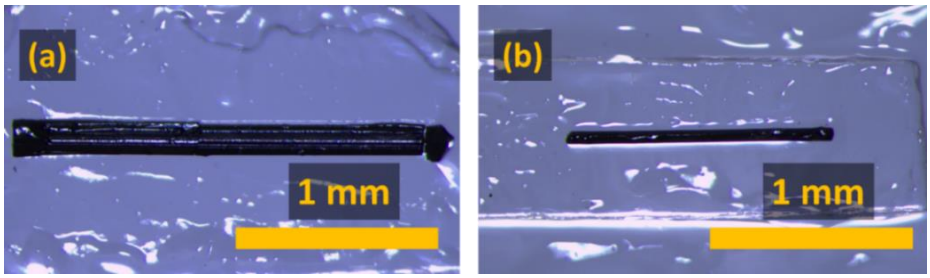

Fig. 5. 1 Two single crystals used for ESR spectroscopy measurement. (a) sample 1 and (b) sample 2. The pictures are taken after measurement.

5.2 DC magnetization

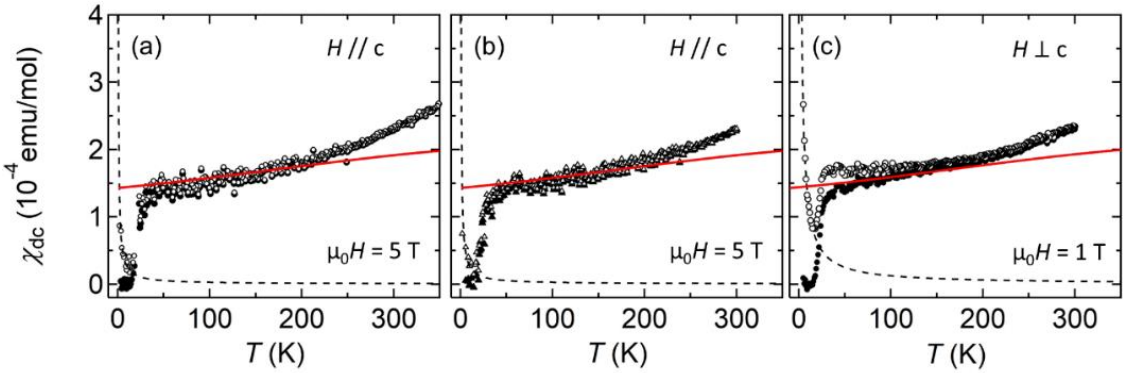

Fig. 5. 2 Magnetic susceptibility χ_{dc} from dc magnetization measurements. Sample 1: (a) hollow circle corresponds to cooling condition with 5 T magnetic field parallel to *c* direction and (b) hollow triangle corresponds to heating condition with 5 T magnetic field parallel to *c* direction. Sample 2: (c) hollow circle corresponds to cooling condition with 1 T magnetic field perpendicular to *c* direction. All results of χ_{dc} are corrected with Diamagnetic component χ'_{D}. Filled circle and triangle correspond to cooling and heating condition of χ_{dc} after subtracting χ_{C}. The dashed line corresponds to Curie law χ_{C}. The red line corresponds to fitting function based on Bonner-Fisher for spin 1/2 Heisenberg chain with antiferromagnetic coupling [45,73].

The temperature dependence of the static susceptibility χ_{dc} measured by dc magnetization measurement with two different applied magnetics flied direction which parallel and perpendicular to *c* direction are plotted in the Fig. 5.2. The measured data was obtained after subtracting background magnetization from the sample holder and the results corrected with the Diamagnetic χ'_{D} obtained from pascal constants about -3.6×10^{-4} emu. mol^{-1} [49,68]. In sample 1, there is no magnetic hysteresis in magnetic susceptibility χ_{dc} between cooling and heating condition as shown in Fig. 5.2 (a) and (b). The magnetic susceptibility χ_{dc} of sample 2 in Fig. 5.2 (c) has similar tendency with sample 1. These results indicate that there is no magnetic field value and direction dependences in the sample 1 and 2 as shown by similar magnetic behavior. From higher temperatures, the susceptibility χ_{dc} is gradually decreased with decreasing temperature down to 30 K. This gradually decreases can be explain by short-range ordering behavior appear after of broad peak in the χ_{dc} which is attributed to low-dimensional localized spin systems. This broad peak in the χ_{dc} is estimated will appear above 350 K. A sudden decrease of the χ_{dc} has been observed around $T_{\mathrm{sp}} \approx 26$ K. The sudden decrease on the magnetic susceptibility χ_{dc} might be attributed to spin-singlet-like transition. Curie-like behavior was observed at low temperature with χ_{dc} start to increase again at about 15 K. The Curie contribution χ_{C} was fitted by Curie law with parameters $\mathrm{C}_1 = 0.268 \times 10^{-3}$ and $\mathrm{C}_2 = 1.25 \times 10^{-3}$ emu. K. mol^{-1} from sample 1 and 2 respectively. The Curie constant C might be related with impurity spin in the sample, and it can be calculated with eq. 5.1 [50]:

$$C = \frac{N\mu_{eff}^2\mu_B^2}{3k_B} \tag{5.1}$$

where N is number of magnetic atoms per volume, μ_{eff} is effective magnetic moment which set equal to 1, μ_B is Bohr magneton and k_B is Boltzmann constant. The impurity spin in the sample can be get

from the ratio of *N* in the eq. 5.1 with volume of sample (where total of molecule in unit cell is about z = 4), and the amount of impurity is 0.2 % and 1.1% from sample 1 and 2 respectively.

High temperatures of χ_{dc} can be fitted with Bonner-Fisher model to estimated exchange coupling *J* in the (BEDT-TTF)Cu[N(CN)$_2$]$_2$. Bonner-Fisher (BF) model is well-known for studying the behavior of spin 1/2 Heisenberg chain with antiferromagnetic (AF) coupling, which is resembling with 1D chain and alternating chain [45,69,70]. In the previous study, a numerical model was used to fit the BF model for 1D linear chain and alternating chain using eq. 5.2 [70, 71],

$$\chi(T) = \frac{Ng^2\mu_B^2}{k_B T}\frac{A+Bx+Cx^2}{1+Dx+Ex^2+Fx^3} \tag{5.2}$$

with $x = J/T$ and J in temperature unit. The measured data was fitted in between 100 – 300 K. The coefficients were given for linear chain are A = 0.25, B = 0.14995, C = 0.30094, D = 1.9862, E = 0.68854, and F = 6.0626 and the coefficients for alternating chain are A = 0.25, B = 0.1242, C = 0.049, D = 1.362, E = 2.292, and F = 1.317, where the value of $\gamma = 0.99$ is based on alternating chain model [71, 72]. The exchange coupling J of susceptibility χ_{dc} from eq. 5.2 with two different set of coefficients are about 450 K. There is deviation of χ_{dc} with BF model fitting function in the high temperature regions as shown in Fig. 5.2. The exchange coupling *J* can also be calculated from 1D Hubbard model $2J = 4t^2/U$ of energy gap between singlet and triplet state, where *U* is coulomb site potential and *t* is transfer integral. The exchange coupling from this model given value $J \sim 650$ K where the transfer integral *t* is about −0.193 eV and the coulomb site potential of BEDT-TTF molecule about 0.7 eV from the chapter 3 and 4 respectively. Although order of from exchange coupling from both model is same, the fitting result is not match with 1D Hubbard model which might be due to calculation is not incorporating transfer integral *t'*. In addition, deviation of χ_{dc} with BF model might be due to itinerant electron come from a semimetal state of this organic compound which already explain by band structure and electronic properties in the chapter 3 and 4, respectively. When (BEDT-TTF)Cu[N(CN)$_2$]$_2$ in the Mott insulating state, the χ_{dc} nicely fit with BF model which mean there is localization of electrons in molecule site of BEDT-TTF.

The spin-singlet-like transition that is observed around $T_{\mathrm{sp}} \approx 26$ K, which is the sudden decrease of the susceptibility χ_{dc}, become the main interest for understanding magnetic properties in (BEDT-TTF)Cu[N(CN)$_2$]$_2$. Measurement of dc magnetization is bulk susceptibility which could not distinguish between its intrinsic and extrinsic components in magnetic susceptibility.

5.3 ESR spectroscopy

ESR spectroscopy is best measurement to detect direct magnetic excitation spectrum of conduction electrons which can separate each contribution in magnetic properties of single crystal. The ESR spectroscopy can be used to confirm this spin-singlet-like transition that observed from dc magnetization measurement. Before confirming spin-singlet-like transition in the susceptibility χ_{dc} of (BEDT-TTF)Cu[N(CN)$_2$]$_2$, it is important to make sure that ESR apparatus detected π-electrons of

BEDT-TTF molecule which the main contribution to the magnetic properties. The room temperature angular dependence measurement was used to determine the principal axis π-electrons of BEDT-TTF molecule according to applied magnetic field directions to the single crystal. After that, temperature dependence measurement will be conducted along principal axis direction, and parameter from the ESR spectra will be used to analyzed magnetic properties of (BEDT-TTF)Cu[N(CN)$_2$]$_2$.

5.3.1 Principal axis from angular dependence

Fig. 5.3 shows angular dependence results at room temperature with three different crystal planes such as *ab*, *ac*, and *bc* plane. The value *g*-value of angular dependence can be obtained from the magnetic field resonance H_0 of ESR spectrum:

$$g = \frac{hv}{\mu_B \mu_0 H_0} \tag{5.3}$$

where *v* is applied microwave frequency from ESR machine setup, *h* is Planck's constant, μ_B is Bohr magneton, and μ_0 is vacuum permeability. The principal axis direction can be simply got from maxima and minima value of *g*-value of angular dependence. This principal axis direction such as $g_{\max}$, g_{mid}, and $g_{\min}$ will be used as fixed direction for temperature dependence measurement later. The given value of maxima and minima in Fig. 5.3; 2.0145 and 2.0038 from *ab* plane, 2.0131 and 2.0069 from *ac* plane, and 2.0087 and 2.0048 from *bc* plane. The maxima and minima values in each crystal plane

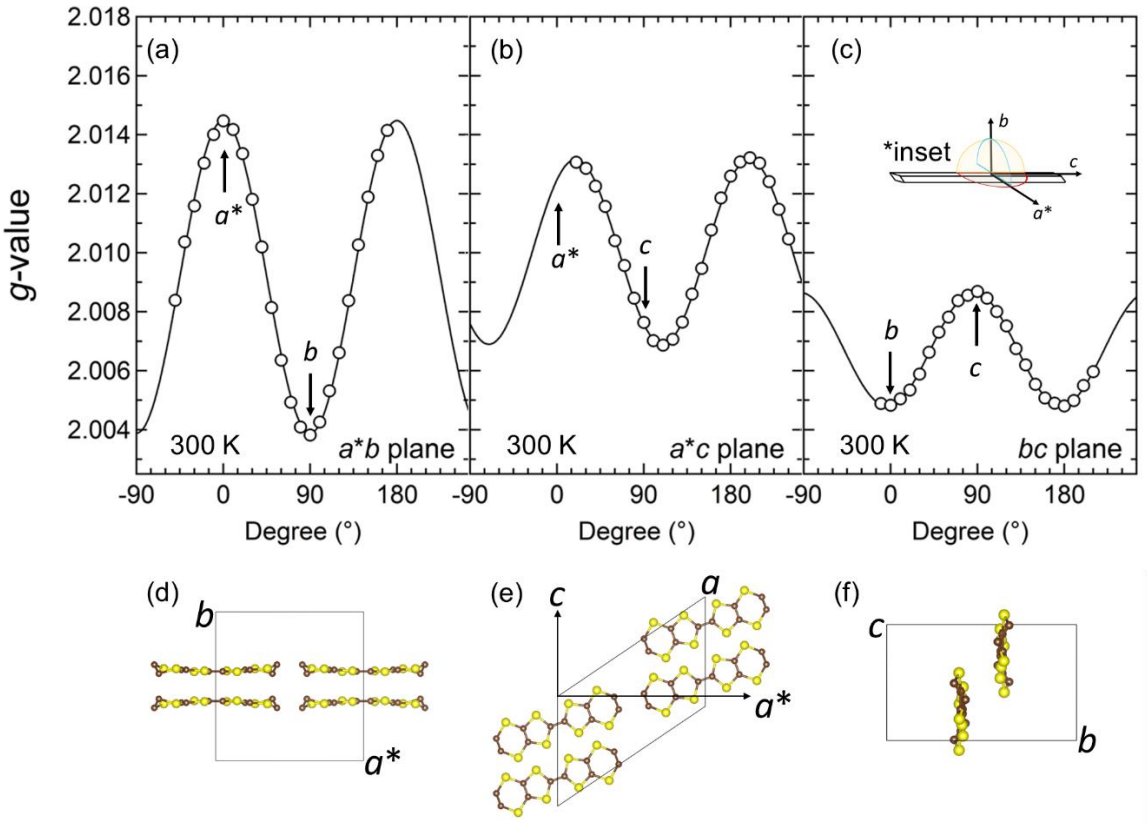

Fig. 5. 3 Angular dependence of *g*-value at 300 K. (a) and (d) *a***b* plane in *c*-axis rotation with *a** = 0°, (b) and (e) *a***c* plane in *b*-axis rotation with *a** = 0°, and (c) and (f) *bc* plane in *a*-axis rotation with *b* = 0°. Circle represents *g*-value from resonance fields H_0 from measured data. Black line represents fitting function of eq. 5.5 fitted to the measured data. Inset figure morphology of needle-like single crystal corresponds to crystal axis directions.

are different from each other which makes it difficult to determine the true values of $g_{\max}$, g_{mid}, and $g_{\min}$. The differences in maxima and minima value due to the single crystal placement is misaligned resulting less value of the principal axis. To get more accurate detail, the *g*-value of angular dependence can be fitted with rotational matrix following equation below [73,75],

$$g^2 = \sum_{i,j} G_{ij} l_i l_j \qquad (5.4.a)$$

$$G_{ij} = \sum_{i,j} g_{ik} g_{kj} \qquad (5.4.b)$$

$$g^2 = (g^2)_{ii} \cos^2 \theta_k + (g^2)_{jj} \sin^2 \theta_k + 2(g^2)_{ij} \cos \theta_k \sin \theta_k \qquad (5.5)$$

where *i* and *j* are measured plane and *k* is the crystal axis rotation in the magnetic field, g^2 is the principal axis based on a set of orthogonal axes or in this case crystal morphology direction such as *a**, *b*, and *c* as shown in the inset Fig. 5.3. The *a** direction is given direction that perpendicular to the other crystal morphology directions in each crystal plane. The fitting result will give a 3×3 matrix of principle axis and the principal axis value can be obtained from square root of eigenvalues *g*-tensor ($g_{\max}$, g_{mid}, and $g_{\min}$). When the crystal placement is not misaligned, the 3×3 matrix of principle axis will be become matrix identity. The principal values of *g*-tensor from fitting results were $g_{\max}$ = 2.0144 (0.99, 0.0, -0.097), $g_{\min}$ = 2.0039 (0.0, 1.0, -0.089), and g_{mid} = 2.0086 (0.10, 0.089, 1.0). These results show that the single crystal is tilting around *ac* and *bc* plane.

The results from Fig. 5.3 also indicating $g_{\max}$, $g_{\min}$ and g_{mid} is following BEDT-TTF molecule axis place in the unit cell. The *g*-value of angular dependence in Fig. 5.3 (a) and (c) show good agreement with crystal morphology directions in the *a***b* and *bc* plane, while *a***c* plane the *g*-value of angular dependence is shifting about 20° from *a** and *c* direction. These shifting of *g*-value because of ESR measuring long axis and short axis BEDT-TTF molecule which tilting about 20° in the real *ac* plane of unit cell. The value of principal axis direction can be compared to the other BEDT-TTF based organic compounds. From the previous studies of β-(BEDT-TTF)$_2$I$_3$ and IBr$_2$, Sugano *et. al.* has determined the principal axis of BEDT-TTF cation radical using precise ESR study. According to them, $g_{\max}$ is along the long axis of the molecule, $g_{\min}$ is perpendicular to the molecule and g_{mid} along the short axis of the molecule [74, 75]. The other study for κ-(BEDT-TTF)$_2$*X* also used a similar principal axis assignment. The small *g*-shift between $g_{\min}$ with free electron g_{e} = 2.002319 is about 0.0088, which explains that a p_{z} orbital of C and S atom from highest occupation molecular orbital (HOMO) and lowest occupation molecular orbital (LUMO) of the BEDT-TTF molecule [75]. For the other principal axis, anisotropy arise from spin-orbit coupling of conduction electron in the BEDT-TTF molecule. Therefore, the arrangement of principal axis can be deduced from the molecular symmetry [76]. The current results are in a good agreement with the previous study about principal axis of BEDT-TTF cation radical. This mean the ESR spectroscopy is directly detected π-orbital of the BEDT-TTF molecule in the current sample.

5.3.2 Temperature dependence of ESR spectra

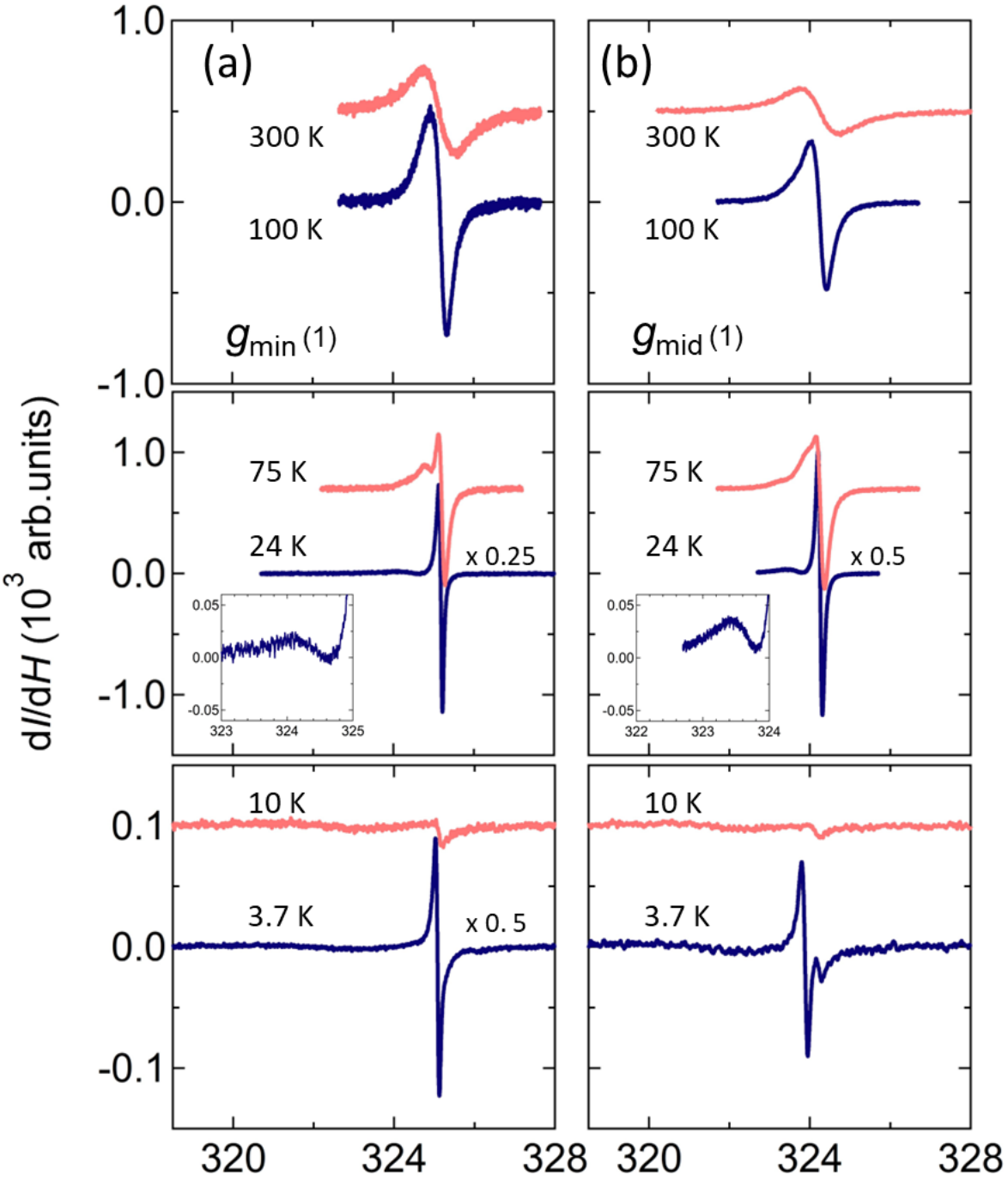

Fig. 5. 4 ESR spectra of chosen temperature from temperature dependence results at principal axis (a) g_{min} and (b) g_{mid} of sample 1 from 3.7 - 300 K. The ESR spectrum at 24 K from g_{min} and g_{mid}, and 3.7 K from g_{min} is adjusting with values as shown in the figures to get better viewing. Inset Fig enlargement of 24 K spectrum (a) g_{min} and (b) g_{mid} for better viewing.

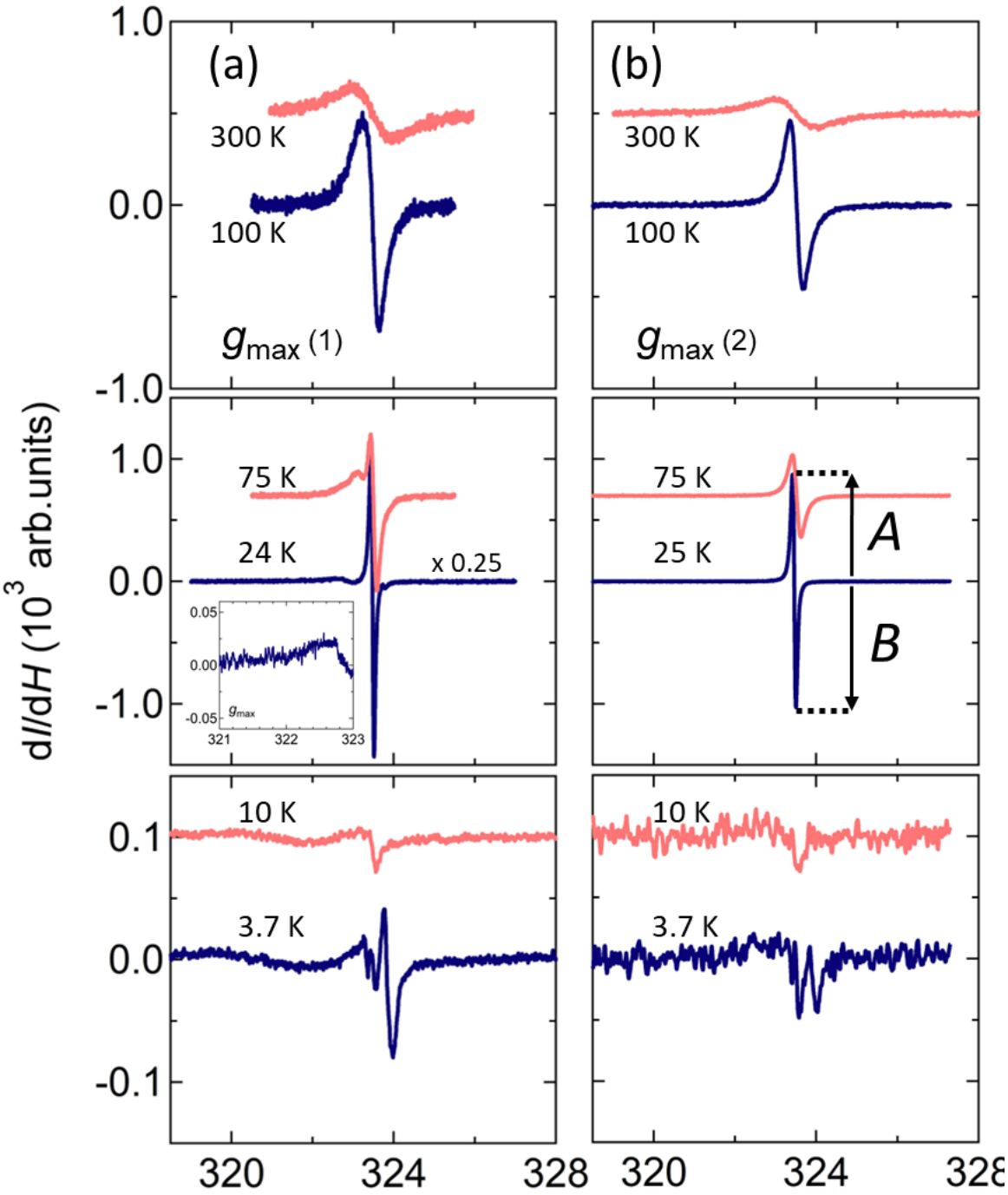

Fig. 5. 5 ESR spectra of chosen temperature from temperature dependence results at principal axis (a) $g_{\max}$ of the sample 1 and (b) $g_{\max}$ of sample 2 from 3.7 - 300 K. The ESR spectrum at 24 K from $g_{\max}$ from sample 1 is adjusting with values as shown in the figures to get better viewing. Inset Fig enlargement of 24 K spectrum (a) $g_{\max}$. A and B are in the ESR spectrum 25 K sample 2 represent top peak and bottom trough respectively for all principal axis directions.

Temperature dependence of ESR spectroscopy measurement was conducted along the principal axis direction of g-value. The result will be presented as arbitrary units because the measurements do not use reference material. All ESR spectra will be normalized by ESR machine parameters. Fig. 5.4 and Fig. 5.5 show all ESR spectra from sample 1 and sample 2 at the principal axis directions. At 300 K, ESR spectrum exhibits symmetrical line shape, which has similar values for peaks on top and bottom of spectrum. At 100 K, ESR spectra of sample 1 start to become unusual, while in sample 2 the ESR spectrum still in symmetrical line shape.

The ESR spectra of sample 1 at all principal axis direction below 75 K start to split to into two peaks namely additional peak and main spectrum as shown in the middle part of Fig. 5.4 and Fig. 5.5. The main spectrum become asymmetric with the bottom trough become more longer than top peak. The ESR spectrum of sample 2 does not have any additional peak as in sample 1, but it has asymmetric features as well as sample 1. The additional peak at sample 1 start to completely split from the top peak of ESR spectrum around 24 K, but the bottom trough of spectrum still convoluted with the main spectrum of ESR. This additional peak still does not exist in sample 2 around 25 K. The additional peak at sample 1 become rather smaller than the main ESR spectrum of sample 1 as temperatures decreasing. Both samples are share similar features on the spectrum, namely asymmetric features. The ESR spectrum become narrower at 25 K compared to higher temperature for both samples and the asymmetric features for both samples become more prominence. The narrowing of ESR spectrum at 25 K is relate with spin-singlet-like transition $T_{sp} \approx 26$ K in the dc magnetic susceptibly χ_{dc}. Additionally, the top peak of ESR spectrum will be labeled as peak A and the bottom trough will be labeled as peak B as shown in Fig. 5.5 (b). Below 25 K, the intensity of ESR spectra for both samples are decreases as temperatures decreasing.

At 10 K, all ESR spectra from both samples become almost flat and become weak in all principal axis directions. In addition, the additional peak on the ESR spectra of sample 1 in all principal axis directions still exist with subtle appearance. The unusual spectra start appearing below 10 K with the strongest appearance at 3.7 K for both samples. At 3.7 K, the ESR spectrum at $g_{\min}$ has two signals such as the main spectrum with strongest asymmetric features compare to the other direction, and weak additional peak. The ESR spectrum at g_{mid} has three signals with the main spectrum in the asymmetric condition, and two additional peaks before and after the main spectrum which the additional peak before the main spectrum is same peak that start to appear below 75 K. The ESR spectrum $g_{\max}$ for both samples have similar features to each other such as three signals with two additional peaks before the main spectrum, but sample 2 shows weakest main spectrum compared to sample 1. Later the $g_{\max}$ for sample 1 and 2 will be named as $g_{\max}(1)$ and $g_{\max}(2)$, respectively.

5.3.3 Asymmetric feature and fitting procedure

The appearance of asymmetric features from both samples ESR spectra become one of the main interests to understanding the ESR spectra temperature dependences. To understand this asymmetric

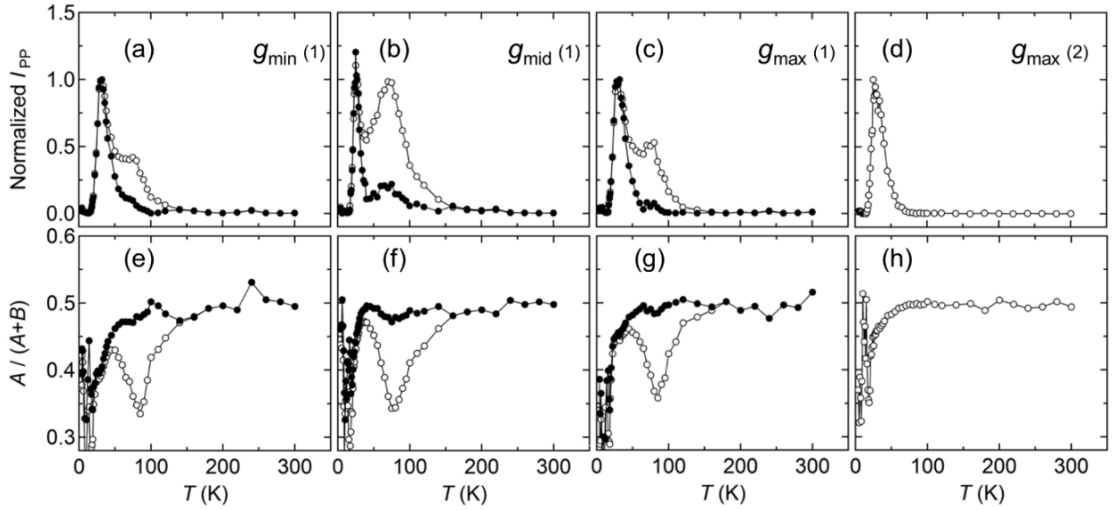

Fig. 5. 6 Normalized peak-to-peak intensity I_{pp} from both samples along all principal axis direction: (a) g_{min}, (b) g_{mid}, (c) $g_{\mathrm{max}}(1)$, and (d) $g_{\mathrm{max}}(2)$. Ratio $\mathrm{A}/(\mathrm{A}+\mathrm{B})$ (peak A and bottom trough B in inset 4.5): (e) g_{min}, (f) g_{mid}, (g) $g_{\mathrm{max}}(1)$, and (h) $g_{\mathrm{max}}(2)$ where 0.5 equal to symmetric line. Hollow circle corresponds to measured data and filled circle is after removing additional peak from the main spectrum for both Normalized intensity I_{pp} and ratio $\mathrm{A}/(\mathrm{A}+\mathrm{B})$.

feature, the ESR spectrum will be checked with peak-to-peak intensity I_{pp} from peak A and bottom trough B as explain in the previous section, and the value will be normalized with the highest intensity value. The ratio between peak A and $(\mathrm{A}+\mathrm{B})$, labeled as $\mathrm{A}/(\mathrm{A}+\mathrm{B})$ (0.5 = symmetric) is plotted in Fig. 5.6. This analysis will be combined with fitting procedure on ESR spectrum as shown in Fig. 5.7 and Fig. 5.8. ESR spectrum will be fitted with the first derivative of Lorentzian and the parameter of ESR spectrum line shape such as peak-to-peak intensity (I_{pp}), linewidth (ΔH_{PP}), and g-value from magnetic field resonance H_0 can be obtained by:

$$\frac{dI}{dH} = L' = \frac{16 I_{PP}(H-H_0)/(\Delta H_{PP}/2)}{\left[3+\{(H-H_0)/(\Delta H_{PP}/2)^2\}\right]^2} \tag{5.6}$$

and the integrated intensity ESR spectrum is equal to $\left(2\pi/\sqrt{3}\right) I_{\mathrm{pp}} \Delta H_{\mathrm{PP}}^2$ [77]. There are three components Lorentzian function such as component labeled as *1**, *2**, and *3**, where component *1** and *2** coming from main spectrum and component *3** come from additional peak for sample 1 that start appearing below 75 K and additional peak for sample 1 that start appearing below 10 K as shown as shown in Fig. 5.7 (b) and Fig. 5.7 (c), respectively. The normalized intensity I_{pp} from Fig. 5.6 increased with decreasing temperatures. The hollow circle graphs in Fig. 5.6 (a), (b), and (c) represent intensity I_{pp} from measured data showing that there are two peaks around 25 K and 75 K on sample 1, and only one peak around 25 K on sample 2 as shown in Fig. 5.6 (d). The first peak around 25 K is coming from the main ESR spectrum, and the second peak around 75 K is coming from peak *3**. The normalized intensity I_{pp} at g_{mid} direction shows the strongest peak compared to the other principal axis direction. The ratio of $\mathrm{A}/(\mathrm{A}+\mathrm{B})$ from sample 1 at all principal axis direction is drastically decreasing below 160 K to 75 K, and the ratio start increasing from 75 K and decreasing again at below 45 K. While in the sample 2 the ratio of $\mathrm{A}/(\mathrm{A}+\mathrm{B})$ start decreased below 75 K.

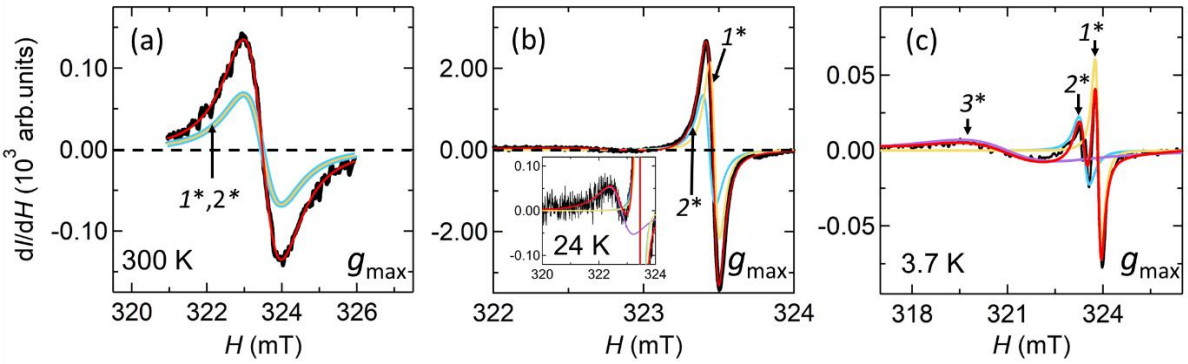

Fig. 5. 7 ESR spectrum of sample 1 along g_{max} direction: (a) 300 K, (b) 24 K, and (c) 3.7 K. The yellow, blue, and purple line represent component *1**, *2**, and *3** of Lorentzian function respectively, and the red line represents total fitting. Inset figures in (b) the additional peak *3** in the sample 1 which appear at all principal axis directions below 75 K.

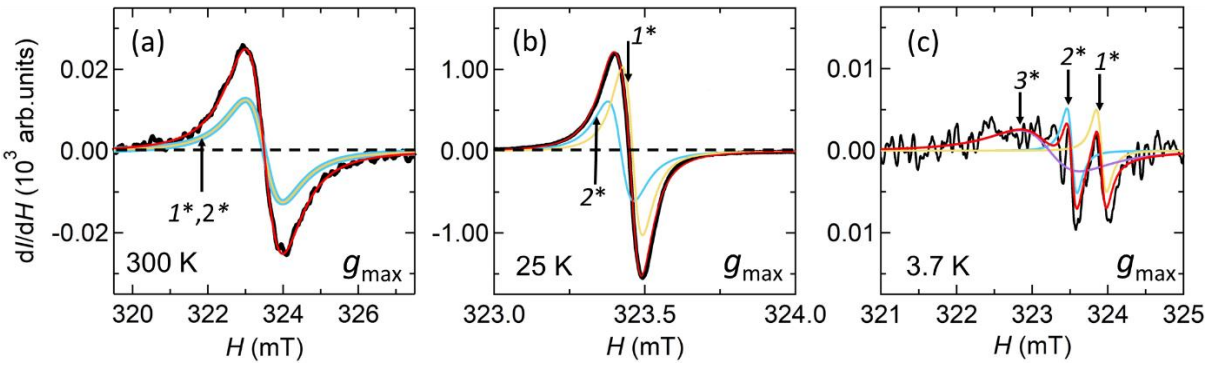

Fig. 5. 8 ESR spectrum of sample 2 along g_{max} direction: (a) 300 K, (b) 24 K, and (c) 3.7 K. The yellow, blue, and purple line represent component *1**, *2**, and *3** of Lorentzian function respectively, and the red line represents total fitting.

By using eq. 5.6, the additional peak 3* can be removed to check whether asymmetric features are intrinsic behavior from the single crystal of the samples or due to the appearance of an additional peak of peak *3**. The second peak around 75 K from normalized intensity I_{pp} disappeared after removing peak *3** from ESR spectrum, and the first peak for both samples show similar behavior to each principal axis direction as shown by filled circle graphs in Fig. 5.6. The ratio of $\mathrm{A}/(\mathrm{A}+\mathrm{B})$ also shows similar results with the normalized intensity where all principal axis directions now have similar asymmetric starting temperature below 75 K. There is a slight difference in asymmetric temperature starting point at g_{mid} in the measured data which might be due to the ESR spectrum line shape heavily affected by peak *3**. From this analysis, the ESR main spectrum becomes asymmetric is not because of the appearance of additional peak *3** at higher temperature, but rather intrinsic features from the single crystal of (BEDT-TTF)Cu[N(CN)$_2$]$_2$. For the peak *3** is still debatable whether component can be observed in the higher temperature regions or not. The appearance of peak *3** at higher temperature might be due to crack in the middle single crystal as shown in Fig. 4. 1 (a). However, in the sample 2, peak *3** in low temperature might has better clarity to identify the origin of this component because there is no crack in the single crystal as shown in Fig. 4. 1 (b).

To get better understanding of ESR spectrum, Lorentzian fitting procedure can be proceeded after confirming asymmetric features in the ESR spectrum is intrinsic from the main spectrum. The

ESR main spectrum at low temperature regions will consist of two Lorentzian components *1** and *2** for sample 1 and sample 2 to form asymmetric ESR spectrum. In sample 2, the component *3** start appearing below 10 K, while in sample 2 component *3** already exist in high temperature regions. Therefore, there are several assumptions for fitting procedure for both samples from low temperature regions to high temperature regions.

First assumption is the asymmetric feature due to convolution of two components *1** and *2** for both samples. The ESR spectrum has symmetric feature at 300 K for both samples. This symmetric feature can be defined as one Lorentzian component, and it also can be defined with more than one Lorentzian component. Therefore, to get better data continuity, the symmetric ESR spectrum will be fitted with two components *1** and *2**. The two-component assumption for symmetrical and symmetrical ESR spectra is also consistent with the fact that there is z = 4 BEDT-TTF molecules in crystal structure or z = 2 for primitive unit cell at 300 K as explained in chapter 3. This mean that the two components *1** and *2** should be coming from the same localized resonance source i.e., BEDT-TTF molecule site which compose the ESR main spectrum.

The second assumption is because of component *1** and *2** come from same magnetic resonance of BEDT-TTF molecules, the spin density of ESR parameter should be equal for both components *1** and *2**. This means that the integrated intensity of both components is equal, which also helps avoiding artifact result in the spin susceptibility.

The third assumption for the component *3** that is appear in high temperature regions for sample 1 and low temperature regions for sample 2. The component *3** source is unknown because its intensity is weak at high temperature regions in the sample 1. For the sample 2, the ESR main spectrum asymmetric feature was not influenced by component *3** at high temperature regions, however it has similar asymmetric feature with sample 1 after subtracting component *3** from the ESR main spectrum as shown in Fig. 5.8. Therefore, for the third assumption, component *3** will start appearing at around 160 K and will disappear at high temperature regions for sample 1, which suitable with analysis of normalized intensity I_{pp} in the Fig. 5.8. For the sample 2, the component *3** will start appearing below 10 K because of the ESR spectrum has complex spectral line shape after at below this temperature regions.

From all the assumptions, it can conclude that the sample 2 is more representative rather than sample 1 because of the ESR main spectrum has simplified component from higher temperature to the temperature of spin-singlet-like transition T_{sp} from the dc magnetic susceptibly χ_{dc}. Therefore, sample 2 will be become main deciding factor for ESR spectrum analysis. The fitting function for ESR spectrum would be the total of all Lorentzian components:

$$L'_{tot} = \sum_{i=1}^{n} L'_n. \tag{5.7}$$

5.3.4 ESR spectra parameters

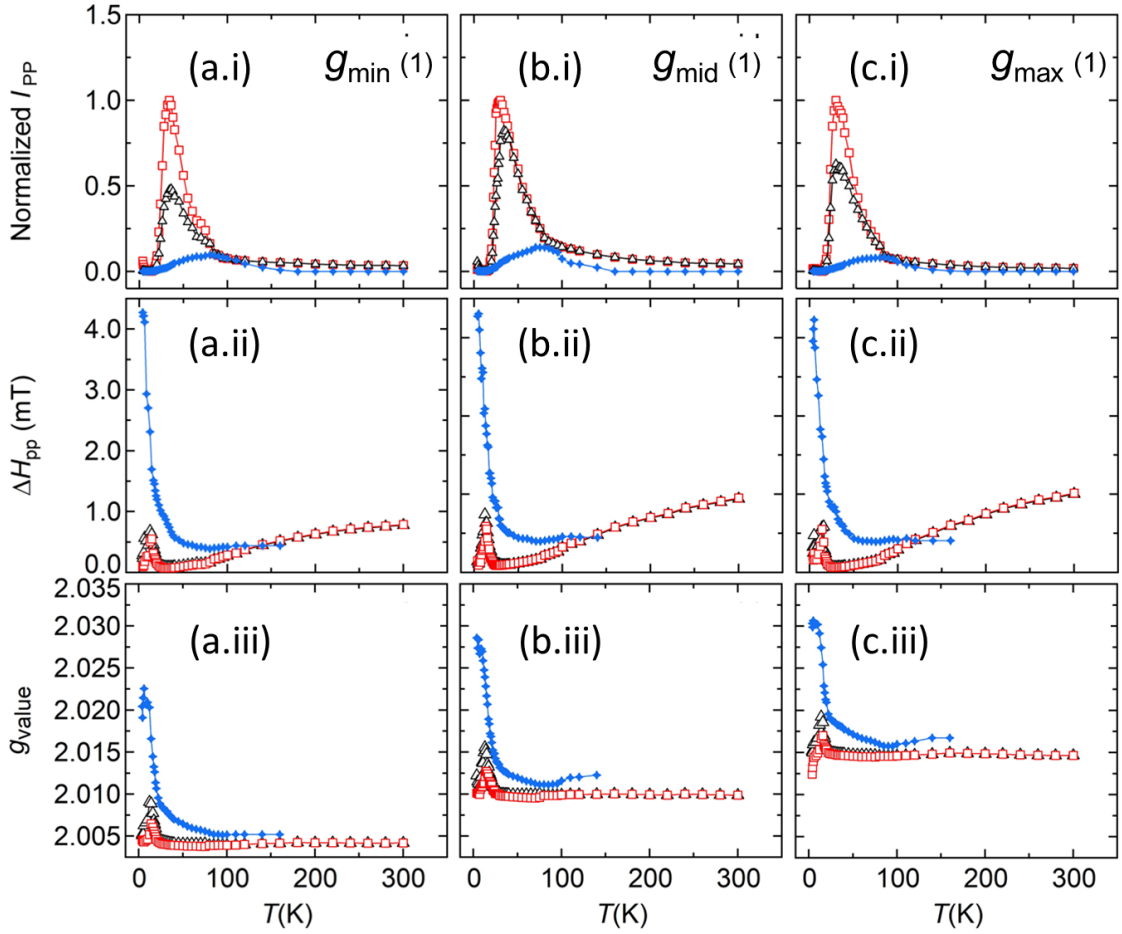

Fig. 5. 9 ESR parameters of sample 1 from fitting results eq. 5.7. (a) $g_{\min}(1)$, (b) $g_{\mathrm{mid}}(1)$, and (c) $g_{\max}(1)$. There are three parameters in each column figure from top to bottom: (i) Normalized intensity I_{pp}, (ii) linewidth ΔH_{PP}, and (iii) g-value. Square, triangle, and filled star graphs correspond to component *1**, *2** and *3** respectively

Fig. 5.9 and Fig. 5.10 show ESR parameter for sample 1 and 2 at all principal axis direction. All ESR parameters for both samples have similar behavior in each parameter at all principal axis direction. The parameters of ESR component *1** and *2** will be remain same until asymmetrical features begin to appear. The normalized intensity I_{pp} from fitting results are match with real intensity I_{pp} measured data. The normalized intensity I_{pp} is increased with decreasing temperature. For sample 1, the intensity I_{pp} has three components with component *1** has strongest peak intensity around 30 K compared to other components, and component *3** has broader features compared to other components. This behavior of intensity I_{pp} of component *1** and *2** in the sample 1 confirm by sample 2 where intensity of *2** a quarter less than *1**. The increased intensity I_{pp} around 30 K are related with spin-singlet-like transition at $T_{\mathrm{sp}} \approx 26$ K in the χ_{dc}. The intensity I_{pp} decreasing rapidly below 25 K down to 10 K. The low temperature regions of intensity I_{pp} will be represent by data from sample 2 because, as in the previous section, the appearance of component *3** in the low temperature regions is more convincing rather than in high temperature regions. Fig. 5.10 (b) shows intensity I_{pp} component *3** start

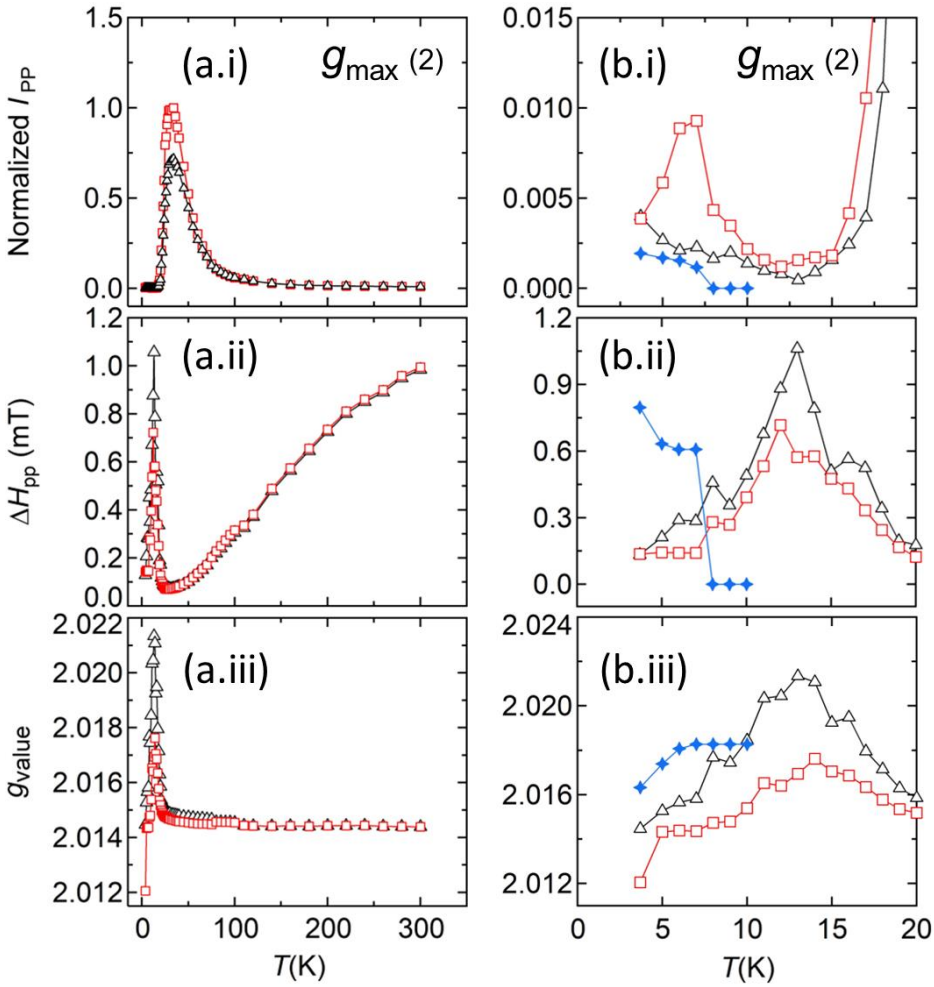

Fig. 5. 10 ESR parameters of sample 2 from fitting results eq. 5.7. (a) $g_{\max}(2)$ for all temperature regions and (b) $g_{\max}(2)$, for low temperature regions. There are three parameters in each column figure from top to bottom: (i) Normalized intensity I_{pp}, (ii) linewidth ΔH_{PP}, and (iii) g-value. Square, triangle, and filled star graphs correspond to component *1**, *2** and *3** respectively.

to increase below 10 K followed by rapid increase component *1** and well as *2**. This intensity I_{pp} behavior is also can be observed for other principal axis directions. At 3.7 K, the intensity I_{pp} of component *1** and *2** are like each other.

The increased intensity value of I_{pp} compensate by the narrowing linewidth as shown in Fig. 5.9 and Fig. 5.10. The parameter linewidth ΔH_{PP} at all principal axis direction is decreased with decreasing temperature and it has linear tendency from 300 K to 30 K. The linewidths ΔH_{PP} of sample 2 shows both components also have two different linear slopes at around 200 K. The results clearly show that the parameter of each principal axis has similar parameters with each other. In addition, the absolute value of ΔH_{PP} is nearly same between sample 1 and 2 at the g_{max} direction, as well as for other directions is similar too. This means the samples batch have good reproducibility data. The linewidth becomes narrower around 30 K which starts to increase with the maximum increase at 12 K and decreased again with decreasing temperature. The sudden drop in the linewidth ΔH_{PP} for both samples related to spin-relaxation time, which mean there is change in the magnetic state i.e., from triplet to

singlet state. Spin-relaxation time has two types such as spin-lattice relaxation T_1 due to energy exchange at emission process which can be shown by linewidth absorption ΔH_{PP}, and spin-spin relaxation T_2 caused by dipolar and exchange interactions between assembly of spins. The general relationship of T_2 and T_1 is $T_2 \leqq T_1$. Both of relaxation time effect can be expressed using eq. 5.8 and 5.9 and the combination of them can be expressed in eq. 5.10:

$$\Delta H_{\mathrm{PP}}(T_1) = \frac{h}{g\mu_B}\frac{1}{2T_1} = \frac{\pi}{\gamma T_1} \tag{5.8}$$

$$\Delta H_{\mathrm{PP}}(T_2) = \frac{h}{g\mu_B}\frac{1}{2T_1} = \frac{2\pi}{\gamma T_1} \tag{5.9}$$

$$\frac{1}{T_1} = \frac{1}{2T_1} + \frac{1}{T_2} \tag{5.10}$$

where g is g-value from the sample, μ_B is Bohr magneton, γ is gyromagnetic ratio. When the linewidth is getting narrow, spin-spin relaxation contribution can be ignored and the contribution came from spin-lattice relaxation. The spin-lattice relaxation occurs by releasing phonon which related to temperature, and the relation linewidth ΔH_{PP} with temperature T, $\Delta H_{\mathrm{PP}} \propto 1/T$ [42, 43]. For low temperature regions, the increasing of linewidth ΔH_{PP} at 12 K represent the ESR main spectrum become wider and almost disappeared, which also mean that the localized spin cannot be detected by ESR measurement, or the spin state in the system become complete spin-singlet state. This means that from the narrowest to the peak in linewidth ΔH_{PP} is a precursor condition for (BEDT-TTF)Cu[N(CN)$_2$]$_2$ to reaching spin-singlet state.

Fig. 5.9 and Fig. 5.10 show g-value for all components for both samples. The g-value for component *1** and *2** are remain constants from 300 K to around 80 K. The g-value components *1** and *2** split to into two different values below 80 K where components *1** has lowest value than *2**. Below 30 K, the g-value of both components *1** and *2** start to rapidly increase with maximum peak at 12 K. These peaks might have relation with the peak of linewidth ΔH_{PP} at 12 K where at this temperature the system become complete spin-singlet. The components *3** in sample 1 is increased with decreasing temperature at all principal axis direction where the order rank of g-value of components *3** has similar order of principal axis i.e., g_{min}, g_{mid} and g_{max}. The components *3** of sample 1 has the highest value compared to sample 2, while sample 2 has components *3** value close to the other components. It is very unclear why components *3** of sample 1 has very high value of g-value. This is probably because the broader shape of component *3** is a superposition of many signals from the cracks of single crystal as shown in Fig. 5.1 (a) resulting in different crystal plane directions. Therefore, from this possible explanation, the sample 2 provides a clearer origin of components *3**, as it might come from the same resonance source which is BEDT-TTF molecules as the g-value of components *3** of sample 2 is close to the other components.

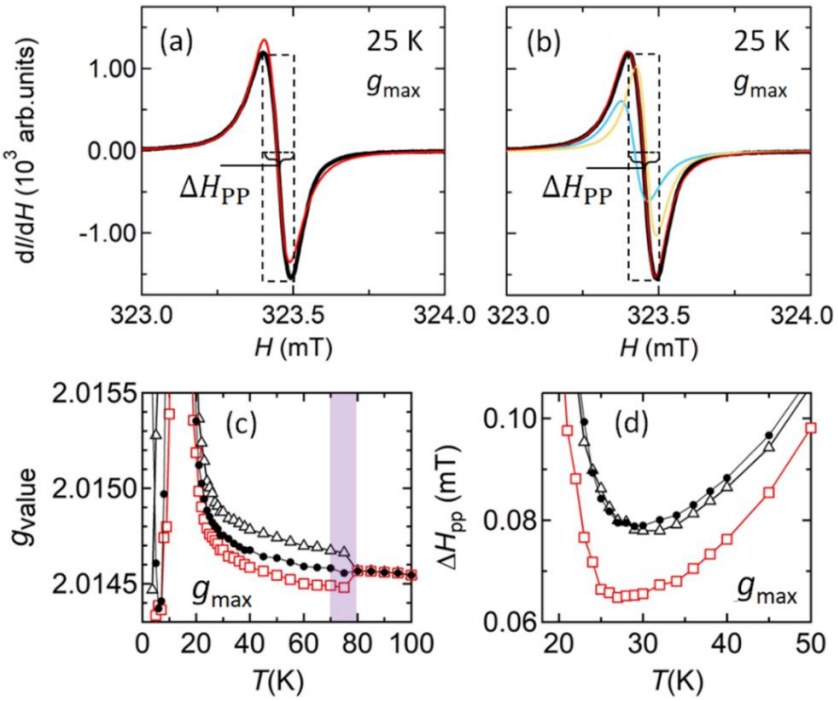

Fig. 5. 11 ESR spectrum of sample 2 along $g_{\max}(2)$ direction with different fitting procedure: (a) one Lorentzian component and (b) two Lorentzian components. The yellow, blue, and purple line represent component *1** and *2** of Lorentzian function respectively, and the red line represents total fitting. The dashed line corresponds to rectangles shape from peak-to-peak ESR spectrum ESR parameter from two different fitting procedure: (c) *g*-value and (d) linewidth ΔH_{PP}. Filled Circle corresponds to one component fitting labeled as *cr*. Square and triangle correspond to two components fitting *1** and *2**, respectively. There is a difficulty of fitting around the area in purple in the *g*-value results.

The information of the shift of *g*-value and the change of linewidth are important to get better understanding of relations between component *1** and *2** for the intrinsic properties of asymmetric feature in ESR spectrum. In this case, ESR parameters of sample 2 along $g_{\max}(2)$ because the results give more clarity of origin for component *1**, *2** and *3**. Fig. 5.11 (a) and (b) show comparison between one Lorentzian component fitting with two components Lorentzian fitting, and the result will be labeled as center (*cr*) for one component fitting and *1** and *2** for two components fitting. The ESR spectrum parameter can be understood as by making rectangular shape from peak-to-peak as shown in Fig. 5.11 (a) and (b), where this rectangle peak-to-peak intensity I_{pp} for long axis, peak-to-peak linewidth ΔH_{PP} for the short axis and magnetic field resonance H_0 for the center of rectangle. Fig. 5.11 (a) shows that one component fitting result has slight differences between intensity top peak and bottom trough B from fitting spectrum with long axis rectangle, which later these differences will be labeled as δI_{PP}. While for two components fitting shows no δI_{PP}, which mean nicely fit between intensity I_{pp} with long axis rectangle. However, there is a similarity between one component fitting and two components fitting, that is the linewidth, and the magnetic field resonance from both rectangles are the same. From this information, the shift of *g*-value and the change of linewidth can be obtained from difference between parameters from component *cr* and *i* (*i =1**, *2**) such as: $\Delta g = g_{\mathrm{cr}} - g_i$ and $\delta H = \Delta H_{\mathrm{PP(cr)}} - \Delta H_{\mathrm{PP(i)}}$, respectively.

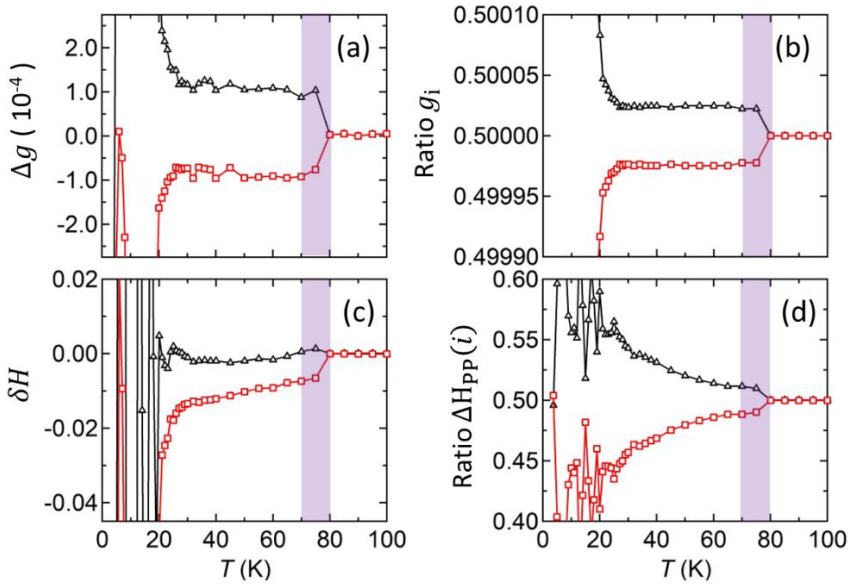

Fig. 5. 12 The change of *g*-value and linewidth from ESR parameters sample 2. (a) *g*-value shift Δg of component 1* and 2* from *cr*. (b) Ratio $g(i)/(\ g(1^*)+\ g(2^*))$ from the *g*-value of components *1** and *2**. (c) linewidth change δH of component 1* and 2* from *cr*. (b) Ratio $\Delta H_{PP}(i)/(\ \Delta H_{PP}(1^*)+\ \Delta H_{PP}(2^*))$ from the linewidth of components *1** and *2**. Square and triangle correspond to two components fitting *1** and *2**. There is a difficulty of fitting around the area in purple in the *g*-value results.

Fig. 5.12 shows shift of *g*-value Δg and the change of linewidth δH of component *1** and *2** from the component *cr*. The shift Δg of component *2** is shift to the higher value and component *1** is shift to the lower value as shown Fig. 5.12 (a). The shift Δg for both components from 100 K to 75 K should gradually change but the results show a jumping change in the values. The jumping change in the values is due to an artifact from the fitting procedure that required constraint which, at these temperature regions, hardly distinguishes component *1** and *2**. The *g*-values shifts are nearly constant below 75 K until the spin-singlet transition $T_{sp} \approx 26$ K, at which both values rapidly shift to the higher value and the lower value until 12 K for both component *1** and *2**, respectively. The differences of ratio of shift Δg are also nearly the same for components *1** and *2**, meaning both components undergo similar magnitude of change. The shift of *g*-values can be understood by using relation eq. 5.11 between *g*-value each component and *g*-value from free electron g_e,

$$g_{ij} = g_e - 2\zeta \sum_n \frac{\langle\psi_0|L_i|\psi_n\rangle\langle\psi_n|L_j|\psi_0\rangle}{E_n - E_0} \tag{5.11}$$

where ζ is spin orbit coupling constant and $\langle\psi_0|L_i|\psi_n\rangle$ is Matrix element angular momentum ground state ψ_0 with energy E_0 and excited state ψ_n with energy E_n [75]. By using this relation, component *2** has higher spin orbit coupling compared to component *1**. This means that component *2** is more likely to coupling toward component *1** at the spin-singlet transition T_{sp}.

Fig. 5.12 (c) shows the change linewidth δH of component *1** and *2** from the component *cr*. The change linewidth δH has different tendencies compared to *g*-value shift Δg, where δH of component *2** is nearly zero and δH of component *1** is getting narrow by decreasing temperature. In

addition, the differences of ratio of change δH are equal for components *1** and *2** as in shift Δg. This means that component *2** nearly same with symmetric ESR spectrum as represented by one component fitting. The component *1** shows a narrowing of linewidth which means that the spin relaxation is lower than component *2**, and this case spin relaxation come from spin-lattice relaxation. This results also might be indicated that there is symmetrical change in one of two BEDT-TTF molecules which represent by component *1** and *2**. The single-spin transition mechanism may be explained by combining shift Δg and change δ, which will be discussed later.

5.3.5 Spin susceptibility

The susceptibility χ_s can be defined from integrated intensity or ESR spectrum. Fig. 5.13 shows total integrated intensity or spin susceptibility χ_s of all Lorentzian component for principal axis direction. There is no significant difference behavior in the χ_s in all principal axis directions. The spin susceptibility χ_s is decreasing as temperature decreases and temperature of T_{sp} is also around 26 K, which has similar tendency with static susceptibility χ_{dc}. This feature of spin susceptibility χ_s mainly comes from components *1** and *2**, where both components have a similar integrated intensity as already explained in the fitting assumptions. Furthermore, both samples have components *1** and *2** show the singlet-like transition with almost $\chi_s = 0$ below 20 K, which indicates that components *1** and 2* do not have a Curie contribution at low temperatures as shown in Fig. 5.13 (d.II). On contrary, component *3** shows a large Curie-like contribution in χ_s is observed below 10 K in the sample 1. While in sample 2, the Curie-like contribution from component *3** is very small. This Curie contribution

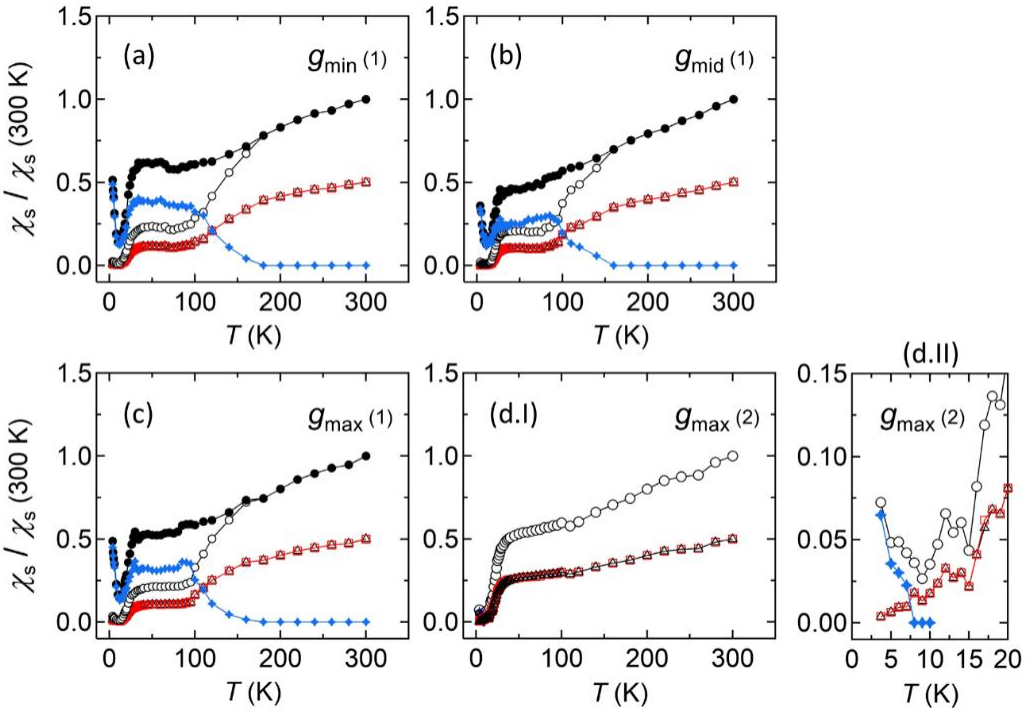

Fig. 5. 13 Total spin susceptibility χ_s from integrated intensity (a) g_{min}, (b) g_{mid}, (c) $g_{max}(2)$, and (dI) $g_{max}(2)$. Figure on side (dII) χ_s along $g_{max}(2)$ at low temperature regions. Square, triangle, and filled star graphs correspond component *1**, *2** and *3** respectively.

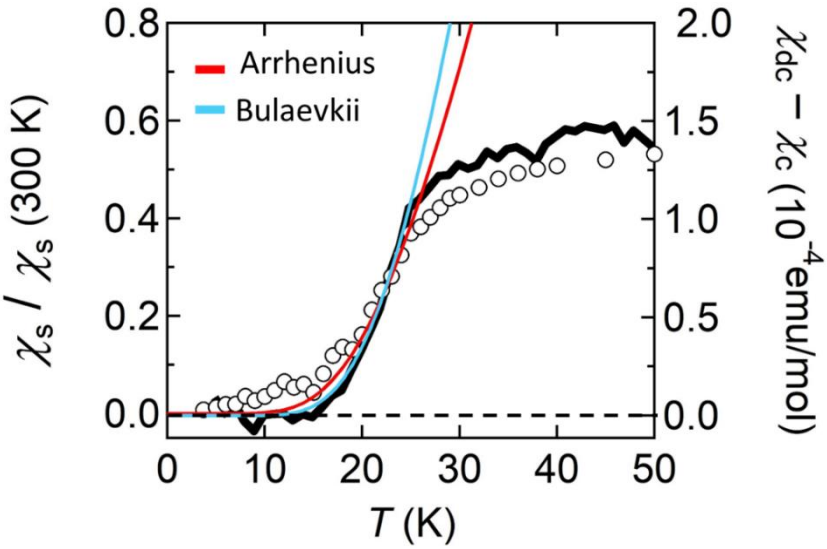

Fig. 5. 14 Circle represents total spin susceptibility χ_s components $(1^* + 2^*)$from $g_{max}(2)$ left axis. Black line represents static susceptibility χ_{dc} with right axis. Red line corresponds to fitting lines of Arrhenius law for $\chi_s(1^* + 2^*)$ and χ_{dc}. Blue line represents Bulaevskii model fitting lines for for $\chi_s(1^* + 2^*)$ and χ_{dc}.

is found at low temperature regions from broader linewidth of the component *3**. These observations indicate that components *1** and *2** are important to form a spin-singlet transition in this organic salt.

The results that isotropic spin-singlet states can be observed at all crystal structure direction. The effective spin Hamiltonian is defined by [44, 45],

$$H = -2J \sum_{i=1}^{N} \left[J_x S_i^x S_{i+1}^x + J_y S_i^y S_{i+1}^y + J_z S_i^z S_{i+1}^z \right] \tag{5.12}$$

The dimensionality of interaction defined by J_x, J_y, J_z component of exchange coupling energy tensor which the direction can be in any direction. Also, by assuming nearest-neighbor spin interaction only. When $J_x = J_y = 0$, and $J_z \neq 0$, the Ising model in the spin system is realized. When $J_x = J_y \neq 0$, and $J_z = 0$, the spin being free to any point at xy plane is realized. When $J_x = J_y \neq J_z$, this means the uniaxial magnetic anisotropy Heisenberg. The last, $J_x = J_y = J_z$ is isotropic Heisenberg model. In addition, because of 1-dimensional zig-zag chain structure of (BEDT-TTF)Cu[N(CN)$_2$]$_2$, the linear chain term can be included in the Hamiltonian. Therefore, the Hamiltonian for isotropic Heisenberg model in 1-dimensioanl system can be written in

$$H = -2J \sum_{i=1} \left[\hat{S}_{2i} \cdot \hat{S}_{2i-1} + \gamma \hat{S}_{2i} \cdot \hat{S}_{2i+1} \right] \tag{5.13}$$

where γ is the alternation parameter in the linear chain with value of γ in between $0 \leq \gamma \leq 1$. When $\gamma = 0$, the model become noninteracting spin pairs or dimers and when $\gamma = 1$, the model become regular linear chain [45]. From this explanation, by qualitatively, singlet transition of (BEDT-TTF)Cu[N(CN)$_2$]$_2$ can be observed at all crystal direction. The χ_s below 26 K shows isotropic spin-singlet state which indicates that exchange coupling *J* is symmetry in all direction which mean this result may fit to the 1D model spin 1/2 chain [44]. Because sample 2 has clear result of spin-singlet transition, the analysis of spin gap in χ_s for all principal axis direction will carried by sample 2 data.

A sudden decrease of χ_{dc} and χ_{s}below T_{sp} indicates a gap opening from triplet to singlet state. Arrhenius law is the simplest model for analyzing thermally activated behavior of single-triplet energy spin-gap Δ. Fig. 5.14 shows χ_{dc} and χ_{s} susceptibility of temperature dependence. By using relation $\chi \propto A\, exp(-\Delta/T)$, the parameters for susceptibility χ_{dc} are $A = 6.261 \times 10^{-3}$ emu. K. mol^{-1} with spin-gap $\Delta \approx 90$ K. For susceptibility χ_{S}, the parameter A is adjusted to χ_{dc} giving $A = 922$ arb. units with spin-gap $\Delta \approx 90$ K. Bulaevskii has reported model obtained for 1D AFM Heisenberg for alternated chain by using Hartree-Fock approximation with following as eq. 5.14,

$$\chi_{DC,S} = \frac{Ng^2\mu_B^2\alpha}{k_B T}\, exp\left(-\frac{\beta J_1}{T}\right) \tag{5.14}$$

where the value of α and β are parameters tabulated in the reported paper that depend on alternating parameter γ [78]. The parameter of alternation γ is related with two unequal and alternating exchange J_1 and J_2 produced from weakly dimerized in the chain, expressed by relation $\gamma = \left(1 - \frac{\delta}{1} + \delta a\right) = J_2/J_1$ [79]. The exchange coupling J for uniform spin chain above transition temperature can be expressed by relation $J_{1,2} = J(1 \pm \delta)$. By using eq. 5.14, the fitting parameters for susceptibility χ_{dc} are $J_1 = 186.9$ K and $J_2 = 95.3$ K with alternating parameter $\gamma = 0.51$ and $J = 141.1$ K. For susceptibility χ_{S}, the exchange coupling $J_1 = 188.0$ K and $J_2 = 95.9$ K with alternating parameter $\gamma = 0.51$ and $J = 141.9$ K. The relationship alternation parameter δ and spin-gap Δ is expressed as $\delta(T) = \Delta(T)/pJ$ with temperature dependent which can be described by mean-field theory and p is self-consistency condition equal to 1.637 [79,80]. Combine with Bulaevskii model that assumes δ is constant, the spin-gap for susceptibility χ_{dc} and susceptibility χ_{S} $\Delta(0) \approx 80$ K. The spin-gap energies Δ are consistent in both models.

5.3.6 Angular dependence of linewidth

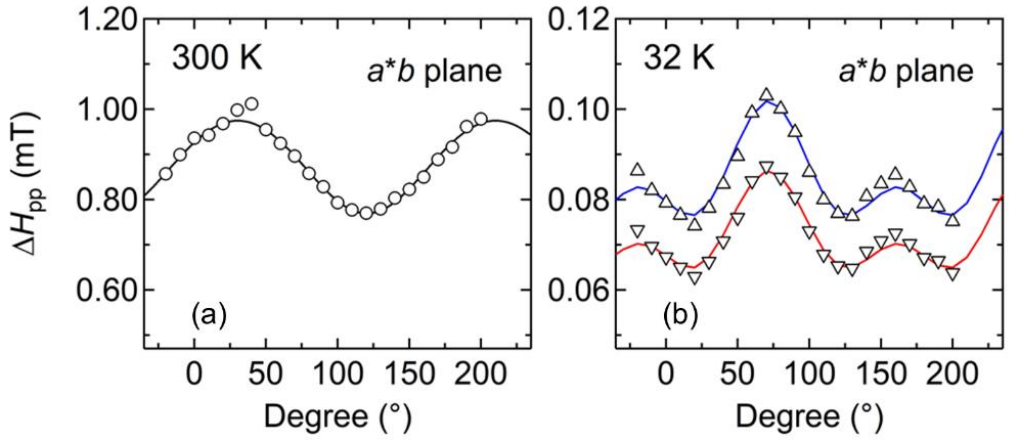

Fig. 5. 15 Angular dependences of Linewidth ΔH_{PP} of sample 2 in the rotation of *a*b* plane with *c*-axis rotation. (a) At temperature 300 K at . Circle represents measured data. Black line represents fitting line of eq. 5.5). (b) At temperature 32 K. Triangle up represents component *1** and triangle down represents component *2**. Blue and red line represent fitting line of eq. 5.15.

The angular dependence of linewidth ΔH_{PP} of sample 2 in the *a*b* plane with *c*-axis rotation in temperature 300 K and 32 K are shown in Fig. 5.15 (a) and (b) respectively. Angular dependence of ΔH_{PP} at 300 K show standard anisotropic behavior can be express as:

$$\Delta H_{\mathrm{PP}}{}^2 = \left(\Delta H_{\mathrm{PP}}{}^2\right)_{a^*} cos^2\,\theta + \left(g\Delta H_{\mathrm{PP}}{}^2\right)_b sin^2\,\theta + 2\left(\Delta H_{\mathrm{PP}}{}^2\right)_{a^*b} cos\,\theta\, sin\,\theta \quad (5.15)$$

The maxima of ΔH_{PP} are close to the *a** direction and the minima close to the *b* direction. The behavior of angular dependencies of ΔH_{PP} remain unchanged until around 100 K. At 32 K close to the T_{sp}, the angular dependence shows different behavior as described by eq. 5.16. According to Nakamura, this behavior is dipole-dipole spin interaction which can be expressed as [81]:

$$\Delta H_{\mathrm{PP}} = h_{\mathrm{D}}(3\cos^2\theta - 1)^2 \quad (5.16)$$

where h_{D} local dipole field and the minima close to the *b* direction. This angular dependence of ΔH_{PP} that can be fitted by eq. 5.15 is become criteria for low dimensionality with spin-singlet state [81]. Furthermore, the change of angular dependence of linewidth ΔH_{PP} due to temperature decrease might indicate presence of a change in molecular symmetry.

5.4 Spin-singlet transition mechanism

The magnetic ground state of (BEDT-TTF)Cu[N(CN)$_2$]$_2$ is spin-singlet state which confirm by magnetic susceptibilities χ_{dc} and χ_{S}. Both magnetic susceptibilities have similar transition which is $T_{\mathrm{sp}} \approx 26$ K. ESR spectroscopy results give more in-depth information how spin-singlet state form in this organic compound. The asymmetric spectrum in the ESR spectrum in the low temperature regions explains the presence of two Lorentzian component namely, *1** and *2**, which according to the primitive lattice structure the two components come from two BEDT-TTF molecules that have symmetrical differences. Furthermore, these two BEDT-TTF molecules have different characteristic spectrum when temperatures decrease resulting in an asymmetric total ESR spectrum as already explain in section 5.3.4 about ESR parameters. By assuming both molecules have same spin number, spin-singlet can be formed because of these two magnetically independent BEDT-TTF molecules. Therefore, the mechanism of spin-singlet transition can be considered based on the ESR parameters results.

The mechanism of spin-singlet transition can be considered as a change of zig-zag spin chain from uniform exchange coupling *J* at high temperature regions into alternating exchange coupling *J* at low temperature regions, as shown in Fig. 5.16. The uniform spin chain has three-dimensional (3D) BEDT-TTF arrangement which connected by transfer integral *t* and *t*'. In high temperature regions, (BEDT-TTF)Cu[N(CN)$_2$]$_2$ is considered to have the itinerant electron in semimetal state based as previously mentioned. However, Hubbard band can be observed from infrared reflectivity measurement at 300K which indicated that this organic compound has localized electron along *c*-axis directions. This means that interaction of two BEDT-TTFF molecule along *t*' is relatively weak. Therefore, the ESR spectroscopy detected one symmetric spectrum as indication of one localized spin site from uniform *J* in 3D BEDT-TTF molecules arrangement as shown in Fig. 5.16 (a). When temperature decreases, (BEDT-TTF)Cu[N(CN)$_2$]$_2$ has paramagnetic insulating state that indicates strongly correlated system

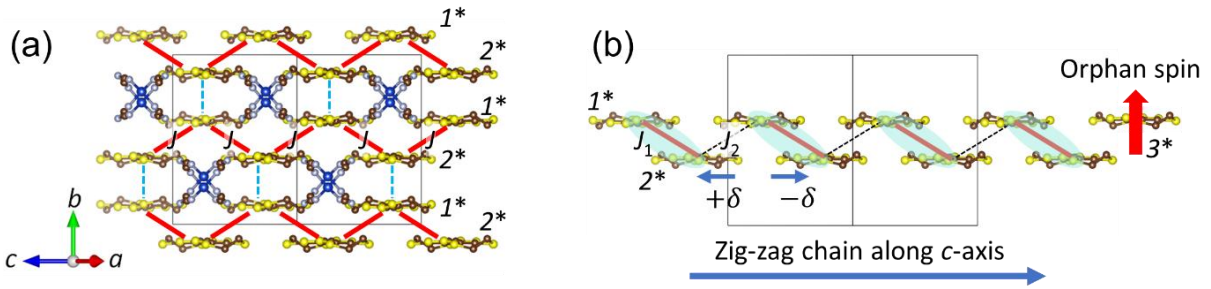

Fig. 5. 16 (a) Uniform *J* on zig-zag chain corresponding to crystal structure of (BEDT-TTF)Cu[N(CN)$_2$]$_2$ at 300 K with assign of component *1** and *2** to BEDT-TTF molecules. (b) Alternating *J* on zig-zag chain corresponding to 1-dimensional zig-zag chain at spin-singlet transition that is observed around $T_{sp} \approx 26$ K. Red line and blue dashed line correspond to integral *t* and *t*', respectively. Red arrow represents unpaired spin or orphan spin from component *3**.

which generates Mott gap in the semimetal state. As such, ESR spectroscopy detected asymmetric spectrum from two BEDT-TTFF (*1** and *2**) with transfer integral *t* along c-axis direction which indicated two spin sites. Now, this organic compound is considered as one-dimensional (1D) zig-zag chain along the *c*-axis direction as shown in Fig. 5.16 (b). The one-dimensionality of this zig-zag chain is also supports by the results of χ_{dc} and χ_{S} which are almost identical with any crystal morphology directions [80]. Based on ESR parameters results in section 5.3.4, the two BEDT-TTF molecules undergo different changes in their spin site characteristics. The *2** BEDT-TTF molecule has more spin orbit coupling compared to *1** BEDT-TTF molecule. This supports the notion that 1D zig-zag chain along the *c*-axis. In addition, this also explain that the *2** more likely to couple with *1** along transfer integral *t*. Besides, *1** BEDT-TTF molecule has a narrower linewidth ΔH_{PP} compared to *2** BEDT-TTF molecule when temperature decreases. The narrower linewidth gives shorter relaxation time meaning that the energy level is lower. The relaxation time caused by narrower linewidth due to temperature decrease might come from spin-lattice relaxation. This spin-lattice might indicate a molecular symmetry change, supported by the angular dependence of linewidth results in the section 5.3.6. The molecular symmetry change may alter zig-zag chain in the amount of δ. That is why the alternation of zig-zag chain is called as alternating zig-zag chain. When *1** and *2** formed into spin-singlet pair, the exchange coupling *J* changed to J_1 and J_2 according to $\pm\delta$, where J_1 has stronger interaction in the spin-singlet pair compared to J_2 of interaction between spin-singlet pair. This spin-singlet transition in the genuine Mott insulator with alternating spin chain by two magnetically independent molecules might indicate a spin Peierls transition. In conclusion, the asymmetric ESR spectrum parameters provide important insight into the mechanism of spin-singlet transition.

Chapter 6 Xray irradiation effect

In this study, we investigate x-ray irradiation effect on the genuine organic Mott insulator (BEDT-TTF)Cu[N(CN)$_2$]$_2$. This material has 1:1 donor/anion molecule ratio on stoichiometry which generates a half-filling energy band. By x-ray irradiation to this system, we can directly show the effect of random potential to strongly correlated electron system. Additionally, the presence of defects in the SP system might affect fundamental properties of this compound.

6.1 Experimental methods

Resistivity measurements with x-ray irradiation effect will be measures on two single crystals of (BEDT-TTF)Cu[N(CN)$_2$]$_2$. Resistivity measurements were measured using the two-probe method on long axis crystal or *c*-axis direction with an electrometer and voltage is set to constant value equal to 1 V. Both samples will measure with different experimental setup. For x-ray time dependence of resistivity measurement, a continuous x-ray irradiation is directly irradiated to the single crystal with specification x-ray lamp is Tungsten tube with 40 kV and 20 mA. Also, a specific temperature control system was built for this experiment (appendix AP.3). The shielding material used for this experimental setup is cooper, manganin as heating element and PT 100 as temperature control sensor. The resistivity time dependence measurement is done 0-350 h at 310 K. For temperature dependence measurement, the cooling system is same as already explain in chapter 3. The single crystal of (BEDT-TTF)Cu[N(CN)$_2$]$_2$ will discreetly irradiate with various irradiation time from 0-350 h and same specification x-ray lamp.

The FTIR measurement at MID region for x-ray irradiation effect were performed in SPring-8, Japan Synchrotron Radiation Research Institute at BL43IR beam. The x-ray irradiation effect on reflectivity of (BEDT-TTF)Cu[N(CN)$_2$]$_2$ prepared using gradation irradiation method (appendix AP.4). In this method, a single crystal put on cooper plate, and will be partially cover by Pb plate to protect certain area of sample from x-ray irradiation. X-ray will irradiate partiality to certain area by opening Pb plate until 300 h by x-ray lamp from tungsten tube 40 kV and 20 mA. By using this method, one single crystal has area with different irradiation time. Reflectivity measurement in the MID IR region was performed at temperature 300 K.

For x-ray irradiation effect on ESR spectrum, the ESR measurements performed by a conventional X-band ESR spectrometer (JEOL JES-RE3X) with magnetic range 319-326 mT equipped with a He-flow cryostat (Oxford Instruments). The experiments have been done on seven single crystals with various irradiation time such as, 0, 5, 15, 30, 60, 90 and 150 hours (h). Six single crystals will be irradiated separately according to target irradiation time directly to the crystal with x-ray lamp from tungsten tube 40 kV and 20 mA. On pristine sample (0 h), angular dependence measurements have been done in the three different crystal planes as the results already explain in chapter 4. After that temperature dependence will be measured on the g_{mid} principal axes which close *c*-axis direction.

6.2 Results and discussion

The first measurement for x-ray irradiation effect on resistivity is time dependence irradiation at 310 K. The results of the x-ray irradiation time dependence of the resistivity ρ at 310 K are shown in Fig. 6.1. The resistivity shows increasing with increasing the irradiation time up to 30 hours and after that decreases exponentially. ρ_{discrete} represents the resistivity at 310 K from each temperature dependence data for every 12.5 h of X-ray irradiation time. Both ρ and ρ_{discrete} show excellent reproducibility at 310 K. From this result, power fitting function and exponential fitting function can be used to as qualitative analysis find out behavior of resistivity. In this fitting function will define as,

$$\rho_{\text{P}} = \rho_0 + \rho_1(t^{\alpha}) \tag{5.1}$$

$$\rho_{\text{E}} = \rho_2 + \rho_3\left(e^{-\frac{t}{\tau}}\right) \tag{5.2}$$

where ρ_0, ρ_2, and ρ_3 is parameter in resistivity with unit Ωcm, and α and τ constant for time parameter. Both fitting results is well fitted except at time region irradiation between 25 h – 50 h. In the time region 25 h – 50 h, the summation of both fitting functions is not fit in this the region. Because of the summation of two different function cannot be fitted to resistivity data, this can be concluded as qualitatively that there are two different transport mechanism in resistivity time dependence result due to x-ray irradiation effect. In addition, at time region 25 h – 50 h, electronic transport starts to change transport mechanism with 30 h irradiation time as critical point. In comparison to other organic dimer-Mott insulators, such a non-monotonic irradiation effect on resistivity has not been observed yet.

Resistivity measurement for x-ray irradiation effect with temperature dependence have done with irradiation time from 0 until 350 h (hours) as shown in Fig. 6.2 (a). The resistivity of (BEDT-TTF)Cu[N(CN)$_2$]$_2$ increases drastically compared to 0 h irradiation due to increasing x-ray irradiation. The result shows that (BEDT-TTF)Cu[N(CN)$_2$]$_2$ is highly sensitive to x-ray irradiation. At 50 h

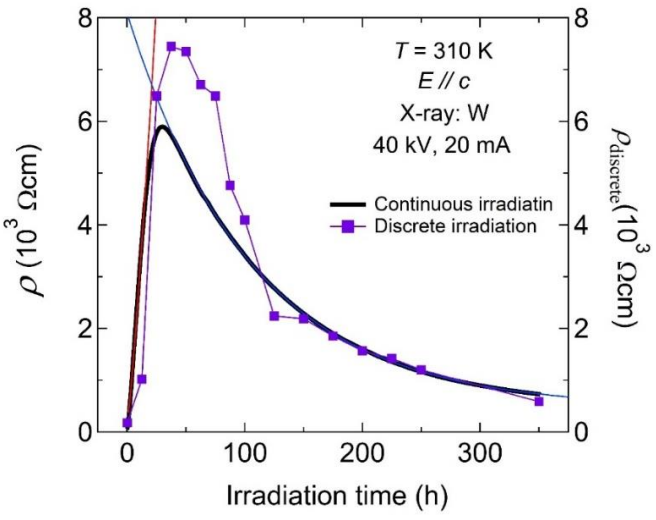

Fig. 6. 1 X-ray irradiation time-dependence of resistivity at 310 K with horizontal axis is the time sample to be irradiated in hour (h) . The data of ρ_{discrete} curve with square symbol from discrete irradiation method every 12.5 h to the sample

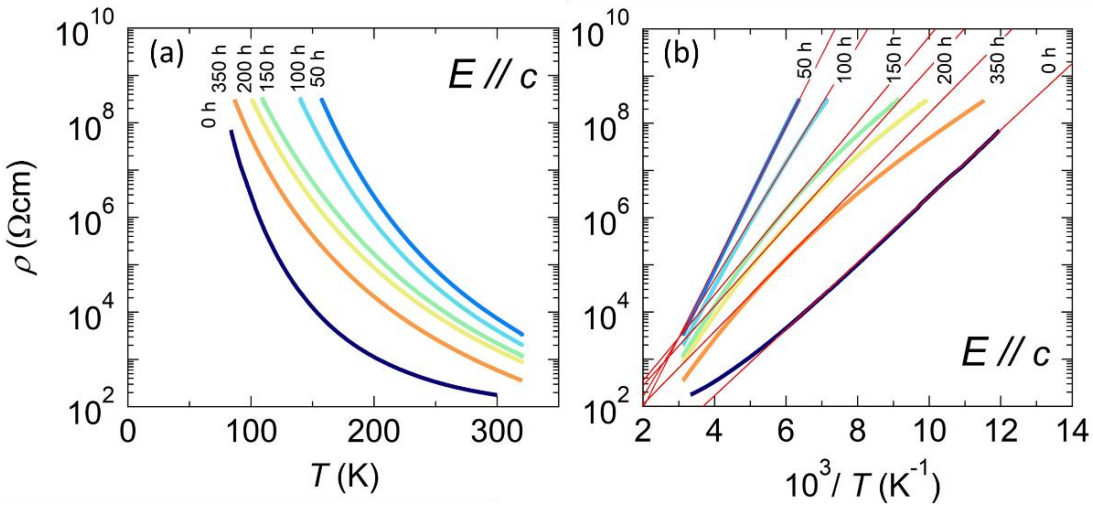

Fig. 6. 2 (a) Temperature-dependence of resistivity of (BEDT-TTF)Cu[N(CN)$_2$]$_2$ with x-ray irradiation effect. (b) Arrhenius plot of Temperature-dependence of resistivity with x-ray irradiation effect

irradiation, the increased resistivity is getting saturated, where the result of 50 h is almost same with 30 h. The resistivity at longer x-rays irradiation time from 50 h until 350 h show different type behavior. At this irradiation time region, resistivity is starting to decrease as irradiation time get longer. Although resistivity value decreases, resistivity at 350 h irradiation time still higher than 0 h irradiation time.

In the report of x-ray irradiation on κ-(BEDT-TTF)$_2$Cu[N(CN)$_2$]Br, the phenomenon of the increase in resistivity can also be obtained [19]. Later the name of organic compounds will be labeled as κ-ET-Br. From this study, κ-ET-Br is originated as superconductor material which can be seen by the sudden drop at resistivity value with superconducting transitions T_c at 11 K. At first, resistivity of 0 h shows a broad hump curve at 100 K with crossover T^* from bad to good metallic and resistivity follows $\rho(T) = \rho_0 + AT^2$. At below 100 h irradiation time, ρ_0 increases and T_c decreases due to by x-ray irradiation. After that at irradiation more than 250 h, the curves show insulating state and at 500 h irradiation time the resistivity become the highest compared to the other x-ray irradiation time. According to Sasaki T. *et. al*., the changes of resistivity on κ-ET-Br indicates MI (metal-insulator) transition phenomena which induced by disorder due x-ray irradiation effect [19]. The result also concludes that the increased resistivity on higher x-ray irradiation time is not Arrhenius type but hopping mechanism in electron between nearest neighbor localized site in the disordered system at higher temperature. This hopping mechanism can be seen by using different model for Arrhenius fitting function [17].

In the previous reported paper, irradiation effect on Dimer Mott insulator have been done with κ-(BEDT-TTF)$_2X$, where X = Cu[N(CN)$_2$]Cl and Cu$_2$(CN)$_3$ [17]. Later the name of organic compounds will be labelled as κ-ET-Cl and κ-ET- Cu$_2$(CN)$_3$. The results show x-ray irradiation effect on the resistivity on that samples decreased as increasing irradiation time in all temperature region. At higher irradiation 620 h κ-ET-Cl shows small increases in resistivity. Also, metallic-like behavior appears κ-ET-Cl where resistivity is decreasing below 50 K. The same reported paper, activation energy decreased with increasing irradiation time. After that at longer irradiation time, the decreasing in the activation

energy is saturated. According to Sasaki T. *et. al.*, the decrease of the activation energy because the formation impurity level induced by the defects in the charge gap between the Hubbard band. In addition, a slight modification of Coulomb potential dimer U_D and/or transfer integral t by the defect in dimer [17].

The increased and decreased of resistivity due to irradiation effect in the (BEDT-TTF)Cu[N(CN)$_2$]$_2$ is quite different compared κ-(BEDT-TTF)$_2X$. The κ-ET-Br shows deviation result at lowest temperature for longer irradiation time, and then the deviation at low temperature result starting try to become linear, but even in 500 h irradiation the deviation still appears at the low temperature. In the current result, ρ(T) vs 10^3/T is linear until 50 h irradiation time without any sign of deviation result. Also, compare the κ-ET-Br, (BEDT-TTF)Cu[N(CN)$_2$]$_2$ has shortest irradiation time to change its electronic properties. In the decreased part of resistivity due to irradiation effect in the (BEDT-TTF)Cu[N(CN)$_2$]$_2$ is also can hardly be compare κ-ET-Cl and κ-ET-Cu$_2$(CN)$_3$. The decreased of resistivity still preserving insulating behavior even at longer irradiation time.

Arrhenius fitting has been done on the resistivity temperature dependence to find out x-ray irradiation effect as shown in Fig. 6.2 (b). The fundamental electronic parameter, such as E_g and ρ_0, is plotted in Fig. 6.3. In the current result, Arrhenius plot with linear feature of only can be seen at below 100 h irradiation time. The Arrhenius plot in Fig. 6.2 (b). shows nonlinear features on the longer irradiation time, while κ-ET-Cl compound is still linear even at longer irradiation time compared to κ-ET-Cl compound. The critical point of irradiation time that shows linearity in Arrhenius plot is around 50 h. As increasing irradiation time, a bent feature in Arrhenius occurs at temperature below 150 K. The bending curve more visible at longer irradiation time. This bent features on curve might be related to hopping mechanism in electronic transport. The bending features in the Arrhenius plot is similar to the deviation in on Arrhenius plot of κ-ET-Br due to longer irradiation time. Therefore, understand Arrhenius plot in the current result, hopping mechanism in electronic transport might be used to analyze longer irradiation.

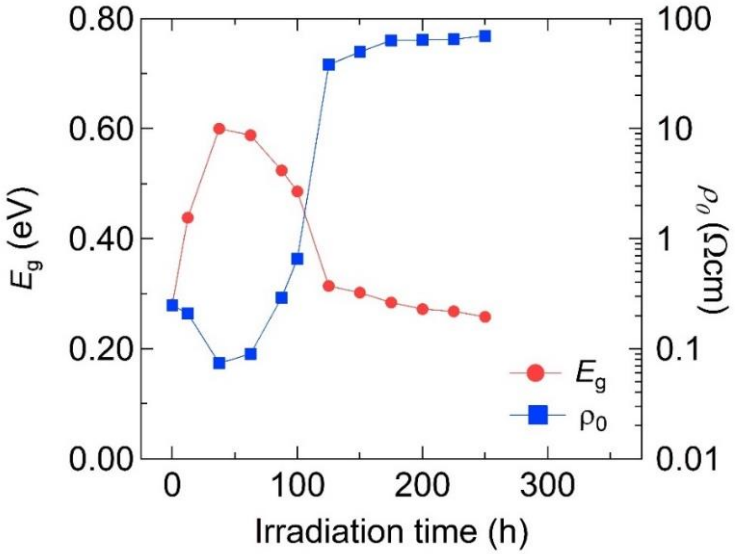

Fig. 6. 3 X-ray irradiation effect on Arrhenius fitting results parameters on resistivity temperature dependences of BEDT-TTF)Cu[N(CN)$_2$]$_2$. Circle is corresponding to the E_g and square is ρ_0 extrapolation of resistivity at high temperature.

Fig. 6.3 shows x-ray irradiation effect energy gap E_g (BEDT-TTF)Cu[N(CN)$_2$]$_2$. The energy gap E_g obtained from the fitting results Arrhenius law in the Fig. 6.2 (b) from 155 - 185 K, where at this temperature regions all resistivity result is linear. The energy E_g in pristine sample or 0 h irradiation is 0.3 eV which has been discuss in chapter 3. At below 37.5 h, resistivity results still follow Arrhenius law which can be seen on the linear behavior in the curves. After sample get x-ray irradiation, the E_g increases up to twice which equal to 0.6 eV at 37.5 h, and then start decreases at longer irradiation time. On the other hand, ρ_0 as extrapolation of resistivity in higher temperature, is decreases from 0.25 to 0.08 Ωcm. The value of ρ_0 also can be defined as conductivity sample $1/\rho$ ($\Omega^{-1}cm^{-1}$) at higher temperature shows at 37.5 h has higher conductivity compared to 0 h at higher temperature limit. The energy E_g at more than 50 h irradiation starting decreases with relatively small differences is about 0.03 eV for each x-ray irradiation time. After 100 h irradiation time, there is 0.1 eV differences between 100 h with 125 and then decreases in E_g is get saturated. In addition, at longer irradiation electronic transport do not follow Arrhenius law because a bent occurs on the curve at low temperature. This bending curves from 125 h – 350 h x-ray irradiation may relate to hopping mechanism in electronic properties.

The hopping mechanism can be explained by variable-range hopping model (VRH). In this model, the Arrhenius law fitting function will be modified by putting another parameter that is β which depend on dimensionality *n* i.e., one, two, and three dimensional. Equation 5.3 shows the VRH fitting function,

$$\rho = \rho_0 e^{\left(\frac{T_0}{T}\right)^{\beta}} \tag{5.3.a}$$

$$\beta = \frac{1}{n+1} \tag{5.3.b}$$

where T_0 as temperature coefficient. The VRH model is based on thermally assisted hopping of charge carriers between the localized state of an electron near the Fermi level at low temperature. When an electron moves one localized state to another state, it will generate quantized energy between those two states due to wave function overlapping each other. Furthermore, the electron must exchange energy with phonon, or possibly a spin wave, for each time it moves. Therefore, energy for an electron to hopping is obtained from a phonon [36, 37]. A hopping electron will always try to find the lowest activation energy E_a and the shortest hopping distance. However, both conditions are not always be satisfied at same time [38]. Therefore, electron will find an optimum hopping distance *r* to get a maximum probability *P* with this relation,

$$P \sim e^{\left(\frac{-2r}{a} - \frac{E_a}{k_B T}\right)} \tag{5.4.a}$$

$$E_a \sim \frac{1}{g_0 r^3} \tag{5.4.b}$$

g_0 is the density of state, in the case β =1/4 where n = 3, the Mott VRH model is using assumption that

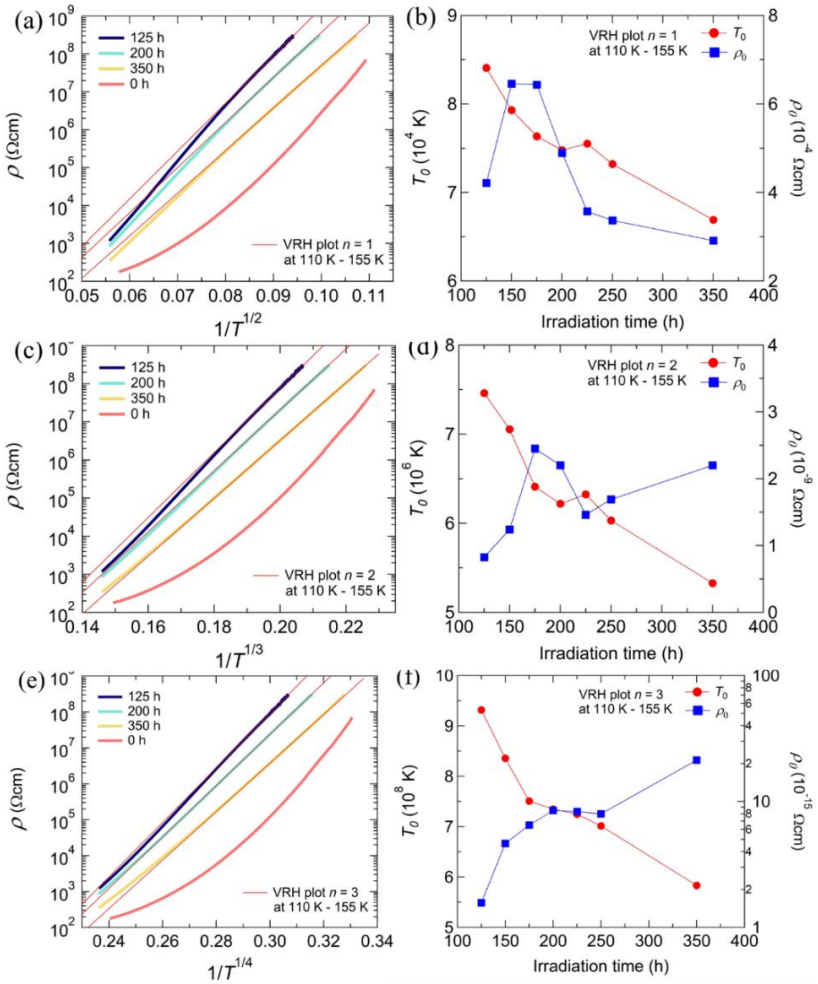

Fig. 6. 4 (a),(b) Resistivity ρ(T) vs $1/T^2$ and parameters from 100 h – 350 h irradiation corresponds to VRH fitting function or ES model, (c),(d) Resistivity ρ(T) vs $1/T^3$ and parameters from 100 h – 350 h irradiation to VRH fitting function n = 2 in two dimensional, and (e),(f) Resistivity ρ(T) vs $1/T^4$ from and parameters 100 h – 350 h irradiation to VRH fitting function n = 3 in three dimensional

the density of states near the Fermi level is constant. In addition, because phonon assisted hopping of localized electron to other states, at low temperature hopping length increasing with decreasing temperature [36,38]. Efros and Shklovskii proposed VRH ES model that the long-range Coulomb interaction between the localized electrons at $\beta = 1/2$ where $n = 1$. In this model, E_a is proportional to 1/r as the Coulomb potential. This Coulomb interaction is long range interaction between localized electrons causes the density of state near the Fermi level will vanish, and then creating a gap near the Fermi level [39].

Fig. 6.4 shows all VRH fitting calculation for longer irradiation time and fitting has been done at 110 K – 155 K. For $1/T^2$ related to VRH ES model $n = 1$, the result is not well fitted compared to another n dimension. The result show at 125 h, $\rho(T)$ is not linear with fitting function, especially at temperature higher than 155 K, and after 200 h irradiation linear behavior will appears. The same tendency behavior in fitting result of $1/T^2$ also can be seen in $1/T^3$ except for $1/T^4$. Fig. 6.4 (e) show resistivity $\rho(T)$ in all irradiation time at temperature scale $1/T^4$ has linear behavior and almost fitted with VRH function. For parameter T_0 as temperature coefficient, in all fitting result show T_0 is decreases

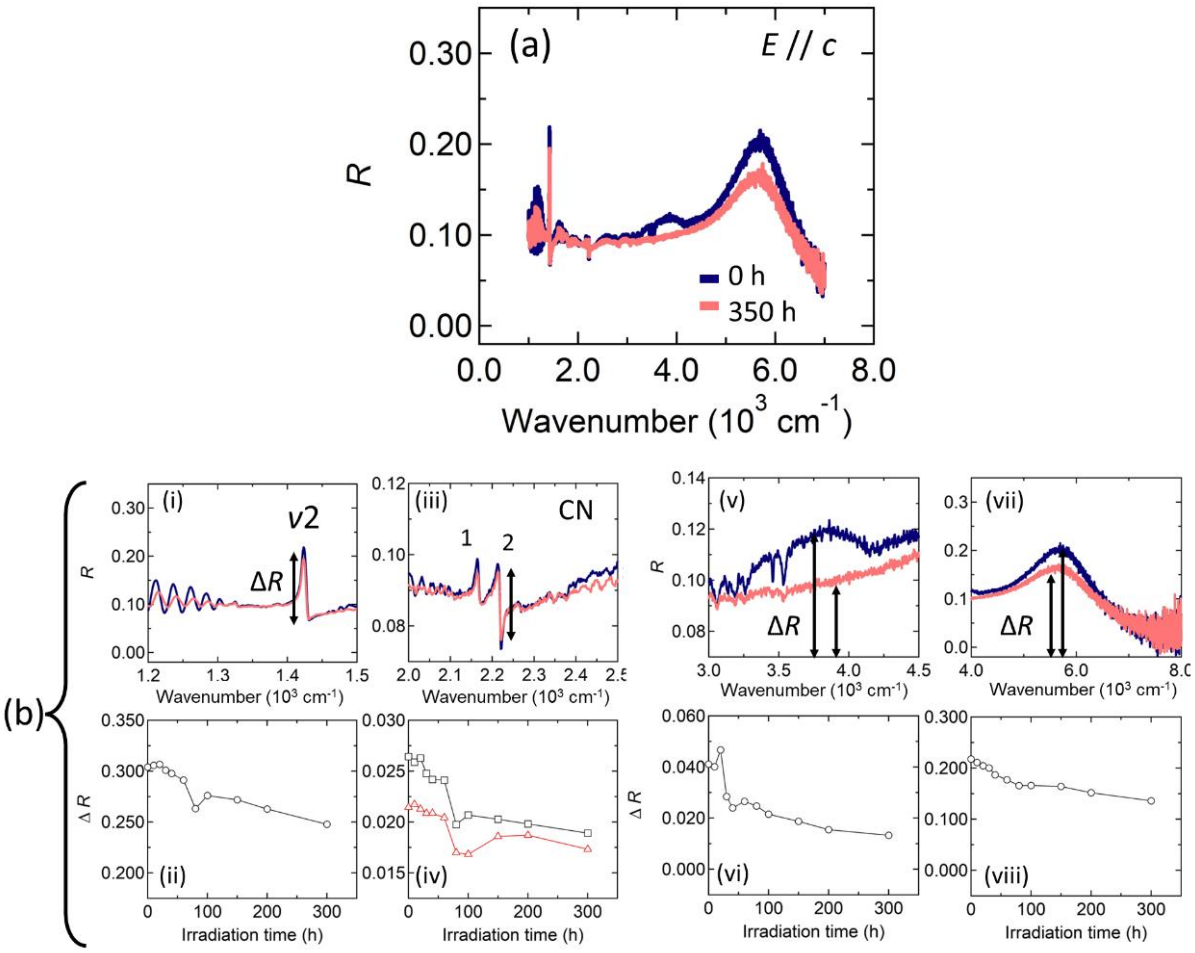

Fig. 6. 5 X-ray irradiation effect on reflectivity of (BEDT-TTF)Cu[N(CN)$_2$]$_2$ along *c*-axis direction at 300 K. Irradiation effect on vibration mode: (b.I) vibration mode *v*2. (b.II) Δ*R* vs irradiation time mode *v*2. (b.III) vibration mode CN bond: square is no 1 and triangle no 2. (b.II) Δ*R* vs irradiation time mode CN. Irradiation effect on charge excitation: (c.I) Isotropic band (see chapter 3). (c.II) Δ*R* vs irradiation Isotropic band. (c.III) Hubbard band. (c.IV) Δ*R* vs irradiation Hubbard band. Δ*R* is total intensity from top peak to the bottom peak.

with increasing irradiation time which this tendency already can be seen in Arrhenius fitting result for E_g. In contrary, for parameter ρ_0 in all fitting result has different behavior which may relate to linearity in fitting calculation. The higher *n* dimensional for calculation, the same trait ρ_0 will appear in the result which in this case $n = 2$ and $n = 3$ show increases ρ_0 with increasing irradiation time. Therefore, VRH model for $n = 2$ and $n = 3$ is suitable for x-ray irradiation effect on resistivity result. Assuming density of states is same for all irradiation time and hopping distance *R* is define as $R \sim 0.4\xi(T_0/T)^{1/4}$ [41], that is mean hopping distance *R* it is getting smaller with increasing irradiation time. Therefore, resistivity decreasing because localized electron more easily to hops another state.

Fig. 6.5 shows x-ray irradiation effect on reflectivity (BEDT-TTF)Cu[N(CN)$_2$]$_2$ along *c*-axis direction at 300 K. The results shows that x-ray irradiation affect vibration modes and charge excitation. Fig. 6.5 (b. I-IV) shows irradiation effect on vibration mode *v*2 and CN bonding no 1 and no 2, and relation Δ*R*, total intensity from top peak to the bottom peak, with x-ray irradiation time. For vibration mode *v*2, x-ray irradiation effect decreased Δ*R* by increasing irradiation time, the percentage lose at

higher irradiation time about 20%. There are two stretching mode CN is detected in this measurement located at wavenumber 2163.8 cm^{-1} and 2212.9 cm^{-1}. X-ray irradiation affecting both stretching mode CN which reduced the intensity of ΔR by increasing irradiation time. The CN mode no 1 is the most sensitive to x-ray irradiation with percentage lose around 30%, while CN mode no 2 has percentage lose around 20%. The charge excitation also affected by x-ray irradiation time. Charge excitation of isotropic band almost completely disappeared by x-ray irradiation time with percentage lose 70%. For Hubbard band, the percentage lose is about 40 % due x-ray irradiation time.

In the study of x-ray irradiation effect on κ-(BEDT-TTF)$_2X$, from optical reflectivity of κ-ET-Cl. The results show that CN-bond defects will occur in anion layer and the defects work as a random potential to the conduction electrons in BEDT-TTF molecule layer. This random potential is known as the randomness effect which creates Anderson-type electron localization. Furthermore, the fundamental electronic parameters such as the intra-dimer transfer energy t and effective Coulomb energy of the dimer site are not affected by x-ray irradiation [18]. In addition, x-ray irradiation affecting inter band transition Mott-Hubbard band and dimer band in mid-IR region by reducing spectral weight (SW). The reduction on SW of inter band transition was compensated by the in a shifting SW in far-IR which attributed to the Drude peak. The shifted the Drude peak to higher region can be causes by electron localization [40]. In suggested that, x-ray irradiation induced weakly disorder metal state with a Coulomb gap which causes by electron-electron interaction. Therefore, in the last study, conclude that a Coulomb soft gapped there is weakly disordered metal state with Coulomb gap which causes by electron-electron fills the Mott gap [1].

The x-ray irradiation effect on reflectivity of (BEDT-TTF)Cu[N(CN)$_2$]$_2$ is in good agreement with the previous study on κ-(BEDT-TTF)$_2X$. In the current result, there is CN bonding intensity lost from the anion molecule due to x-ray irradiation is absorbed by the copper atom and propagating along the anion chain molecule. However, x-ray irradiation effect also affecting vibration mode $v2$ which mean x-ray irradiation also physically affected BEDT-TTF molecule. This result might be because 1:1 ratio between donor and acceptor molecule which also have close contact of intermolecular distance between BEDT-TTF molecule and Cu[N(CN)$_2$]$_2^-$. As already explain in chapter 3, isotropic band in reflectivity has relation with activation energy E_a in the electronic properties. The disappearance of the isotropic band due to x-ray radiation is confirming the change in the energy gap E_g of electronic properties by x-ray irradiation as shown in Fig. 5. 3. The change in Hubbard band in Fig. 6.5 (c.III-IV) might be not from x-ray irradiation effect. As already explain in chapter 3, the isotropic band is located close to Hubbard band which mean the large charge excitation peak in the reflectivity is summation of both energy band. When x-ray irradiation affecting isotropic band, it is affecting total summation energy band but preserving the density of Hubbard band.

Fig. 6.6 show x-ray irradiation effect on ESR parameters g-value and linewidth ΔH_PP. The fitting procedure using same method and assumption as explain in chapter 4. (eq. 4.7 and 4.8). There

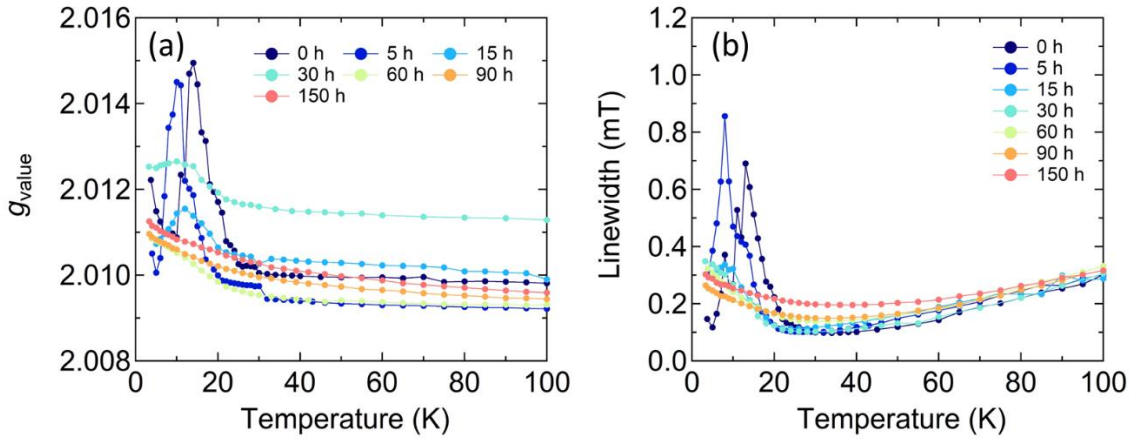

Fig. 6. 6 X-ray irradiation effect on the ESR spectrum parameters: (a) g-value and (b) Linewidth ΔH_{PP}

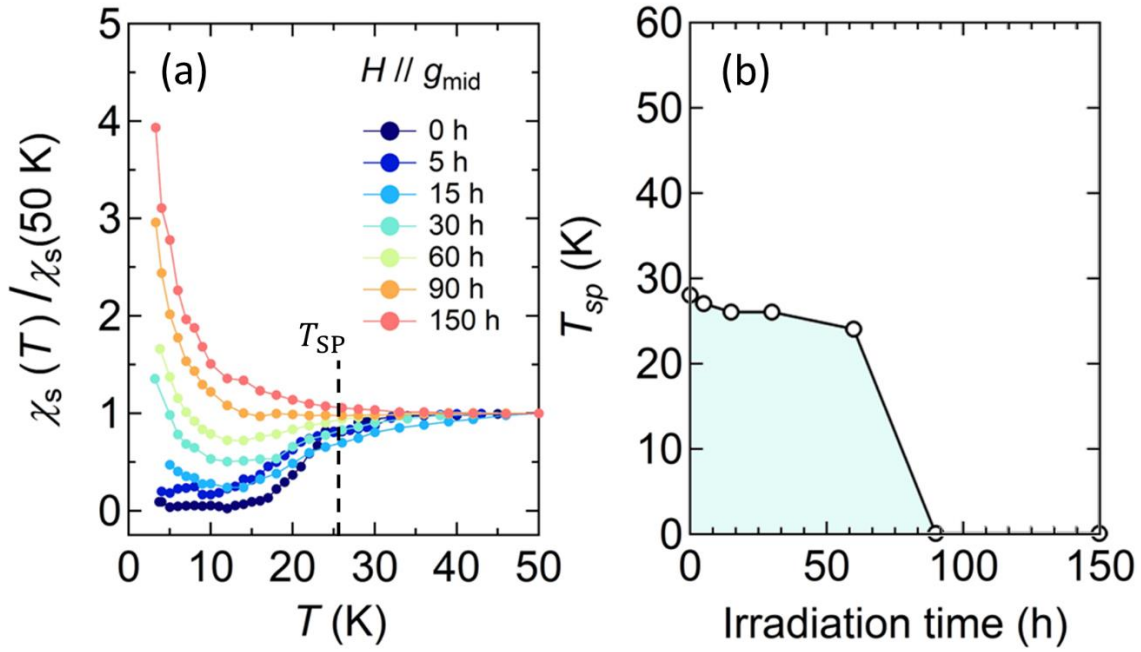

Fig. 6. 7 (a) χ_s of irradiated samples of (BEDT-TTF)Cu[N(CN)$_2$]$_2$. The data normalized to 50 K. The results show Spin-gap suppression. (d) X-ray irradiation on the temperature singlet transition *T*sp

are seven single crystals with various irradiation time such as, 0, 5, 15, 30, 60, 90 and 150 h. The g-value of main spectrum of pristine sample (0 h) is remain constant by decreasing temperature from higher temperature region to 25 K and start to increase with peak maximum around 12 K. The linewidth also has similar behavior with same peak maximum around 12 K. For irradiated sample, this peak of both parameters is start moving toward to the lowest temperature compared to pristine sample. At longer irradiation time, the peak disappears and only remains the large hump of the peak. Fig. 6.7 shows the temperature dependence of χ_S in samples with different x-ray irradiation times. Each χ_S value is normalized by the value at 50 K. The irradiated samples show a suppression of the spin singlet transition and enhancement of the Curie component by increasing irradiation time. As already explain in the chapter 4, from the narrowest to the peak in linewidth ΔH_{PP} is a precursor condition for (BEDT-TTF)Cu[N(CN)$_2$]$_2$ to reaching spin singlet state. This means by increasing irradiation time to

single crystal is affected forming of spin singlet between localize BEDT-TTF molecules. The longer irradiation time will be increasing more disorder as already proven in reflectivity data as defect as shown in Fig. 6.5. These results indicate that a spin-singlet transition is hardly formed by increasing disorder introduced by x-ray irradiation for irradiated sample. Because of spin-singlet hardly to form, the spin-gap is become suppressed, and the Curie component also become enhanced as shown in Fig. 5. 7. Therefore, the spin singlet temperature T_{SP} in Fig. 6.7 (b) is decreased with increasing irradiation and eventually disappeared at longer irradiation time regions.

Chapter 7 Summary

The fundamental properties of Mott insulating state of (BEDT-TTF)Cu[N(CN)2]2 have been established by the transport, infrared optical spectra, and the static and ESR magnetic measurements, including x-ray irradiation effects on them.

The Mott gap of this system has been well established by resistivity and infrared optical spectra. The resistivity results show that this organic compound has higly insulating resistivity with istropic energy gap, about 0.3 eV, at all crystal morphology direction. The BEDT-TTF molecular charge of +1 has been proved by the vibrational modes of *v*2 and *v*27 with use of the empirical equations. We found that the lowest interband excitation is isotropic at about 0.4 eV by the optical spectra measurements. Above the excitation, Hubbard band excitation with a large anisotropy appears at 0.7 eV, which is associated with the one-dimensional electronic system. These optical properties correspond well with the band calculation results by the tight binding approximation method and first principle DFT calculations except for the band gap due to the electron correlations. From these calculations (BEDT-TTF)Cu[N(CN)2]2 is expected to have a nodal point along the c-direction in the crystal. This compound has a zig-zag chain pattern of BEDT-TTF molecules along the c-axis, which make this crystal quasi-one-dimensional. When the chain experiences structural change, e.g., dimerization of BEDT-TTF molecules the gap formation on all the nodal lines easily occurs.

The magnetic properties obtained by DC magnetization and ESR spectroscopy show that (BEDT-TTF)Cu[N(CN)2]2 has a spin-singlet ground state with temperature $T_{sp} \approx 26$ K. Fundamentally, the spin singlet state is formed by two spins of two BEDT-TTF molecules, which suggests that an alternating spin chain by two magnetically independent molecules occurs together with the opening of the spin gap, i.e. , spin Peierls transition.

In the studies of irradiation effect to the fundamental properties, the x-ray irradiation affects the electric, optical, and magnetic properties of the crystal. The resistivity shows the non-monotonic curve which increases drastically at irradiation time before 30 hours and decays exponentially after 30 hours. These results give two different electronic properties mechanism: Arrhenius transport mechanism and variable range hopping mechanism. This change in electronic properties due to x-ray irradiation affecting isotropic band of electronic properties. Irradiation of x-ray suppressed the spin gap and temperature T_{sp} of the spin singlet, resulting in the increase of Curie type impurity contributions which relate with unpair spin or orphan spin. These results also give some support evidence to confirm spin singlet state is spin-Peierls state because the state is vulnerable to the disorder.

Appendix

AP. 1 4 probe method vs 2 probe method

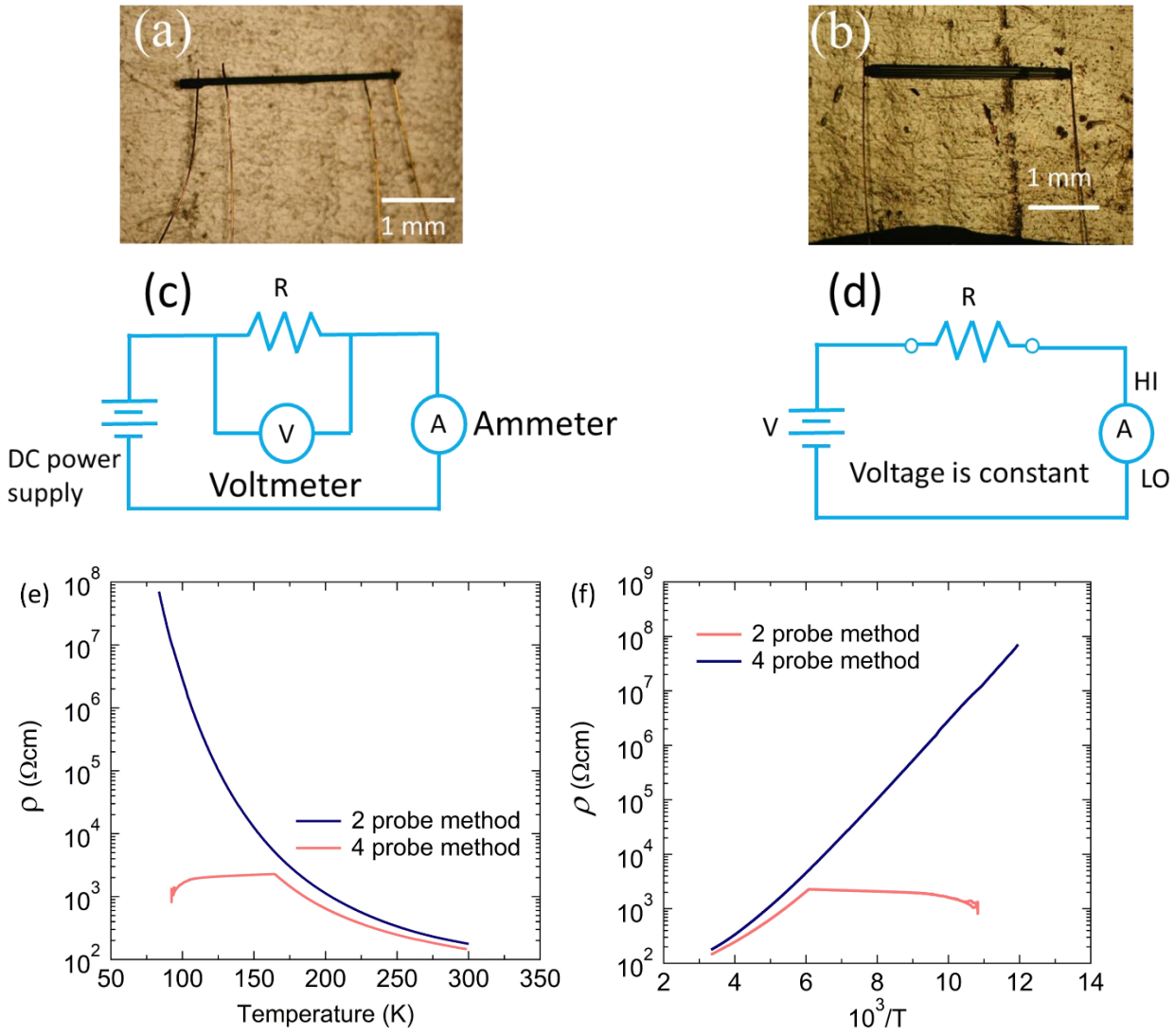

Fig. AP. 1 (a) Sample with 4 probe method attached with gold wire. (b) Sample with 2 probe method attached with gold wire. The gold wire glued by carbon paste. From gold wire to probe measurement using silver paste. (c) Concept figure for four probe method circuit. (d) Concept figure for two probe method circuit. (e) The resistivity result of 4 probe method and 2 probe method. (f) Arrhenius plot of resistivity result.

AP. 2 Polyacetal rod: sample holder for DC magnetization measurement

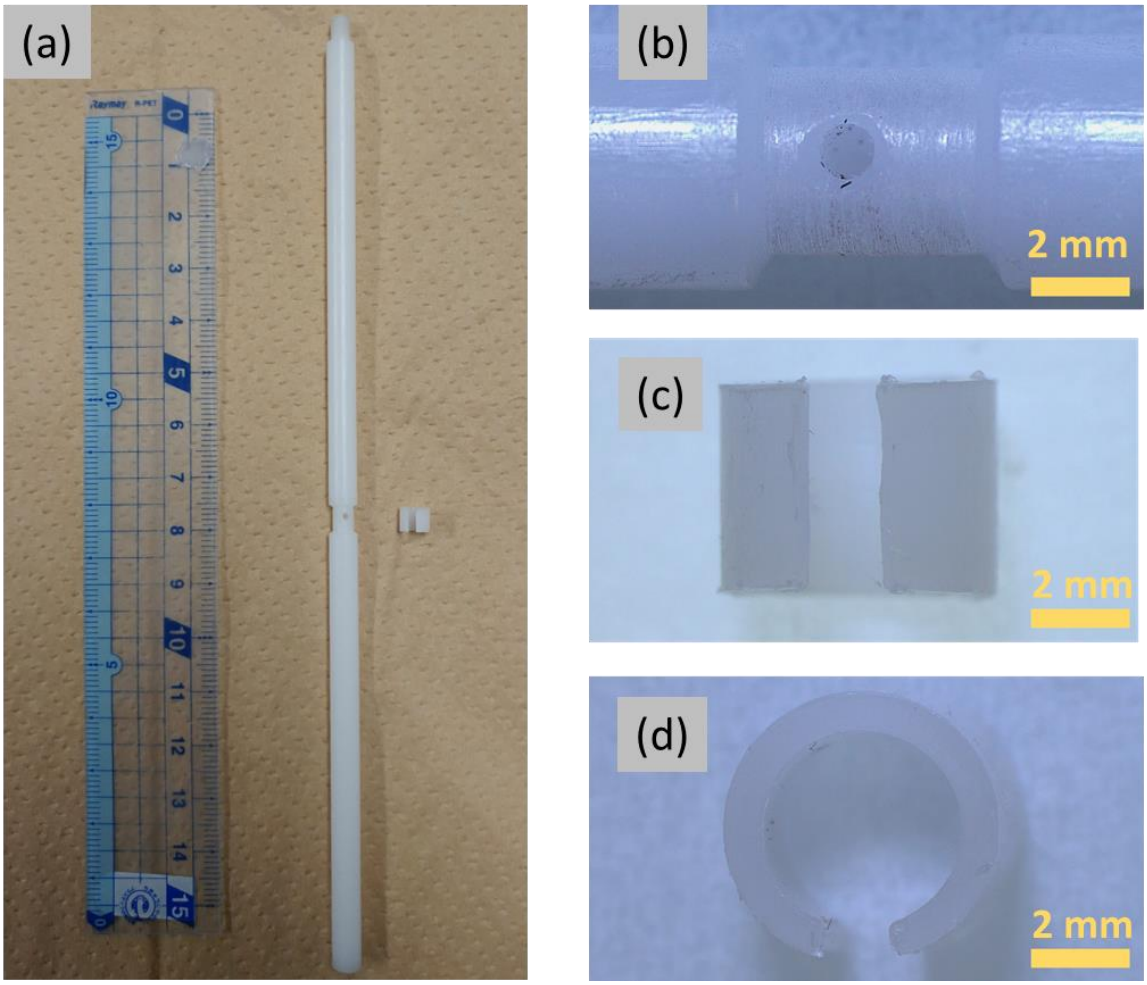

Fig. AP. 2 (a) Polyacetal rod for none grease method of DC magnetization measurement. (b) hole for sample placement, where the hole is perpendicular to the field direction. Shielding for hole sample placement (c) side view and (d) top view

AP. 3 Quartz rod: sample orientation in the ESR spectroscopy measurement

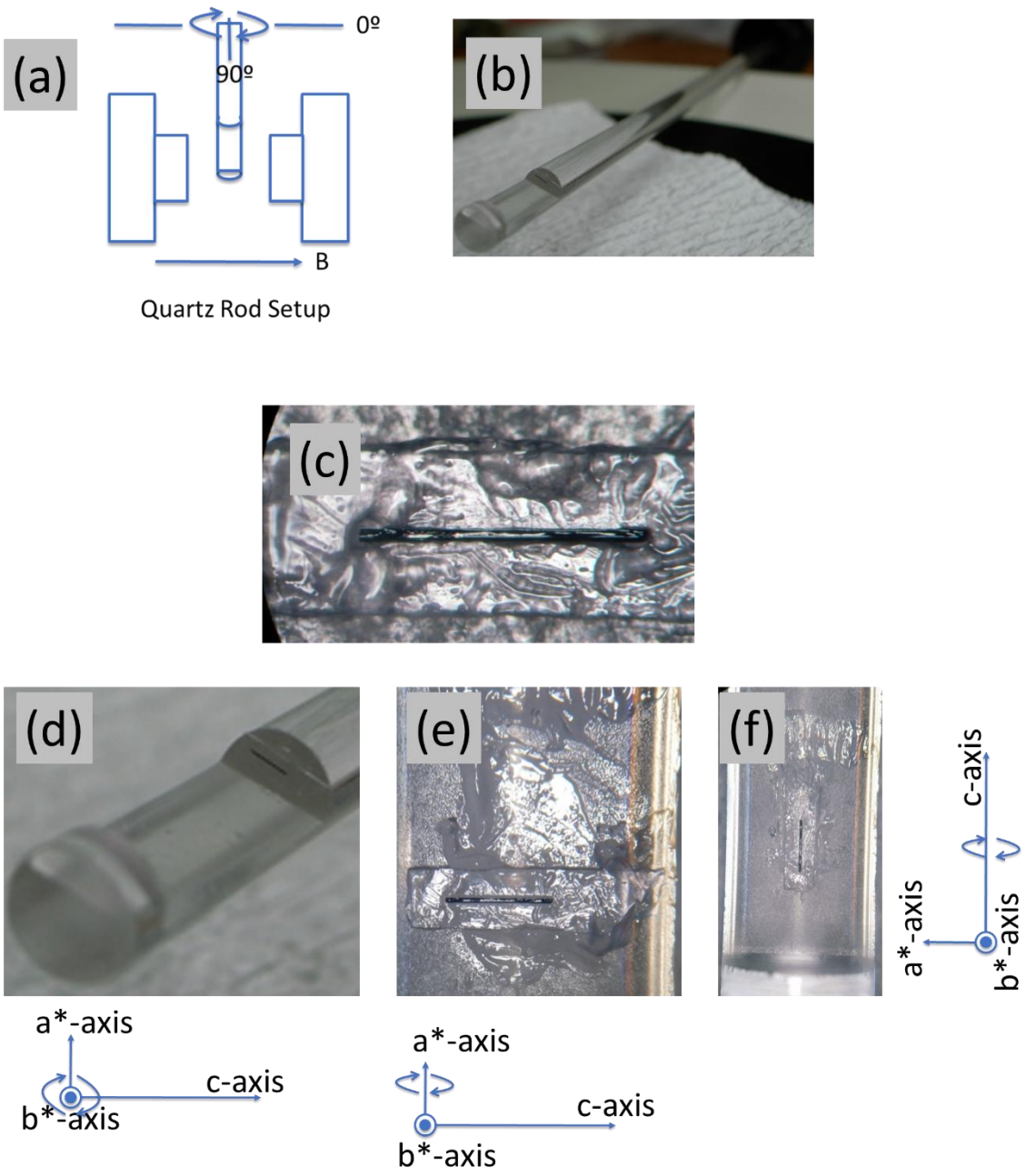

Fig. AP. 3 (a) Sample orientation for ESR spectroscopy measurement. (b) Quartz rod as sample holder and rotator. (c) Sample placement on plastic sheet which glued by silicon grease. (d) rotational axis of *ac* plane with *b**-axis rotation. (e) rotational axis of *bc* plane with *a**-axis rotation. (f) rotational axis of *ab* plane with *c*-axis rotation.

AP. 4 Time dependence of resistivity experimental setup and background check result

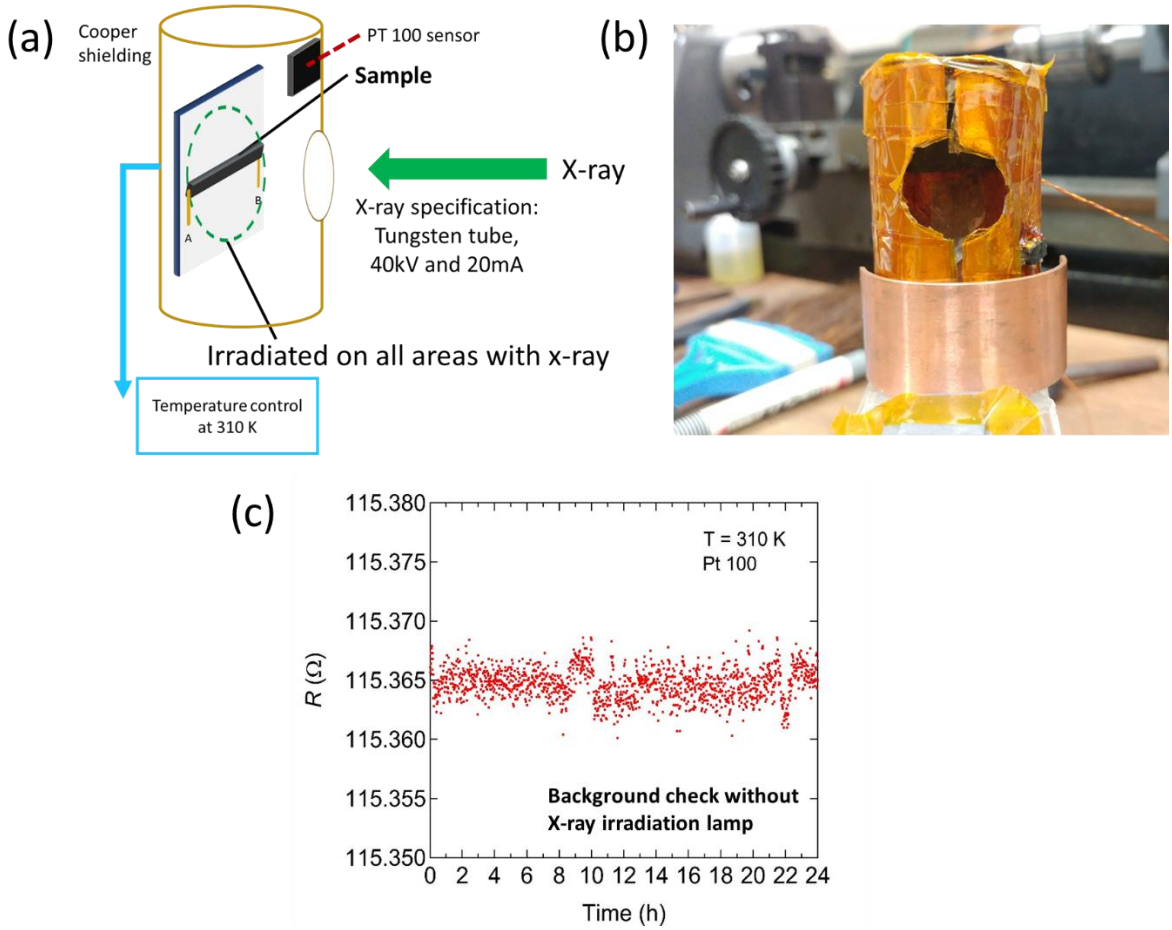

Fig. AP. 4 (a) Concept figure of cooling set-up x-ray irradiation time dependence of resistivity. (b) Photo of cooling system. The shielding material used for this experimental setup is cooper, manganin as heating element and PT 100 as temperature control sensor. (c) Resistance background check with continuous x-ray irradiation to the cooling system. The temperature is set to 310 K. The result shows temperature control system works well which can be seen at resistance background of sensor is linier.

AP. 4 Gradation method: preparation sample for reflectivity measurement with x-ray irradiation effect

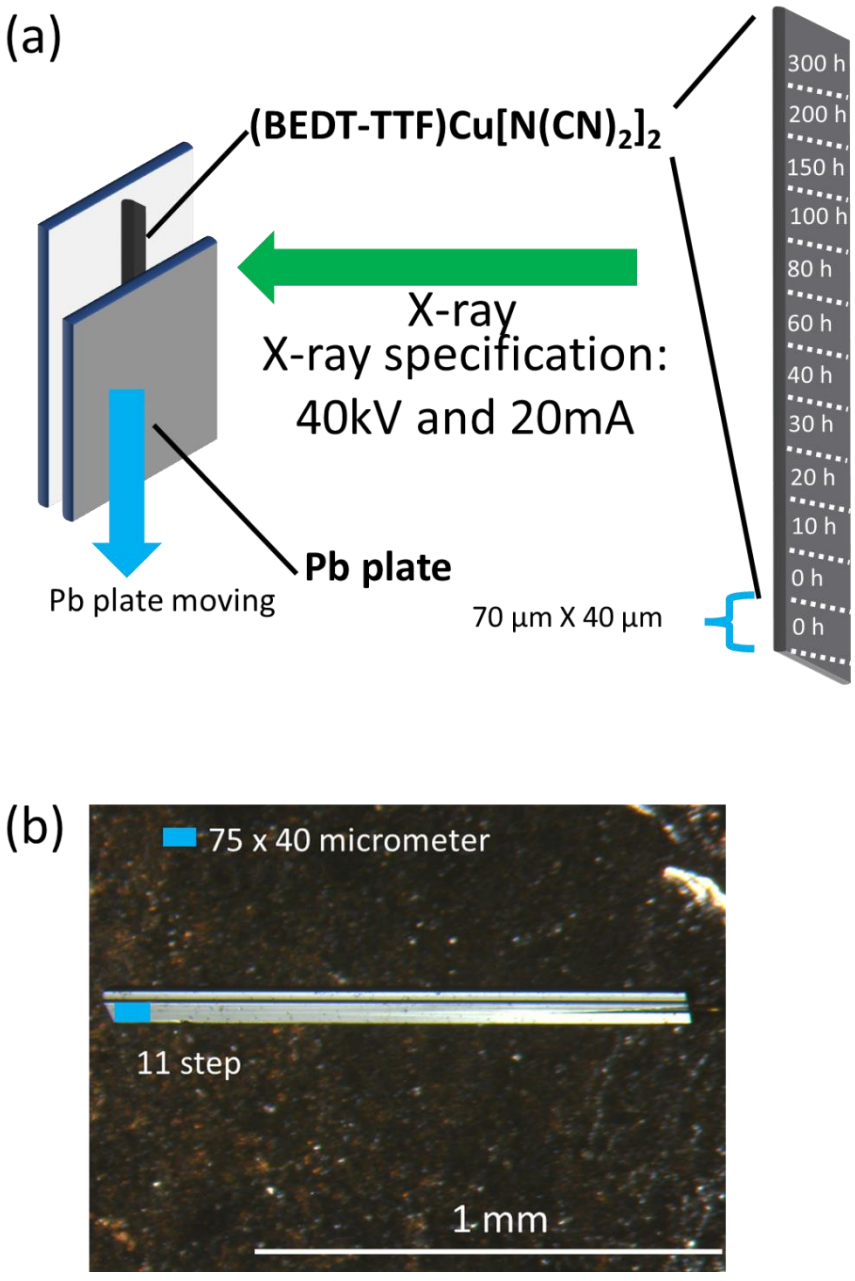

Fig. AP. 5 (a) Sample preparation set up for gradation method. The setup used Cooper plate as sample holder. Pb plate to protect unwanted area from x-ray irradiation. The movement of Pb plate is controlled by program with time Moving program 0, 10, 20, 30, 40, 60, 80, 100, 150, 200 and 300. (b) Sample of gradation method.

Conferences and Workshops

[1] M. K. Nuryadin, S. Iguchi, N. Yoneyama, Y. Oshima, T. Tsumuraya, T. Moriwaki, Y. Ikemoto and T. Sasaki, ESR studies on spin-singlet transition in organic salt (BEDT-TTF)Cu[N(CN)$_2$]$_2$, Poster presentation, The 141st IMR Lecture Meeting, Institute material of science, Tohoku University, Sendai, Miyagi, Japan, November 30, and December 01 (2021).

[2] M. K. Nuryadin, S. Iguchi, N. Yoneyama, Y. Oshima, T. Tsumuraya, T. Moriwaki, Y. Ikemoto and T. Sasaki, X-ray irradiation effect on spin-singlet transition in organic salt (BEDT-TTF)Cu[N(CN)$_2$]$_2$, Poster presentation, Symposium CRCMS 4th and GPMS 5th, Tohoku University, Sendai, Miyagi, Japan, November 25-28 (2021).

[3] M. K. Nuryadin, S. Iguchi, N. Yoneyama, Y. Oshima, T. Tsumuraya, T. Moriwaki, Y. Ikemoto and T. Sasaki, ESR studies on spin-singlet transition in organic salt (BEDT-TTF)Cu[N(CN)$_2$]$_2$, Poster presentation, The Physical Society of Japan Autumn meeting, Virtual conference, Japan, September 20-23 (2021).

[4] M. K. Nuryadin, S. Iguchi, N. Yoneyama, Y. Oshima, T. Tsumuraya, T. Moriwaki, Y. Ikemoto and T. Sasaki, X-ray irradiation effect on spin-singlet transition in organic salt (BEDT-TTF)Cu[N(CN)$_2$]$_2$, Poster presentation, The 140th IMR Lecture Meeting, Institute material of science, Tohoku University, Sendai, Miyagi, Japan, May 26 (2021).

[5] M. K. Nuryadin, S. Iguchi, N. Yoneyama, Y. Oshima, T. Tsumuraya, T. Moriwaki, Y. Ikemoto and T. Sasaki, X-ray irradiation effect on spin-singlet transition in organic salt (BEDT-TTF)Cu[N(CN)$_2$]$_2$, Poster presentation, The Physical Society of Japan Annual meeting (76th), Tokyo University, virtual conference, Japan, March 12-15 (2021).

[6] M. K. Nuryadin, S. Iguchi, N. Yoneyama, Y. Oshima, T. Tsumuraya, T. Moriwaki, Y. Ikemoto and T. Sasaki, Studies of spin states in (BEDT-TTF)Cu[N(CN)$_2$]$_2$ by electron spin resonance, Presentation, The Physical Society of Japan Autumn meeting, Kumamoto University, virtual conference, Japan, September 08-11 (2020).

[7] M. K. Nuryadin, S. Iguchi, N. Yoneyama, Y. Oshima, T. Tsumuraya, T. Moriwaki, Y. Ikemoto and T. Sasaki, X-ray irradiation effect on Spin-Peierls transition in organic salt (BEDT-TTF)Cu[N(CN)$_2$]$_2$, Poster presentation, The 139th IMR Lecture Meeting, Institute material of science, Tohoku University, Sendai, Miyagi, Japan, May 26-27 (2020).

[8] M. K. Nuryadin, S. Iguchi, N. Yoneyama, Y. Oshima, T. Tsumuraya, T. Moriwaki, Y. Ikemoto and T. Sasaki, X-ray irradiation effect in a Mott insulator (BEDT-TTF)Cu[N(CN)$_2$]$_2$, Poster presentation, SMS and GIMRT User Meeting 2019, Institute material of science, Tohoku University, Sendai, Miyagi, Japan, November 27-28 (2019).

[9] M. K. Nuryadin, S. Iguchi, K. Hashimoto, K. Itoh, N. Yoneyama, T. Moriwaki, Y. Ikemoto and T. Sasaki, X-ray irradiation effect on a genuine organic Mott Insulator (BEDT-TTF)Cu[N(CN)$_2$]$_2$,

Poster presentation, The 137th IMR Lecture Meeting, Institute material of science, Tohoku University, Sendai, Miyagi, Japan, May 29 (2019).

[10] M. K. Nuryadin, S. Iguchi, K. Hashimoto, K. Itoh, N. Yoneyama, T. Moriwaki, Y. Ikemoto and T. Sasaki, X-ray irradiation effect on a genuine organic Mott Insulator (BEDT-TTF)Cu[N(CN)$_2$]$_2$, Presentation, The Physical Society of Japan Annual meeting (74th), Kyushu University, Fukuoka, Japan, March 14-17 (2019).

[11] M. K. Nuryadin, S. Iguchi, N. Yoneyama, T. Moriwaki, Y. Ikemoto and T. Sasaki, X-ray irradiation effect on a genuine organic Mott Insulator (BEDT-TTF)Cu[N(CN)$_2$]$_2$, Poster presentation, The Physical Society of Japan Autumn meeting, Doshisha University, Kyotanabe, Kyoto, Japan, September 09-12 (2018).

[12] M. K. Nuryadin, S. Iguchi, N. Yoneyana, and T. Sasaki, X-ray irradiation effect on a genuine organic Mott Insulator (BEDT-TTF)Cu[N(CN)$_2$]$_2$, Poster presentation, The 135th IMR lecture meeting, Institute material of science, Tohoku University, Sendai, Miyagi, Japan, May 23 (2018)

[13] M. K. Nuryadin, S. Iguchi, N. Yoneyana, and T. Sasaki, Electronic properties of a genuine organic Mott Insulator (BEDT-TTF)Cu[N(CN)$_2$]$_2$, Poster presentation, 有機固体若手の会 2018, Echigo Yuzawa, Niigata, Japan, March 15-18 (2018).

References

[1] T. Sasaki, N. Yoneyama and N. Kobayashi, Mott transition and superconductivity in the strongly correlated organic superconductor κ-(BEDT-TTF)$_2$Cu[N(CN)$_2$] Br, Phys. Rev. B 77, 05450 (2008).

[2] J. Hubbard, Generalized Wigner lattices in one dimension and some applications to tetracyanoquinodimethane (TCNQ) salts, Phys. Rev. B 17, 494 (1978).

[3] J. Hubbard, Electron correlations in narrow energy bands, Proc. Roy. Soc. London A 276, 238 (1963).

[4] D. Jérome, A. Mazaud, M. Ribault, K. Bechgaard, K. Bechgaard Superconductivity and K. H. Bechgaard C Oersted, in a synthetic organic conductor (TMTSF)$_2$PF$_6$, J. Physique Lett. 41 (1980).

[5] S. Ishibashi, First-principles electronic-band calculations on organic conductors, Science and technology of advanced materials 10 (2009).

[6] T. Mori, Organic conductors with unusual band fillings, Chemical reviews 104, 4947 (2004).

[7] T. Mori, H. Inokuchi, Y. Misaki, T. Yamabe, H. Mori and S. Tanaka, Crystal Structures of Highly Conducting Iodine Complexes of TTM-TTP, Bulletin of the Chemical Society of Japan 67, 661 (1994).

[8] M. Onuki, K. Hiraki, T. Takahashi, D. Jinno, T. Kawamoto, T. Mori, K. Tanaka and Y. Misaki, Electronic state of a new organic conductor (TTM-TTP)I3 with a one-dimensional half-filled band, Journal of Physics and Chemistry of Solids 62, 405 (2001).

[9] R. Świetlik, K. Yakushi, K. Yamamoto, T. Kawamoto and T. Mori, Infrared and Raman studies of the phase transition in the organic conductor (TTM-TTP)I3, Synthetic metals 150, 83 (2005).

[10] H. Urayama, H. Yamochi, G. Saito, K. Nozawa, T. Sugano, M. Kinoshita, S. Sato, K. Oshima, A. Kawamoto and J. Tanaka, A New Ambient Pressure Organic Superconductor Based on BEDT-TTF with TC Higher than 10 K (TC = 10.4 K), Chem. Lett. 17, 55 (1988).

[11] U. Geiser, J. Schultz, H. H. Wang, D. M. Watkins, D. L. Stuoka and J. M. Williams, Strain index, lattice softness and superconductivity of organic donor-molecule salts Crystal and electronic structures of three isostructural salts κ-(BEDT-TTF)$_2$Cu[N(CN)$_2$]X (X=Cl, Br, I), Physica C. 174, 475 (1991).

[12] H. Taniguchi, M. Miyashita, K. Uchiyama, K. Satoh, N. Môri, H. Okamoto, K. Miyagawa, K. Kanoda, M. Hedo and Y. Uwatoko, Superconductivity at 14.2 K in layered organics under extreme pressure, J. Phys. Soc. Jpn. 72, 468 (2003).

[13] C. Hotta, Classification of quasi-two dimensional organic conductors based on a new minimal model, J. Phys. Soc. Jpn. 72, 840 (2003).

[14] H. H. Wang, U. Geiser, J. M. Williams, K. D. Carlson, A. M. Kini, J. M. Mason, J. T. Perry, H. A. Charlier and A. V. S. Crouch, Phase selectivity in the simultaneous synthesis of the Tc = 12.8 K (0.3 kbar) organic superconductor κ-(BEDT-TTF)$_2$Cu[N(CN)$_2$]Cl or the semiconductor (BEDT-TTF)Cu[N(CN)$_2$]$_2$, American Chemical Society 4, 247 (1992).

[15] J. G. Analytis, A. Ardavan, S. J. Blundell, R. L. Owen, E. F. Garman, C. Jeynes and B. J. Powell, Effect of irradiation-induced disorder on the conductivity and critical temperature of the organic superconductor κ-(BEDT-TTF)$_2$Cu(SCN)$_2$, Phys. Rev. Lett. 96, (2006).

[16] G. Mihély and L. Zuppiroli, Radiation effects in organic metals: The mechanisms of damage production, Philos. Mag. A 45, 549 (1982).

[17] T. Sasaki, H. Oizumi, N. Yoneyama, N. Kobayashi and N. Toyota, X-ray irradiation-induced carrier doping effects in organic dimer-Mott insulators, J. Phys. Soc. Jpn. 76, (2007).

[18] T. Sasaki, N. Yoneyama, Y. Nakamura, N. Kobayashi, Y. Ikemoto, T. Moriwaki and H. Kimura, Optical probe of carrier doping by x-ray irradiation in the organic dimer Mott insulator κ-(BEDT-TTF)$_2$Cu[N(CN)$_2$]Cl, Phys. Rev. Lett. 101, (2008).

[19] N. Yoneyama, T. Sasaki, N. Kobayashi, K. Furukawa and T. Nakamura, X-ray irradiation effect on magnetic properties of Dimer–Mott insulators: κ-(BEDT-TTF)$_2$Cu[N(CN)$_2$]Cl and β′-(BEDT-TTF)$_2$ICl$_2$, Phys. B 405, S244 (2010).

[20] K. Sano, T. Sasaki, N. Yoneyama and N. Kobayashi, Electron localization near the Mott transition in the organic superconductor κ-(BEDT-TTF)$_2$Cu[N(CN)$_2$]Br, Phys Rev. Lett. 104, 217003 (2010).

[21] T. Sasaki, H. Oizumi, Y. Honda, N. Yoneyama and N. Kobayashi, Suppression of superconductivity by nonmagnetic disorder in organic superconductor κ-(BEDT-TTF)$_2$Cu(NCS)$_2$, J. Phys. Soc. Jpn. 80, 104703 (2011).

[22] T. Sasaki, K. Sano, H. Sugawara, N. Yoneyama and N. Kobayashi, Influence of randomness on the Mott transition in κ-(BEDT-TTF)$_2$X, Phys. Status Solidi B 249, 947 (2012).

[23] L. Kang, K. Akagi, K. Hayashi and T. Sasaki, First-principles investigation of local structure deformation induced by x-ray irradiation in κ-(BEDT-TTF)$_2$Cu[N(CN)$_2$]Br, Phys. Rev. B 95, 214106 (2017).

[24] S. Sasaki, K. Hashimoto, R. Kobayashi, K. Itoh, S. Iguchi, Y. Nishio, Y. Ikemoto, T. Moriwaki, N. Yoneyama, M. Watanabe, A. Ueda, H. Mori, K. Kobayashi, R. Kumai, Y. Murakami, J. Müller and T. Sasaki, Crystallization and vitrification of electrons in a glass-forming charge liquid, Science 357, 1381 (2017).

[25] J. M. Williams, A. M. Kini, H. H. Wang, K. D. Carlson, U. Geiser, L. K. Montgomery, G. J. Pyrka, D. M. Watkins and J. M. Kommers, From semiconductor-semiconductor transition (42 K) to the highest-Tc organic superconductor, κ-(ET)$_2$Cu[N(CN)$_2$]Cl (Tc = 12.5 K), Inorganic Chemistry 29, 3272 (1990).

[26] K. Miyagawa, K. Kanoda and A. Kawamoto, NMR Studies on Two-Dimensional Molecular Conductors and Superconductors: Mott Transition in κ-(BEDT-TTF)$_2$X, Chem. Rev. 104, 5635 (2004).

[27] K. Kanoda, Recent progress in NMR studies on organic conductors, Hyperfine Interact 104, 235 (1997).

[28] H. Kino and H. Fukuyama, Phase Diagram of Two-Dimensional Organic Conductors: (BEDT-TTF)$_2$X, J. Phys. Soc. Jpn. 65, 2158 (1996).

[29] H. Ito, T. Ishiguro, M. Kubota and G. Saito, Metal-Nonmetal Transition and Superconductivity Localization in the Two-Dimensional Conductor κ-(BEDT-TTF)$_2$Cu[N(CN)$_2$]Cl under Pressure, J. Phys. Soc. Jpn. 65, 2987 (1996).

[30] S. Lefebvre, P. Wzietek, S. Brown, C. Bourbonnais, D. Jérome, C. Mézière, M. Fourmigué and P. Batail, Mott Transition, Antiferromagnetism, and Unconventional Superconductivity in Layered Organic Superconductors, Phys. Rev. Lett. 85, 5420 (2000).

[31] N. Yoneyama, T. Sasaki and N. Kobayashi, Substitution Effect by Deuterated Donors on Superconductivity in κ-(BEDT-TTF)$_2$Cu[N(CN)$_2$]Br, J. Phys. Soc. Jpn. 73, 1434 (2004).

[32] P. B. Allen, R. M. Wentzcovitch, W. W. Schulz and P. C. Canfield, Resistivity of the high-temperature metallic phase of VO2, Phys. Rev. B 48, 4359 (1993).

[33] C. N. Berglund and H. J. Guggenheim, Electronic Properties of VO2 near the Semiconductor-Metal Transition, Phys. Rev. 185, 1022 (1969).

[34] C. Michel, S. D. Baranovskii, P. J. Klar, P. Thomas and B. Goldlücke, Strong non-Arrhenius temperature dependence of the resistivity in the regime of traditional band transport, Applied physics letters 89, 112116 (2006).

[35] J. S. Blakemore, Semiconductor Statistics, Elsevier, 1962.

[36] N. F. Mott, Metal-Insulator Transitions, London: CRC Press, 2004.

[37] N. F. Mott and E. A. Davis, Electronic Process in Non-crystalline Materials, 2nd ed., Oxford: Oxford university press, 1979.

[38] D. Yu, C. Wang, B. L. Wehrenberg and P. Guyot-Sionnest, Variable range hopping conduction in semiconductor nanocrystal solids, Phys. Rev. Lett. 92, 216802 (2004).

[39] A. L. Efros and B. I. Shklovskii, Coulomb gap and low temperature conductivity of disordered systems, J. Phys. C 8, L49 (1975).

[40] M. Dressel and G. Grüner, Electrodynamics of Solids, Cambridge: Cambridge University Press, 2002.

[41] W. N. Shafarman and T. G. Castner, Critical behavior of Mott variable-range hopping in Si:As near the metal-insulator transition, Phys. Rev. B 33, 3570 (1986).

[42] P. W. Anderson, A Mathematical Model for the Narrowing of Spectral Lines by Exchange or Motion, J. Phys. Soc. Jpn 9, 316 (1954).

[43] Z. H. Wang, E. M. Scherr, A. G. MacDiarmid and A. J. Epstein, Transport and EPR studies of polyaniline: A quasi-one-dimensional conductor with three-dimensional ‘‘metallic’’ states, Phys. Rev. B 45, 4190 (1992).

[44] J. C. Bonner, One-dimensional model systems: Theoretical survey, Journal of Applied Physics 49, 1299 (1978).

[45] J. C. Bonner and M. E. Fisher, Linear Magnetic Chains with Anisotropic Coupling, Phys. Rev. 135, A640 (1964).

[46] T. Yamamoto, M. Uruichi, K. Yamamoto, K. Yakushi, A. Kawamoto and H. Taniguchi, Examination of the Charge-Sensitive Vibrational Modes in Bis(ethylenedithio)tetrathiafulvalene, J. Phys. Chem. B 109, 15226 (2005).

[47] K. Hashimoto, R. Kobayashi, H. Okamura, H. Taniguchi, Y. Ikemoto, T. Moriwaki, S. Iguchi, M. Naka, S. Ishihara and T. Sasaki, Emergence of charge degrees of freedom under high pressure in the organic dimer-Mott insulator β′-(BEDT - TTF)$_2$ICl$_2$, Phys. Rev. B 92, 085149 (2015).

[48] A. Fortunelli and A. Painelli, Ab initio estimate of Hubbard model parameters: A simple procedure appliedto BEDT-TTF salts, Phys. Rev. B 55, 16088 (1997).

[49] O. Kahn, Molecular Magnetism, New York: Wiley-VCH, 1993.

[50] R. L. Carlin, Magnetochemistry, Berlin: Springer-Heidelberg, 1986.

[51] H. Kino and H. Fukuyama, Phase Diagram of Two-Dimensional Organic Conductors: (BEDT-TTF)$_2$X, J. Phys. Soc. Jpn 65, 2158 (1996).

[52] H. Fukuyama, Physics of molecular conductors, J. Phys. Soc. Jpn 75, 051001 (2006).

[53] K. Kanoda, Metal-insulator transition in κ-(ET)$_2$X and (DCNQI)$_2$M: Two contrasting manifestation of electron correlation, J. Phys. Soc. Jpn 75, 051007 (2006).

[54] B. J. Powell and R. H. McKenzie, Quantum frustration in organic Mott insulators: From spin liquids to unconventional superconductors, Reports on Progress in Physics 74, 056501 (2011)

[55] H. Wang, K. Carlson, U. Geiser, A. Kini, A. Schultz, J. Williams, L. Montgomery, W. Kwok, U. Welp, K. Vandervoort, S. Boryschuk, A. Crouch, J. Kommers, D. Watkins, J. Schriber, D. Overmyer, D. Jung, J. Novoa and M.-H. Whangbo, New κ-phase materials, κ-(ET)$_2$Cu[N(CN)$_2$]X. X=Cl, Br and I. The synthesis, structure and superconductivity above 11 K in the Cl (TC = 12.8 K, 0.3 kbar) and Br (TC = 11.6 K) salts, Synthetic metals 42, 1983 (1991)

[56] B. Miksch, A. Pustogow, M. J. Rahim, A. A. Bardin, K. Kanoda, J. A. Schlueter, R. Hübner, M. Scheffler and M. Dressel, Gapped magnetic ground state in quantum spin liquid candidate κ-(BEDT-TTF)$_2$Cu$_2$(CN)$_3$, Science 372, 276 (2001).

[57] T. Furukawa, K. Miyagawa, T. Itou, M. Ito, H. Taniguchi, M. Saito, S. Iguchi, T. Sasaki and K. Kanoda, Quantum Spin Liquid Emerging from Antiferromagnetic Order by Introducing Disorder, Phys. Rev. Lett 115, 077001 (2015).

[58] H.-L. Liu, L.-K. Chou, K. A. Abboud, B. H. Ward, G. E. Fanucci, G. E. Granroth, E. Canadell, M. W. Meisel, D. R. Talham and D. B. Tanner, Structure and Physical Properties of a New 1:1 Cation-Radical Salt, ζ-(BEDT−TTF)PF6, Chemistry of materials 9, 1865 (1997).

[59] T. Kawamoto, K. Kurata, T. Mori and R. Kumai, A New Genuine Mott Insulator: β-(BEDT-TTF)TaF6, J. Phys. Soc. Jpn 90, 103703 (2021).

[60] Y. Shimizu, A. Otsuka, M. Maesato, M. Tsuchiizu, A. Nakao, H. Yamochi, T. Hiramatsu, Y. Yoshida and G. Saito, Molecular diamond lattice antiferromagnet as a Dirac semimetal candidate, Phys. Rev. B 99, 174417 (2019).

[61] A. Otsuka, Y. Shimizu, G. Saito, M. Maesato, A. Kiswandhi, T. Hiramatsu, Y. Yoshida, H. Yamochi, M. Tsuchiizu, Y. Nakamura, H. Kishida and H. Ito, Canting Antiferromagnetic Spin-Order (TN = 102 K) in a Monomer Mott Insulator (ET)Ag4(CN)5 with a Diamond Spin-Lattice, Bulletin of the Chemical Society of Japan 93, 260 (2020).

[62] A. Kiswandhi, M. Maesato, S. Tomeno, Y. Yoshida, Y. Shimizu, P. Shahi, J. Gouchi, Y. Uwatoko, G. Saito and H. Kitagawa, High pressure investigation of an organic three-dimensional Dirac semimetal candidate having a diamond lattice, Phys. Rev. B 101, 245124 (2020).

[63] D. Bergman, J. Alicea, E. Gull, S. Trebst and L. Balents, Order-by-disorder and spiral spin-liquid in frustrated diamond-lattice antiferromagnets, Nature Physics 3, 487 (2007).

[64] Y. Zhang, Y. Ran and A. Vishwanath, Topological insulators in three dimensions from spontaneous symmetry breaking, Phys. Rev. B 79, 245331 (2009).

[65] A. Bondi, van der Waals Volumes and Radii, J. Phys. Chem. 68, 441 (1964).

[66] N. Yoneyama, M. K. Nuryadin, S. Iguchi and T. Sasaki, will be published.

[67] N. Marzari and D. Vanderbilt, Maximally localized generalized Wannier functions for composite energy bands, Phys. Rev. B 56, 12847 (1997).

[68] G. A. Bain and J. F. Berry, Diamagnetic Corrections and Pascal's Constants, Journal of Chemical Education 85, 532 (2008).

[69] J. C. Bonner, H. W. J. Blöte, J. W. Bray and I. S. Jacobs, Susceptibility calculations for alternating antiferromagnetic chains, Journal of Applied Physics 50, 1810 (1979).

[70] J. C. Bonner, S. A. Friedberg, H. Kobayashi, D. L. Meier and H. W. J. Blöte, Alternating linear-chain antiferromagnetic in copper nitrate $Cu(NO_3)_2.2.5H_2O$, Phys. Rev. B 27, 248 (1993).

[71] W. E. Estes, D. P. Gavel, W. E. Hatfield and D. J. Hodgson, Magnetic and structural characterization of dibromo- and dichlorobis(thiazole)copper(II), Inorganic Chemistry 17, 1415 (1978).

[72] J. W. Hall, W. E. Marsh, R. R. Weller and W. E. Hatfield, Exchange Coupling in the Alternating-Chain Compounds catena-Di-μ-chloro-bis(4-methylpyridine)copper(II), catena-Di-μ-bromo-bis(N-methylimidazole)copper(II), catena-Di-μ-chloro-bis(4-methylpyridine)copper(II), catena-[Hexanedione bis(thiosemicarbazonato)] copper(II), catena-[Octanedione bis(thiosemicarbazonato)] copper(II), Inorganic Chemistry 20, 1033 (1981).

[73] J. E. Geusic and L. C. Brown, Computation of the Principal Components of an Asymmetric g Tensor from Paramagnetic Resonance Data, Phys. Rev. 112, 64 (1958).

[74] T. Sugano, G. Saito and M. Kinoshita, Spin relaxation and diffusion in quasi-two-dimensional organic metals: The Bis(ethylenedithio)tetrathiafulvalene compounds P-$(BEDT\text{-}TTF)_2X$ (X =I3 and IBr2), Phys. Rev. B 35, 6554 (1987).

[75] T. Nakamura, T. Nobutoki, T. Takahashi, G. Saito, H. Mori and T. Mori, ESR Properties of κ-Type Organic Superconductors Based on BEDT-TTF, J. Phys. Soc. Jpn 63, 4110 (1994).

[76] M. Dressel, M. Dumm, T. Knoblauch, B. Köhler, B. Salameh and S. Yasin, Charge Order Breaks Magnetic Symmetry in Molecular Quantum Spin Chains, Advances in Condensed Matter Physics 2012, 1 (2012).

[77] C. P. Poole and H. A. Farach, Line Shapes in Electron Spin Resonance, Bulletin of Magnetic Resonance 1, 162 (1979).

[78] L. N. Bulaevskii, Magnetic susceptibility of a chain of spins with antiferromagnetic interaction, Fiz. Tverd. Tela (Leningrad) vol 11, 1132 (1969) [Sov. Phys. Solid State 11, 921 (1969)].

[79] E. Pytte, Peierls instability in Heisenberg chains, Phys. Rev. B 10, 4637 (1974).

[80] J. W. Bray, H. R. Hart, L. V. Interrante, I. S. Jacobs, J. S. Kasper, G. D. Watkins, S. H. Wee and J. C. Bonner, Observation of a Spin-Peierls Transition in a Heisenberg Antiferromagnetic Linear-Chain System, Phys. Rev. Lett 35, 744 (1975).

[81] T. Nakamura, Possible Charge Ordering Patterns of the Paramagnetic Insulating States in $(TMTTF)_2X$, J. Phys. Soc. Jpn 72, 213 (2003).

[82] M. Kozlov, K. Pokhodnia and A. Yurchenko, Electron molecular vibration coupling in vibrational spectra of BEDT-TTF based radical cation salts, Spectrochimica Acta Part A: Molecular Spectroscopy 45, 437 (1989).

[83] O. Drozdova, G. Saito, H. Yamochi, K. Ookubo, K. Yakushi, M. Uruichi and L. Ouahab, Composition and structure of the anion layer in the organic superconductor κ'-$(ET)_2Cu_2(CN)_3$: Optical study, Inorganic Chemistry 40, 3265 (2001).

[84] M. Kozlov, K. Pokhodnia and A. Yurchenko, The assignment of fundamental vibrations of BEDT-TTF and BEDT-TTF-d_8, Spectrochimica Acta Part A: Molecular Spectroscopy 43, 323 (1987).

[85] D. I. Khomskii, Basic aspects of the quantum theory of solids: Order and elementary excitations. Cambridge, UK: Cambridge University Press, 2010.

[86] N. Toyota, M. Lang and J. Müller, Low-dimensional molecular metals, Berlin: Springer-Verlag, 2007.

[87] R. S. Peierls, Quantum Theory of Solids. Oxford: Oxford University Press, 2001

[88] J. S. Miller, Extended linear chain compounds: Volume 3. New York: Plenum Press, 1983.

[89] T. Ishiguro and K. Yamaji, Organic superconductors. Berlin: Springer Verlag, 1989.